

Geochronological data processing with **R** and **IsoplotR**

Pieter Vermeesch
Department of Earth Sciences
University College London
`p.vermeesch@ucl.ac.uk`

Contents

I	Basic geochronology	5
1	Introduction	6
2	Basic Notions	8
2.1	Isotopes and radioactivity	8
2.2	Radioactivity	8
2.3	The age equation	10
2.4	Decay series	11
3	Analytical techniques	14
3.1	Mass spectrometry	14
3.2	Isotope dilution	17
3.3	Sample-standard bracketing	18
4	Simple parent-daughter pairs	19
4.1	^{14}C dating	19
4.2	The Rb-Sr method	20
4.3	Isochrons	21
4.4	The Sm-Nd method	21
5	The U-Pb system	23
5.1	The U-(Th-)Pb method	23
5.2	The Pb-Pb method	24
5.3	Concordia	25
5.4	Detrital geochronology	25
6	The K-Ar system	27
6.1	K-Ar dating	27
6.2	$^{40}\text{Ar}/^{39}\text{Ar}$ dating	27
6.3	Applications	28
7	Thermochronology	30
7.1	The U-Th-He method	30
7.2	Fission tracks	31
8	U-series dating	35
8.1	The ^{234}U - ^{238}U method	35
8.2	The ^{230}Th method	36
8.3	The ^{230}Th -U method	36

9 Error propagation	38
9.1 Some basic definitions	38
9.2 Examples	39
9.3 Accuracy vs. precision	40
10 Exercises	42
11 Programming practicals	44
11.1 Introduction to R	44
11.2 U-Th-Pb data reduction	48
11.3 $^{40}\text{Ar}/^{39}\text{Ar}$ data reduction	48
11.4 Error propagation	49
11.5 Fission tracks	50
II Advanced geochronology	51
12 Introduction	52
13 Statistical considerations	54
13.1 The normal distribution	54
13.2 The method of maximum likelihood	55
13.3 The mean square of weighted deviates (MSWD)	57
13.4 Dealing with overdispersion	60
13.5 Error correlations	61
13.6 Linear regression	63
13.7 Confidence intervals	65
14 Generic functions	69
14.1 Weighted mean and outlier detection	69
14.2 Frequency distributions	70
14.3 Radial plots	71
14.4 Mixture models	73
15 U–Pb geochronology	78
15.1 Input formats	78
15.2 Concordia diagrams and ages	80
15.3 Discordia/isochron regression	83
15.4 Common Pb	85
15.5 Initial disequilibrium	88
15.6 Discordance filters	90
16 Pb–Pb and Th–Pb	94
16.1 Pb–Pb	94
16.2 (inverse) isochrons	94
16.3 The Stacey-Kramers growth curve	95
16.4 Th–Pb	96
16.5 Single grain ages	97

17 Ar–Ar and K–Ca	98
17.1 Ar–Ar	98
17.2 Age spectra	99
17.3 K–Ca	100
18 Rb–Sr, Sm–Nd, Lu–Hf and Re–Os	101
19 U–Th–(Sm)–He	103
19.1 The α -ejection correction	103
19.2 isochrons	105
19.3 Compositional data analysis and the ‘helioplot’	105
20 Fission tracks	109
20.1 The external detector method	109
20.2 LA-ICP-MS based fission track dating	110
20.3 Compositional zoning	111
20.4 Zero track counts	112
21 ^{230}Th–U dating	114
21.1 Data formats	115
21.2 Isochrons	115
21.3 Th–U evolution diagrams	116
22 Detrital geochronology	118
22.1 Maximum depositional age estimation	118
22.2 Multi-sample plots	119
22.3 Multidimensional scaling	121
III IsoplotR manual	125
23 Introduction to IsoplotR	126
23.1 Software architecture	126
23.2 The Graphical User Interface (GUI)	127
23.3 The Command Line Interface (CLI)	129

Part I

Basic geochronology

Chapter 1

Introduction

The use of naturally occurring radioactive isotopes to date minerals and rocks is the oldest branch of isotope geology. The foundations of these so-called isotopic or radiometric dating methods were laid shortly after the turn of the XXth century with the discovery of the laws of radioactive decay by eminent physicists such as Ernest Rutherford and Frederick Soddy (Rutherford and Soddy, 1902a; Rutherford and Soddy, 1902b). The application of these principles to the field of Geology and the calibration of the geological time scale were pioneered by Arthur Holmes (1911), Holmes (1913), and Holmes (1947). Initially, radiometric geochronology was exclusively based on uranium and its daughter products, but with the development of increasingly sensitive analytical equipment, ever more isotopic ‘clocks’ were added over the course of the century: Rb/Sr (Hahn et al., 1943), ¹⁴C (Libby, 1946), K/Ar (Aldrich and Nier, 1948), ²³⁸U fission tracks (Price and Walker, 1963), ⁴⁰Ar/³⁹Ar (Merrihue and Turner, 1966), Sm/Nd (Lugmair, 1974), etc.

The first part of these lecture notes provides a basic introduction to all these methods. Chapter 2 reviews the basic principles of radioactive decay, which form the basis of all isotopic dating techniques. It will derive the fundamental age equation and introduce the concepts of secular equilibrium, which will be revisited in later chapters. Chapter 3 provides the briefest of introductions to the world of mass spectrometry. It will sketch the basic operating principles of the instruments used to acquire the datasets that will be used for R programming exercises later on. Chapters 4–8 provide basic introductions to the radiocarbon, Rb–Sr, Sm–Nd, U–Pb, Ar–Ar, U–Th–He, fission track and Th–U methods, which will be fleshed out further in Part 2 of the notes.

Chapter 9 presents a primer in error propagation which is extremely important because, to quote K.R. Ludwig “The uncertainty of the age is as important as the age itself” (Ludwig, 2003). Chapter 10 contains a collection of exercises that are meant to be solved by pencil on paper, whereas Chapter 11 contains a collection of practical exercises that require the R programming language. In these exercises, you will process some raw data files for the U–Pb, Ar–Ar and fission track methods. The purpose of these exercises is to provide a glimpse into the ‘black box’ data processing software that is normally used by geochronologists to turn mass spectrometer data into tables of isotopic ratios for further processing with the *IsoplotR* package that is the subject of Part 2 of this book.

The core of these notes is formed by Prof. Peter van den Haute’s lecture notes (in Dutch) at the University of Ghent. This was expanded with additional material, exercises, and practicals. Some figures were modified from published sources, including Allègre (2008), Braun, Van Der Beek, and Batt (2006), and Galbraith (2005). These books are recommended further reading

material, as is the detailed textbook by Dickin (2005), from which both Allègre (2008) and van den Haute heavily borrowed. Additional lecture material, including the data files used in the programming practicals of Chapter 11, can be found at <https://github.com/pvermees/geotopes/>.

References

- Aldrich, L. T. and A. O. Nier (1948). “Argon 40 in potassium minerals”. In: *Physical Review* 74.8, p. 876.
- Allègre, C. J. (2008). *Isotope geology*. Cambridge University Press, p. 512.
- Braun, J., P. Van Der Beek, and G. Batt (2006). *Quantitative thermochronology: numerical methods for the interpretation of thermochronological data*. Cambridge University Press.
- Dickin, A. P. (2005). *Radiogenic isotope geology*. Cambridge University Press, p. 492.
- Galbraith, R. F. (2005). *Statistics for fission track analysis*. CRC Press, p. 219.
- Hahn, O. et al. (1943). “Geologische Altersbestimmungen mit der strontiummethode”. In: *Chem. Zeitung* 67, pp. 55–6.
- Holmes, A. (1911). “The association of lead with uranium in rock-minerals, and its application to the measurement of geological time”. In: *Proceedings of the Royal Society of London. Series A, Containing Papers of a Mathematical and Physical Character* 85.578, pp. 248–256.
- (1913). *The age of the Earth*. Harper & Brothers.
- (1947). “The Construction of a Geological Time-Scale”. In: *Transactions of the Geological Society of Glasgow* 21.1, pp. 117–152.
- Libby, W. F. (1946). “Atmospheric helium three and radiocarbon from cosmic radiation”. In: *Physical Review* 69.11-12, p. 671.
- Ludwig, K. R. (2003). “Mathematical-statistical treatment of data and errors for $^{230}\text{Th}/\text{U}$ geochronology”. In: *Reviews in Mineralogy and Geochemistry* 52.1, pp. 631–656.
- Lugmair, G. (1974). “Sm-Nd ages: a new dating method”. In: *Meteoritics* 9, p. 369.
- Merrihue, C. and G. Turner (1966). “Potassium-argon dating by activation with fast neutrons”. In: *Journal of Geophysical Research* 71.11, pp. 2852–2857.
- Price, P. and R. Walker (1963). “Fossil tracks of charged particles in mica and the age of minerals”. In: *Journal of Geophysical Research* 68.16, pp. 4847–4862.
- Rutherford, E. and F. Soddy (1902a). “The cause and nature of radioactivity – Part I”. In: *The London, Edinburgh, and Dublin Philosophical Magazine and Journal of Science* 4.21, pp. 370–396.
- (1902b). “The cause and nature of radioactivity – Part II”. In: *The London, Edinburgh, and Dublin Philosophical Magazine and Journal of Science* 4.23, pp. 569–585.

Chapter 2

Basic notions of radiometric geochronology

2.1 Isotopes and radioactivity

Thanks to discoveries by Niels Bohr, Ernest Rutherford, Arnold Sommerfeld, Joseph Thomson and James Chadwick, we know that rocks and minerals are made of atoms, atoms are made of a nucleus and an electron cloud, and the nucleus is made of *nucleons* of which there are two kinds: protons and neutrons. The total number of nucleons in the atomic nucleus is called the *mass number* (A). The number of protons (which equals the number of electrons in a neutral atom) is called the *atomic number* (Z). The chemical properties of a nuclide solely depend on the atomic number, which therefore forms the basis of the Periodic Table of Elements. The number of neutrons in the atomic nucleus may take on a range of values for any given element, corresponding to different *isotopes* of said element. For example, $^{16}_8\text{O}$ is an isotope of oxygen with 16 nucleons of which 8 are protons (and $N = A - Z = 16 - 8 = 8$ are neutrons). Adding one extra neutron to the nucleus produces a second oxygen isotope, $^{17}_8\text{O}$, with identical chemical properties as $^{16}_8\text{O}$, but slightly different physical properties (e.g. boiling temperature). Adding another neutron produces $^{18}_8\text{O}$ which, with 8 protons and 10 neutrons, is more than 10% heavier than $^{16}_8\text{O}$. Due to this mass difference, the $^{18}_8\text{O}/^{16}_8\text{O}$ ratio undergoes *mass fractionation* by several natural processes, forming the basis of $^{18}_8\text{O}/^{16}_8\text{O}$ palaeothermometry (see the second half of this course). When we try to add yet another neutron to the atomic nucleus of oxygen, the nucleus becomes unstable and undergoes radioactive decay. Therefore, no $^{19}_8\text{O}$ exists in nature.

2.2 Radioactivity

As mentioned before, the Periodic Table of Elements (aka ‘Mendeleev’s Table’) arranges the elements according to the atomic number and the configuration of the electron cloud. The equally important *Chart of Nuclides* uses both the number of protons and neutrons as row and column indices. At low masses, the stable nuclides are found close to the $1 \div 1$ line ($N \approx Z$), with the radionuclides found at higher and lower ratios. At higher atomic numbers, the stable nuclides are found at higher mass numbers, reflecting the fact that more neutrons are required to keep the protons together. For example, $^{208}_{82}\text{Pb}$, which is the heaviest stable nuclide, has 44 more neutrons than protons. The unstable nuclides (or *radionuclides*), such as $^{209}_{82}\text{Pb}$ or $^{19}_8\text{O}$ may survive for time periods of femtoseconds to billions of years depending on the degree of instability, which generally scales with the ‘distance’ from the curve of stable nuclides. Radionuclides eventually disintegrate to a stable form by means of a number of different mechanisms:

1. α -decay

The atomic nucleus (e.g., $^{238}_{92}\text{U}$, $^{235}_{92}\text{U}$, $^{232}_{90}\text{Th}$, $^{147}_{62}\text{Sm}$) loses an α particle, i.e. the equivalent of a ^4_2He nucleus. When these nuclei acquire electrons, they turn into Helium atoms, forming the basis of the U-Th-He chronometer, which is further discussed in Section 7.1. The recoil energy of the decay is divided between the α particle and the parent nucleus, which eventually relaxes into its ground state by emitting γ -radiation, i.e. photons with a wavelength of 10^{-12}m or less. In addition to the aforementioned U-Th-He method, α -decay is central to the ^{147}Sm - ^{143}Nd (Section 4.2), ^{235}U - ^{207}Pb , ^{238}U - ^{206}Pb and ^{232}Th - ^{208}Pb methods (Section 5).

2. β -decay

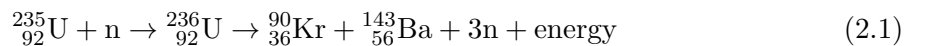
Comprises negatron (β^-) and positron (β^+) emission, in which either an electron or a positron is emitted from the nucleus, causing a transition of $(N,Z) \rightarrow (N-1,Z+1)$ for β^- decay and $(N,Z) \rightarrow (N+1,Z-1)$ for β^+ decay. For example, the oxygen isotope $^{19}_8\text{O}$ discussed in Section 2.1 decays to $^{19}_9\text{F}$ by β^- emission. In contrast with α particles, which are characterized by discrete energy levels, β particles are characterised by a continuous energy spectrum. The difference between the maximum kinetic energy and the actual kinetic energy of any given emitted electron or positron is carried by a neutrino (for β^+ decay) or an anti-neutrino (for β^- decay). Just like α decay, β decay is also accompanied by γ -radiation, arising from two sources: (a) relaxation into the ground state of the excited parent nucleus and (b) spontaneous annihilation of the unstable positron in β^+ decay. β^- decay is important for the ^{40}K - ^{40}Ca , ^{87}Rb - ^{87}Sr (Section 4.2) and ^{14}C - ^{14}N (Section 4.1) clocks. It also occurs as part of the ^{235}U - ^{207}Pb , ^{238}U - ^{206}Pb and ^{232}Th - ^{208}Pb decay series (Sections 5 and 8). β^+ decay is found in the ^{40}K - ^{40}Ar system (Section 6).

3. electron capture

This is a special form of decay in which an ‘extra-nuclear’ electron (generally from the K-shell) is captured by the nucleus. This causes a transformation of $(N,Z) \rightarrow (N+1,Z-1)$, similar to positron emission, with which it often co-exists. The vacant electron position in the K-shell is filled with an electron from a higher shell, releasing X-rays ($\sim 10^{-10}\text{m}$ wavelength), which is the diagnostic signal of electron capture. This mechanism occurs in the ^{40}K - ^{40}Ar decay scheme (Section 6).

4. nuclear fission

Extremely large nuclei may disintegrate into two daughter nuclei of unequal size, releasing large amounts of energy ($\sim 200\text{ MeV}$). The two daughter nuclei move in opposite directions from the parent location, damaging the crystal lattice of the host mineral in their wake. The two daughter nuclides are generally radioactive themselves, giving rise to β -radiation before coming to rest as stable isotopes. $^{238}_{92}\text{U}$ is the only naturally occurring nuclide that undergoes this type of radioactive decay in measurable quantities, and even then it only occurs once for every $\sim 2 \times 10^6$ α -decay events. Nevertheless, the fission mechanism forms the basis of an important geochronological method, in which the damage zones or ‘fission tracks’ are counted (Section 7.2). Nuclear fission can also be artificially induced, by neutron irradiation of ^{235}U , e.g.:



Note that every neutron on the left hand side of this formula generates three neutrons on the right hand side. The latter may react with further ^{235}U nuclei and generate a chain reaction. This forms the basis of nuclear reactors, the atom bomb and the ‘external detector’ method (Section 7.2).

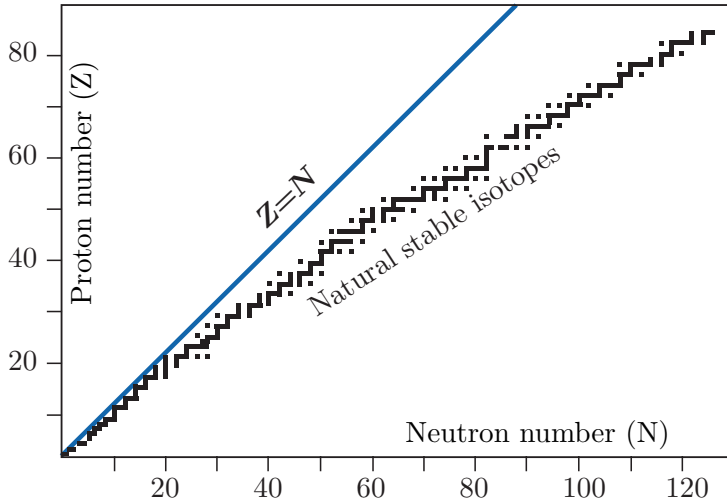


Figure 2.1: A schematic ‘*Chart of Nuclides*’ (modified from Allègre, 2008).

2.3 The age equation

A characteristic property of radioactive decay is its absolute independence of external physical and chemical effects. In other words, it is not affected by changes in pressure, temperature, or the molecular bonds connecting a radioactive nuclide to neighbouring atoms. This means that the rate at which a radioactive parent decays to a radiogenic daughter per unit time, i.e. dP/dt only depends on P , the number of parent atoms present. The *decay constant* λ expresses the likelihood that a radioactive disintegration takes place in any given time (i.e., λ has units of atoms per atoms per year). This can be expressed mathematically with the following differential equation:

$$\frac{dP}{dt} = -\lambda P \quad (2.2)$$

Integrating this equation over time yields:

$$P = P_0 e^{-\lambda t} \quad (2.3)$$

where P_0 is the number of parent atoms present at time $t = 0$. Since this number is generally unknown (one exception is ^{14}C , see Section 4.1), Equation 2.3 generally cannot be used in this form. We can, however, measure the *present* number of parent and daughter nuclides in the sample. Rewriting Equation 2.3:

$$P_0 = P e^{\lambda t} \quad (2.4)$$

and bearing in mind that $P_0 = P + D$, we obtain:

$$D = P(e^{\lambda t} - 1) \quad (2.5)$$

This equation forms the foundation of most geochronological methods. It can be rewritten explicitly as a function of time:

$$t = \frac{1}{\lambda} \ln \left(\frac{D}{P} + 1 \right) \quad (2.6)$$

The degree of instability of a radioactive nuclide can be expressed by λ or by the *half life* $t_{1/2}$, which is the time required for half of the parent nuclides to decay. This follows directly

from Equation 2.3:

$$\frac{P_o}{2} = P_o e^{-\lambda t_{1/2}} \Rightarrow t_{1/2} = \frac{\ln(2)}{\lambda} \quad (2.7)$$

As a rule of thumb, the detection limit of a radiometric geochronometer is reached after about 10 half lives. Thus, ^{14}C goes back $\sim 50,000$ years, ^{10}Be 10 million and ^{40}K 10 billion years.

2.4 Decay series

Sometimes the radiogenic daughter (D_1) of a radioactive parent is radioactive as well, decaying to a daughter of its own (D_2), which may be radioactive again etc., until a stable daughter (D_*) is reached. Considering the simplest case of one intermediate daughter:



The increase (or decrease) of the number of atoms per unit time for each of the nuclides is given by:

$$\text{for } P : dP/dt = -\lambda_P P \quad (2.9)$$

$$\text{for } D_1 : dD_1/dt = \lambda_P P - \lambda_1 D_1 \quad (2.10)$$

$$\text{for } D_* : dD_*/dt = \lambda_1 D_1 \quad (2.11)$$

The number of parent atoms P can be written as a function of t :

$$P = P_o e^{-\lambda_P t} \quad (2.12)$$

Plugging Equation 2.12 into 2.10 yields

$$dD_1/dt = \lambda_P P_o e^{-\lambda_P t} - \lambda_1 D_1 \quad (2.13)$$

Solving this differential equation yields the evolution of D_1 with time. Assuming that $D_1 = 0$ at $t = 0$:

$$D_1 = \frac{\lambda_P}{\lambda_1 - \lambda_P} P_o \left[e^{-\lambda_P t} - e^{-\lambda_1 t} \right] \quad (2.14)$$

If $\lambda_P \ll \lambda_1$ (by a factor of 10 or greater), and $t \gg 1/\lambda_1$ then $e^{-\lambda_1 t}$ becomes vanishingly small relative to $e^{-\lambda_P t}$ so that Equation 2.14 can be simplified:

$$D_1 = \frac{\lambda_P}{\lambda_1 - \lambda_P} P_o e^{-\lambda_P t} \quad (2.15)$$

or, alternatively:

$$D_1 = \frac{\lambda_P}{\lambda_1 - \lambda_P} P \quad (2.16)$$

This means that the ratio of D_1 and P remains constant through time. If $\lambda_P \ll \lambda_1$, then $\lambda_1 - \lambda_P \approx \lambda_1$, from which it follows that:

$$D_1 = \frac{\lambda_P}{\lambda_1} P \quad (2.17)$$

Rearranging:

$$D_1\lambda_1 = P\lambda_P \quad (2.18)$$

or, equivalently:

$$\frac{P}{D_1} = \frac{t_{1/2}(P)}{t_{1/2}(D_1)} \quad (2.19)$$

This is the *secular equilibrium* in which the number of atoms of both radioactive members is proportional to their respective half lives. In the geochronological isotope systems $^{235}\text{U}/^{207}\text{Pb}$, $^{238}\text{U}/^{206}\text{Pb}$ and $^{232}\text{Th}/^{208}\text{Pb}$, the lead isotopes are the end points of a long decay series comprised of several α and β^- disintegrations, in which the decay constants of the parent nuclide is orders of magnitude shorter than the other nuclides in the chain. For a decay series like that, Equation 2.18 can be generalised to:

$$D_n\lambda_n = \dots = D_2\lambda_2 = D_1\lambda_1 = P\lambda_P \quad (2.20)$$

This means that the entire series is in equilibrium, so that all members occur in mutually constant proportions. The number of atoms of the stable end member D_* is given by:

$$D_* = P_o - P - D_1 - D_2 - \dots - D_n \quad (2.21)$$

Using Equation 2.20, this becomes:

$$D_* = P_o - P - \frac{P\lambda_P}{\lambda_1} - \frac{P\lambda_P}{\lambda_2} - \dots - \frac{P\lambda_P}{\lambda_n} \quad (2.22)$$

or

$$D_* = P_o - P \left(1 + \frac{\lambda_P}{\lambda_1} + \frac{\lambda_P}{\lambda_2} + \dots + \frac{\lambda_P}{\lambda_n} \right) \quad (2.23)$$

Since each of the ratios λ_P/λ_1 , λ_P/λ_2 , etc. are vanishingly small, we can simplify Equation 2.23 as:

$$D_* = P_o - P = P \left(e^{\lambda_P t} - 1 \right) \quad (2.24)$$

This means that the accumulation of the final Pb isotope of the aforementioned three decay series is only a function of the decay of the parent isotope. All intermediate decay steps are therefore inconsequential. In rare cases, however, the isotopic equilibrium is disturbed by a dissolution or recrystallisation event, say. The intermediate parent/daughter pairs can then be used to date phenomena occurring over much shorter time scales than those probed by the U-Pb method (Section 8).

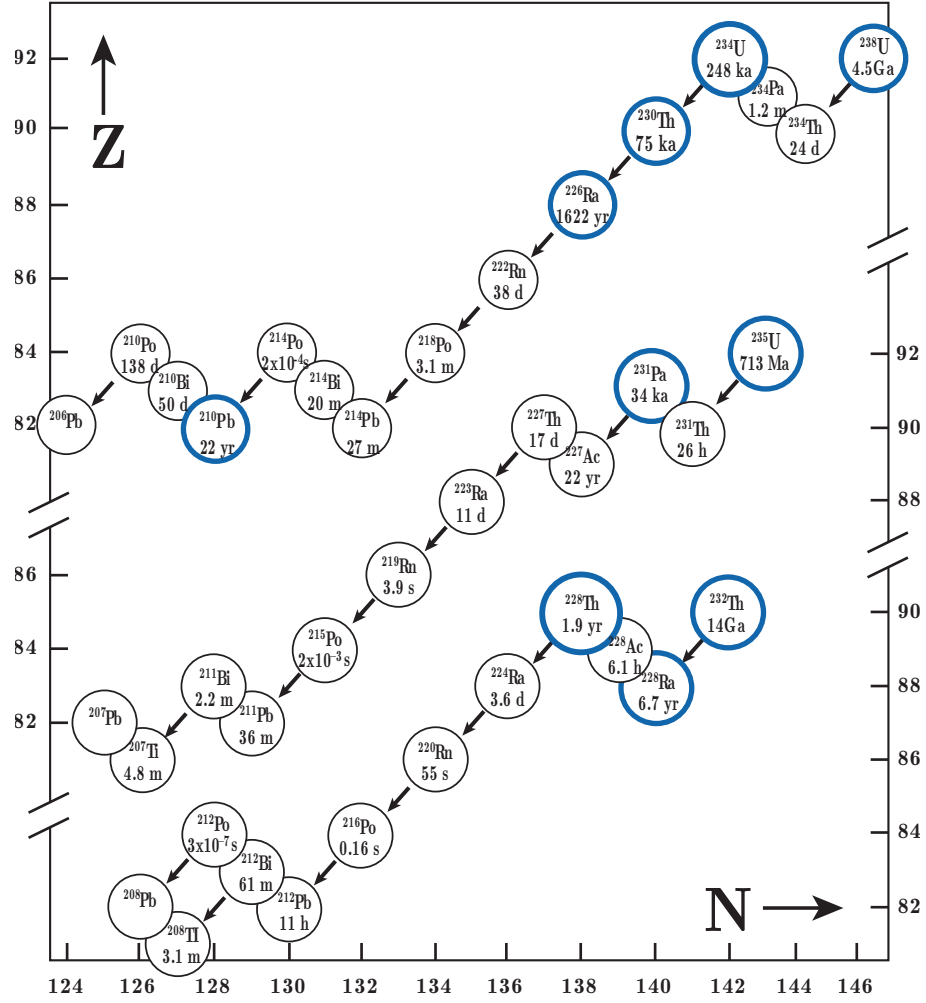


Figure 2.2: The decay series of ^{232}Th , ^{235}U and ^{238}U , which form the basis of the U-Th-Pb, U-Th-He and U-Th-series methods (modified from Allègre, 2008).

Chapter 3

Analytical techniques

Isotope geochemistry is based on the accurate and precise determination of elemental and isotopic compositions of rocks and minerals. Although some of the earliest geochronological methods (notably the ^{14}C method, see Section 4.1) were based on the detection of radioactivity by means of Geiger-Müller counters and liquid scintillation detectors, nearly all modern isotope geochemistry is done by mass spectrometry.

3.1 Mass spectrometry

A mass spectrometer is a device that separates electrically charged atoms or molecules based on their mass, enabling precise measurement of the isotopic composition. A mass spectrometer consists of the following parts:

1. ion source: this can be either a filament (similar to that found in an incandescent light bulb), a plasma torch, a primary ion beam, or a spray chamber, among other possibilities.
2. mass analyser: this can be an electromagnet (possibly combined with an electrostatic field), or a rapidly fluctuating electric field.
3. ion detector: this is, essentially, a volt meter.

In the remainder of this section, we will assume the source to be a filament and the mass analyser to be an electromagnet.

After pumping the mass spectrometer down to (ultra-)high vacuum conditions (10^{-6} to 10^{-9} mbar), the sample enters the ion source as a gas, where it is bombarded with electrons. The resulting ions (with charge e) are accelerated in an electric field (with potential difference V) and collimated to a narrow beam. This beam is sent through a magnetic field (with strength H) which deflects it into a circular trajectory with a radius proportional to the ion mass (m). This results in a physical separation of the incoming ion beam into various outgoing beams. The beams of interest are steered into the ion detector which, in its simplest design (the so-called ‘Faraday Cup’) consists of a long and narrow cup. The ion beam is neutralised in the cup by electrons flowing from ground through a resistor. The potential difference across this resistor is measured and registered on a computer for further processing.

The electric field transfers a certain amount of kinetic energy to the ions:

$$E = eV = \frac{mv^2}{2} \quad (3.1)$$

With e is the electrical charge (in multiples of $1.60219 \times 10^{-19}\text{C}$, which is the elementary charge of an electron. Because each type of ion has a different mass (m , in multiples of $1.660538 \times 10^{-27}\text{kg}$, the atomic mass unit), their terminal velocity (v) differs as well:

$$v = \sqrt{\frac{2eV}{m}} \quad (3.2)$$

The mass analyser deflects the ions according to the following equation:

$$Hev = \frac{mv^2}{r} \quad (3.3)$$

Substituting Equation 3.2 into 3.3 yields:

$$H\sqrt{\frac{2eV}{m}} = \frac{2V}{r} \quad (3.4)$$

from which it follows that:

$$r = \frac{1}{H} \sqrt{\frac{2mV}{e}} \quad (3.5)$$

and $H = \frac{1}{r} \sqrt{\frac{2mV}{e}}$

Equation 3.5 allows us to calculate the radius of the ion trajectory for any given mass-to-charge ratio m/e . Note that light isotopes are more strongly deflected than equally charged heavy ones. Equation 3.5 can also be used to calculate the magnetic field strength required to deflect an ion beam with a given m/e ratio into the collector. This is more practical because most mass spectrometers have a fixed radius so that the different ions must be collected by varying H . Some modern mass spectrometers are equipped with multiple ion collectors the enabling simultaneous analysis of several ionic masses.

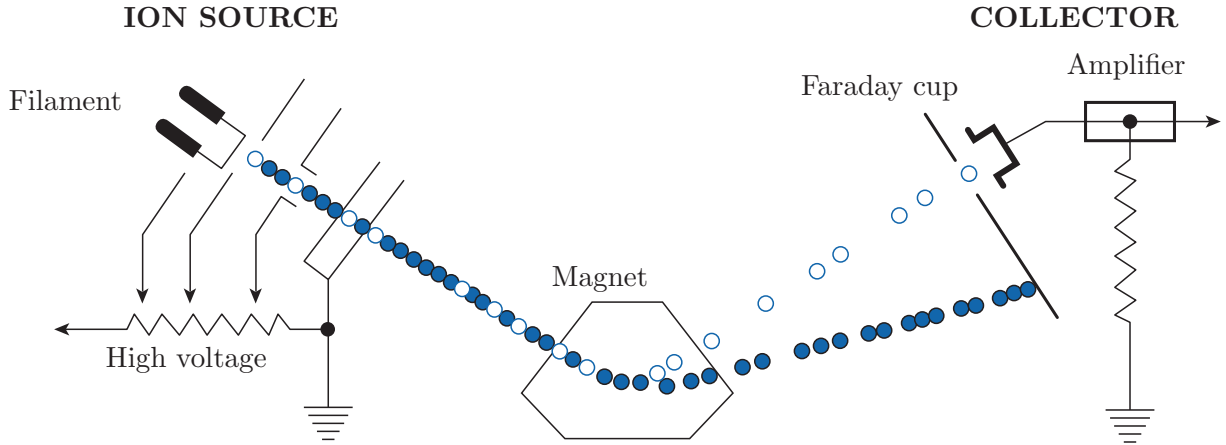


Figure 3.1: Schematic diagram of a sector-field noble gas or TIMS mass spectrometer (modified from Allègre, 2008).

Several types of mass spectrometers are used for geoscience applications:

1. *Thermal Ionisation Mass Spectrometry (TIMS).*

The sample is dissolved and subjected to careful chemical separation procedures (liquid chromatography) in order to separate the parent and daughter elements to a high level of purity. The resulting solutions are spiked and deposited on a tungsten or tantalum filament, which is brought to a glow by an electric current and thus produces ions. These are separated by a

large electromagnet and analysed in one or more Faraday cups. TIMS is very time consuming but produces extremely precise results (%-level precision on the ages).

2. *Inductively Coupled Plasma Mass Spectrometry (ICP-MS).*

The sample is vapourised in one of two ways: either by introducing a liquid into a spray chamber, or by firing an ultraviolet laser at a solid sample and transporting the resulting aerosol into the ion source with a carrier gas (typically helium). The ion source itself consists of an argon flow which is heated to a temperature of approximately 10,000K by sending a radiofrequency current through a coil. This breaks up all the molecular bonds and produces a plasma (i.e. a ‘soup’ of ions and electrons) which enters the high vacuum chamber through a tiny opening. The mass analyser can either be a sector magnet or a quadrupole (which consists of four metal rods generating a rapidly fluctuating electrical field). ICP-MS offers a higher throughput than TIMS, especially in laser ablation mode, where hundreds of ages can be measured per day. However, this increased throughput comes at the expense of precision, which is on the percent level (better in solution mode).

3. *Secondary ion mass spectrometry (SIMS)*

Prior to the development of laser ablation (LA-) ICP-MS, the only other method to produce spot measurements in solid samples was by firing a beam of negative (e.g. oxygen) or positive (e.g. caesium) ions at the target under high vacuum. This releases (‘sputters’) positive (or negative, in the case of a Cs beam) *secondary* ions from the sample surface, which are accelerated by an electrostatic field and sent to a sector field mass spectrometer. Although SIMS has been replaced by LA-ICP-MS in some applications, it remains an important instrument in the geochronological toolbox because (a) it offers higher spatial resolution than laser ablation (5-10 μ m vs. 25-50 μ m) and (b) can measure light ions (e.g, hydrogen) more reliably than LA-ICP-MS.

4. *Noble gas mass spectrometry*

The noble gases (He, Ne, Ar, Kr, Xe) require a different class of mass spectrometer than the rest of the periodic table because, as their name suggests: 1) they are gases 2) that do not ionise easily. Noble gases are liberated from solid state materials by heating or laser ablation under ultra-high vacuum conditions. To remove any unwanted gas species (such as CO, CO₂, hydrocarbons, etc.) that may interfere with the noble gas measurements, the released gas is exposed to reactive metals, liquid N₂ ‘cold traps’ and other ‘gettering’ devices in a ‘noble gas extraction line’ for a duration of 5–30 minutes. The extraction line removes all the reactive gas species until only the inert noble gases remain. It is only after this lengthy delay that the purified noble gases are ionised by electron bombardment, and analysed on the actual mass spectrometer.

5. *Accelerator Mass Spectrometer (AMS)*

The AMS combines two mass spectrometers with a (‘tandem’ type) particle accelerator. Ions are produced by a SIMS source and steered through a first mass analyser, which selects all ions of a desired mass (e.g., mass 14: ¹⁴C[−], ¹²CH₂[−], ...). The resulting beam is accelerated in the first part of the tandem accelerator by a potential difference of several million eV, and sent through a thin chamber filled with a ‘stripper’ gas. Collisions of stripper gas atoms with the incoming ions destroys any molecular bonds and forms 3+ ions in the process. The beam now consists of purely atomic ions, which are accelerated in the second part of the accelerator and steered into a second mass analyser. The AMS has revolutionised the ¹⁴C method by enabling the analysis of extremely small (mg-sized) samples (see Section 4.1), and has enabled a whole new field of geochronology based on the analysis of terrestrial cosmogenic radionuclides. The

main limitation of AMS is its high cost. Currently only two AMS facilities are operating in the UK (in Oxford and Glasgow).

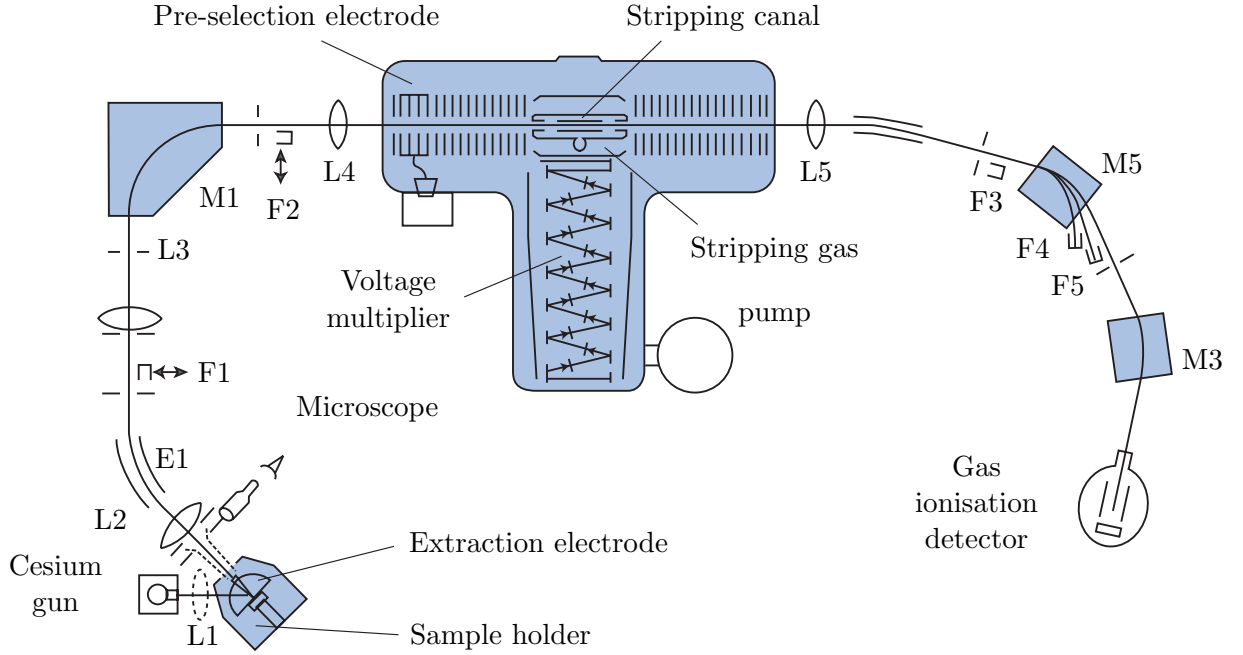


Figure 3.2: Schematic diagram of an Accelerator Mass Spectrometer (AMS) (modified from Allègre, 2008).

3.2 Isotope dilution

Besides determining isotopic compositions, the mass spectrometer can also be used to measure elemental concentrations, using a method called *isotope dilution*. This is done by mixing the sample solution (whose isotopic composition has already been determined) with a known quantity of a solution with a different (but known) isotopic composition and known elemental concentration. The latter solution is called the *spike*. The isotopic composition of the mixture is analysed by mass spectrometry. The measured isotopic ratio R_m for an element with two isotopes (aX and bX) is given by:

$$R_m = \frac{N^a X_N + S^a X_S}{N^b X_N + S^b X_S} \quad (3.6)$$

with

$$\begin{aligned} N &= \text{the number of atoms of X in the sample} \\ S &= \text{the number of atoms of X in the spike} \\ {}^aX_N, {}^bX_N &= \text{the atomic abundance of isotope } a \text{ (or } b \text{) in the} \\ {}^aX_S, {}^bX_S &= \text{sample (or spike) } ({}^aX_N + {}^bX_N = {}^aX_S + {}^bX_S = 1) \end{aligned}$$

N is the only unknown in Equation 3.6, which can therefore be rewritten as:

$$N = S \frac{{}^aX_S - R_m {}^bX_S}{R_m {}^bX_N - {}^aX_N} \quad (3.7)$$

N can also be expressed as a function of the isotopic ratios in the sample $R_N (= {}^aX_N/{}^bX_N)$ and in the spike $R_S (= {}^aX_S/{}^bX_S)$. The atomic abundance of aX and bX in the sample are given by:

$${}^aX_N = \frac{R_N}{R_N + 1} \text{ and } {}^bX_N = \frac{1}{R_N + 1} \quad (3.8)$$

and in the spike:

$${}^aX_S = \frac{R_S}{R_S + 1} \text{ and } {}^bX_S = \frac{1}{R_S + 1} \quad (3.9)$$

Substituting Equations 3.9 and 3.8 into 3.7 yields:

$$N = S \frac{(R_N + 1)(R_S - R_m)}{(R_S + 1)(R_m - R_N)} \quad (3.10)$$

Equations 3.7 and 3.10 give the atomic concentration of X (in atoms/g). Dividing N by Avogadro's number N_A and multiplying with the atomic weights (g/mol) yields the corresponding weight percentages. Isotope dilution is a very powerful method because:

1. It does not require quantitative separation of the elements of interest.
2. Chemical purification removes unwanted interferences from other species.
3. The method is very sensitive, so extremely low concentrations can be measured (ppb or less).

3.3 Sample-standard bracketing

Isotope dilution is the 'gold standard' for isotope geochemistry, recommended when the most accurate and precise results are desired. Unfortunately, isotope dilution is also very time consuming and cannot be readily applied to micro-analytical techniques such as LA-ICP-MS and SIMS. In those cases, an alternative method is used, which is less precise (%- rather than ‰-level precision) but quicker. The idea is to normalise the signal ratios recorded by the mass spectrometer to a standard of known age. As before, let P be a radioactive parent which decays to a radiogenic daughter D . Suppose that we can measure both nuclides on the same mass spectrometer, yielding two electronic signal intensities S_P and S_D . These signals may be recorded in units of V, A, or Hz. We cannot directly use the signal ratios as a proxy for the isotopic ratio:

$$\frac{D}{P} \neq \frac{S_D}{S_P}$$

because the parent and daughter are two different elements with different chemical properties and ionisation efficiencies. We can, however, assume that the isotopic ratio is proportional to the signal ratio:

$$\frac{D}{P} = C \frac{S_D}{S_P} \quad (3.11)$$

Thus, if we double D (and thus D/P), we would also expect to double S_D (and thus S_D/S_P). To determine the constant of proportionality C , we analyse a standard of known age (t_s) and, hence (D/P)-ratio (due to Equation 2.5):

$$C = \left(e^{\lambda_P t_s} - 1 \right) \frac{S_P^s}{S_D^s} \quad (3.12)$$

where λ_P is the decay constant of the parent and S_P^s/S_D^s is the (inverse) signal ratio of the standard.

Chapter 4

Simple parent-daughter pairs

4.1 ^{14}C dating

There are two stable isotopes of carbon: ^{12}C and ^{13}C , and one naturally occurring radionuclide: ^{14}C . The half life of ^{14}C is only 5,730 years, which is orders of magnitude shorter than the age of the Earth. Therefore, no primordial radiocarbon remains and all ^{14}C is *cosmogenic*. The main production mechanism is through secondary cosmic ray neutron reactions with ^{14}N in the stratosphere: $^{14}_7\text{N} (\text{n,p}) ^{14}_6\text{C}$. Any newly formed ^{14}C rapidly mixes with the rest of the atmosphere creating a spatially uniform carbon composition, which is incorporated into plants and the animals that eat them. Prior to the industrial revolution, a gram of fresh organic carbon underwent 13.56 (β^-) decays per minute. When a plant dies, it ceases to exchange carbon with the atmosphere and the ^{14}C concentration decays with time according to Equation 2.2:

$$\frac{d^{14}C}{dt} = -\lambda_{14} \times ^{14}C \quad (4.1)$$

where $\lambda_{14} = 0.120968 \text{ ka}^{-1}$. Thus, the radiocarbon concentration is directly proportional to the radioactivity, which can be measured by β -counting. This can then be used to calculate the radiocarbon age by rearranging Equation 2.3:

$$t = -\frac{1}{\lambda_{14}} \ln \left[\frac{d^{14}C/dt}{(d^{14}C/dt)_o} \right] \quad (4.2)$$

where $(d^{14}C/dt)_o$ is the original level of β activity. This method was developed by Willard Libby in 1949, for which he was awarded the Nobel Prize in 1960. As mentioned before, $(d^{14}C/dt)_o$ was 13.56 prior to the industrial revolution, when thousands of tonnes of ‘old’ carbon were injected into the atmosphere, resulting in a gradual lowering of the radiocarbon concentration until 1950, when nuclear testing produced an opposite effect, leading to a doubling of the atmospheric ^{14}C activity in 1963. Since the banning of atmospheric nuclear testing, radiocarbon concentrations have steadily dropped until today, where they have almost fallen back to their pre-industrial levels. But even prior to these anthropogenic effects, ^{14}C concentrations underwent relatively large fluctuations as a result of secular variations of the Earth’s magnetic field and, to a lesser extent, Solar activity. These variations in $(d^{14}C/dt)_o$ can be corrected by comparison with a precisely calibrated production rate curve, which was constructed by measuring the ^{14}C activity of tree rings (*dendrochronology*).

Since the 1980’s, β -counting has been largely replaced by accelerator mass spectrometry (AMS, see Section 3.1), in which the ^{14}C concentration is measured directly relative to a stable isotope such as ^{13}C . Although this has not significantly pushed back the age range of the

radiocarbon method, it has nevertheless revolutionised the technique by reducing the sample size requirements by orders of magnitude. It is now possible to analyse individual seeds or tiny fragments of precious objects such as the Turin Shroud, which was dated at AD1260-1390.

4.2 The Rb-Sr method

Trace amounts of Rb and Sr are found in most minerals as substitutions for major elements with similar chemical properties. Rb is an alkali metal that forms single valent positive ions with an ionic radius of 1.48 Å, which is similar to K⁺ (1.33 Å). Rb is therefore frequently found in K-bearing minerals such as micas, K-feldspar and certain clay minerals. Strongly evolved alkalic rocks such as syenites, trachites and rhyolites often contain high Rb concentrations. Rb contains two isotopes of constant abundance: ⁸⁵Rb (72.1854%) and ⁸⁷Rb (27.8346%). Sr is an alkaline earth metal that forms bivalent positive ions with a radius of 1.13 Å, similar to Ca²⁺ (ionic radius 0.99 Å). It therefore substitutes Ca²⁺ in many minerals such as plagioclase, apatite, gypsum and calcite in sites with 8 neighbours, but not in pyroxene where Ca²⁺ has a coordination number of 6. Native Sr²⁺ can also substitute K⁺ in feldspars (where radiogenic Sr is expected to be found), but this substitution is limited and requires the simultaneous replacement of Si⁴⁺ by Al³⁺ in order to preserve electric neutrality. Sr therefore predominantly occurs in Ca-rich undifferentiated rocks such as basalts. Sr contains four isotopes (⁸⁴Sr, ⁸⁶Sr, ⁸⁷Sr and ⁸⁸Sr) with variable abundance due to the variable amount of radiogenic ⁸⁷Sr. However, the non-radiogenic ⁸⁴Sr/⁸⁶Sr and ⁸⁶Sr/⁸⁸Sr-ratios are constant with values of 0.056584 and 0.1194, respectively. The Rb-Sr chronometer is based on the radioactive decay of ⁸⁷Rb to ⁸⁷Sr:



Where ν indicates an antineutrino. The number of radiogenic ⁸⁷Sr atoms produced by this reaction after a time t is given by:

$$^{87}\text{Sr}^* = ^{87}\text{Rb}(e^{\lambda_{87}t} - 1) \quad (4.4)$$

where ⁸⁷Rb is the actual number of ⁸⁷Rb atoms per unit weight and λ_{87} is the decay constant $1.42 \times 10^{-11} \text{ a}^{-1}$ ($t_{1/2} = 4.88 \times 10^{10} \text{ a}$). In addition to this radiogenic ⁸⁷Sr, most samples will also contain some ‘ordinary’ Sr. The total number of ⁸⁷Sr atoms measured is therefore given by:

$$^{87}\text{Sr} = ^{87}\text{Sr}^* + ^{87}\text{Sr}_o \quad (4.5)$$

with ⁸⁷Sr_o the initial ⁸⁷Sr present at the time of isotopic closure. Combining Equations 4.5 and 4.3, we obtain:

$$^{87}\text{Sr} = ^{87}\text{Sr}_o + ^{87}\text{Rb}(e^{\lambda_{87}t} - 1) \quad (4.6)$$

Dividing this by the non-radiogenic ⁸⁶Sr yields

$$\frac{^{87}\text{Sr}}{^{86}\text{Sr}} = \left(\frac{^{87}\text{Sr}}{^{86}\text{Sr}} \right)_o + \frac{^{87}\text{Rb}}{^{86}\text{Sr}}(e^{\lambda_{87}t} - 1) \quad (4.7)$$

The method can be applied to single minerals or to whole rocks. Given the very long half life, the optimal time scale ranges from the formation of the solar system to the late Palaeozoic (300-400 Ma). To measure a Rb/Sr age, the weight percentage of Rb is measured by means

of X-ray fluorescence, ICP-OES or similar techniques, and the $^{87}\text{Sr}/^{86}\text{Sr}$ ratio is determined by mass spectrometry (isotope dilution). The $^{87}\text{Rb}/^{86}\text{Sr}$ -ratio is then calculated as:

$$\frac{^{87}\text{Rb}}{^{86}\text{Sr}} = \frac{\text{Rb} \text{ Ab}(^{87}\text{Rb}) A(\text{Sr})}{\text{Sr} \text{ Ab}(^{86}\text{Sr}) A(\text{Rb})} \quad (4.8)$$

Where $\text{Ab}(\cdot)$ signifies ‘abundance’ and $A(\cdot)$ ‘atomic weight’.

4.3 Isochrons

Equation 4.8 can be used in one of two ways. A first method is to use an assumed value for $(^{87}\text{Sr}/^{86}\text{Sr})_0$, based on the geological context of the sample. This method is only reliable for samples with a high Rb/Sr ratio (e.g., biotite) because in that case, a wrong value for $(^{87}\text{Sr}/^{86}\text{Sr})_0$ has only a minor effect on the age. A second and much better method is to analyse several minerals of the same sample and plot them on a $(^{87}\text{Rb}/^{86}\text{Sr})$ vs. $(^{87}\text{Sr}/^{86}\text{Sr})$ diagram (Figure 4.1). Due to Equation 4.7, this should form a linear array (the so-called *isochron*) with slope $(e^{\lambda_{87}t} - 1)$ and intercept $(^{87}\text{Sr}/^{86}\text{Sr})_0$. Both parameters can be determined by linear regression, allowing us to quantify the ‘goodness of fit’ of the data and obviating the need to assume any initial Sr-ratios.

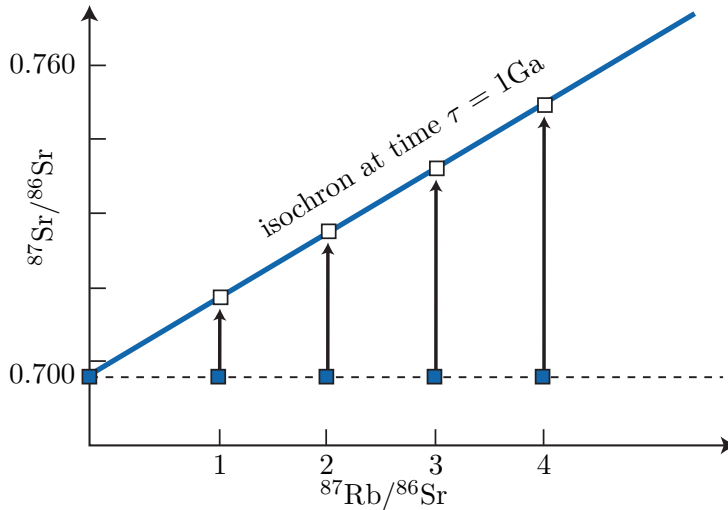


Figure 4.1: Schematic evolution of the $^{87}\text{Sr}/^{86}\text{Sr}$ -system as a function of time for multiple aliquots of a hypothetical sample with initial ratio $(^{87}\text{Sr}/^{86}\text{Sr})_0 = 0.700$. The slope of the isochron is a function of the age as per Equation 4.7 (modified from Allègre, 2008).

4.4 The Sm-Nd method

The elements Neodymium ($Z=60$) and Samarium ($Z=62$) are so-called ‘rare earth elements’. All elements of this family have similar chemical properties. They nearly all form $3+$ ions of roughly equal albeit slightly decreasing size with atomic number. The ionic radius of Nd and Sm is 1.08 and 1.04 Å, respectively. As the name suggests, rare earth elements rarely form the major constituents of minerals. One notable exception is monazite, which is a rare earth phosphate. In most cases, the rare earth elements are found in trace amounts of up to 0.1% in apatite $[\text{Ca}_5(\text{PO}_4)_3(\text{OH}, \text{Cl}, \text{F})]$ and zircon $[\text{ZrSiO}_4]$. Both Sm and Nd are slightly enriched in feldspar, biotite and apatite and thus tend to be found in higher concentrations in differentiated (alkalic) magmatic rocks.

Because their chemical properties are so similar, geological processes are rarely capable of fractionating the Sm and Nd concentrations. Therefore, the Sm/Nd ratio in most rocks generally falls in a narrow range of 0.1 to 0.5 (the Sm/Nd ratio of the solar system being 0.31). One exception is garnet, in which Sm/Nd ratios > 1 have been found. Partial melting of mafic minerals such as pyroxene and olivine produces lower Sm/Nd ratios in the fluid phase than the solid residue. The Sm/Nd ratio of magmatic rocks therefore decreases with increasing differentiation.

Natural Sm contains seven naturally occurring isotopes, three of which are radioactive (^{147}Sm , ^{148}Sm and ^{149}Sm). Only ^{147}Sm has a sufficiently short half life to be useful for geochronology. Nd also contains seven isotopes, of which only one is radioactive (^{144}Nd) but with a very long half life. ^{143}Nd is the radiogenic daughter of ^{147}Sm and is formed by α -decay. This forms the basis of the Sm-Nd chronometer. Analogous to the Rb-Sr method (Equation 4.4), we can write:

$$^{143}\text{Nd}^* = ^{147}\text{Sm}(e^{\lambda_{147}t} - 1) \quad (4.9)$$

Hence:

$$t = \frac{1}{\lambda_{147}} \ln \left(\frac{^{143}\text{Nd}^*}{^{147}\text{Sm}} + 1 \right) \quad (4.10)$$

With $\lambda_{147} = 6.54 \times 10^{-12} \text{a}^{-1}$ ($t_{1/2} = 1.06 \times 10^{11} \text{a}$). Since most samples contain some initial Nd, the preferred way to calculate Sm/Nd ages is by analysing several minerals in a rock and create an isochron, similar to the Rb/Sr method (Section 4.3):

$$\frac{^{143}\text{Nd}}{^{144}\text{Nd}} = \left(\frac{^{143}\text{Nd}}{^{144}\text{Nd}} \right)_0 + \frac{^{147}\text{Sm}}{^{144}\text{Nd}} (e^{\lambda_{147}t} - 1) \quad (4.11)$$

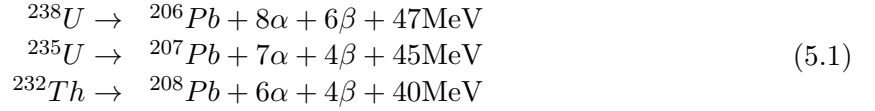
All measurements are done by mass spectrometry using isotope dilution. Because of the identical atomic masses of ^{147}Sm and ^{147}Nd , it is necessary to perform a chemical separation between Sm and Nd prior to analysis.

The Sm/Nd method is generally applied to basic and ultrabasic igneous rocks (basalt, peridotite, komatiite) of Precambrian to Palaeozoic age. The method thus complements the Rb/Sr method, which is preferentially applied to acidic rock types. The Sm/Nd method can also be applied to high grade metamorphic rocks (granulites, eclogites) as well as meteorites (shergottites, nakhlites). Since the rare earths are significantly less mobile than Rb and Sr, the Sm/Nd is more reliable in rocks that have been disturbed by weathering or metamorphism.

Chapter 5

The U-Pb system

U and Th are found on the extremely heavy end of the Periodic Table of Elements. All their isotopes are radioactive and exhibit α -decay and sometimes even spontaneous fission (see Section 7.2). ^{232}Th , ^{235}U and ^{238}U each form the start of long decay series comprising multiple α - and β emissions which eventually produce various isotopes of Pb:



Each of these three decay series is unique, i.e. no isotope occurs in more than one series (Figure 2.2). Furthermore, the half life of the parent isotope is much longer than any of the intermediary daughter isotopes, thus fulfilling the requirements for secular equilibrium (Section 2.4). We can therefore assume that the ^{206}Pb is directly formed by the ^{238}U , the ^{207}Pb from the ^{235}U and the ^{208}Pb from the ^{232}Th . Several chronometers are based on the α -decay of U and Th:

- The U-Th-Pb method (Section 5.1)
- The Pb-Pb method (Section 5.2)
- The U-Th-He method (Section 7.1)

5.1 The U-(Th-)Pb method

Natural Pb consists of four isotopes ^{204}Pb , ^{206}Pb , ^{207}Pb and ^{208}Pb . The ingrowth equations for the three radiogenic Pb isotopes are given by:

$$\begin{aligned} ^{206}\text{Pb}^* &= ^{238}\text{U} (e^{\lambda_{238}t} - 1) \\ ^{207}\text{Pb}^* &= ^{235}\text{U} (e^{\lambda_{235}t} - 1) \\ ^{208}\text{Pb}^* &= ^{232}\text{Th} (e^{\lambda_{232}t} - 1) \end{aligned} \quad (5.2)$$

With $\lambda_{238} = 1.55125 \times 10^{-10} \text{a}^{-1}$ ($t_{1/2} = 4.468 \text{ Gyr}$), $\lambda_{235} = 9.8485 \times 10^{-10} \text{a}^{-1}$ ($t_{1/2} = 703.8 \text{ Myr}$), and $\lambda_{232} = 0.495 \times 10^{-10} \text{a}^{-1}$ ($t_{1/2} = 14.05 \text{ Gyr}$). The corresponding age equations are:

$$\begin{aligned} t_{206} &= \frac{1}{\lambda_{238}} \ln \left(\frac{^{206}\text{Pb}^*}{^{238}\text{U}} + 1 \right) \\ t_{207} &= \frac{1}{\lambda_{235}} \ln \left(\frac{^{207}\text{Pb}^*}{^{235}\text{U}} + 1 \right) \\ t_{208} &= \frac{1}{\lambda_{232}} \ln \left(\frac{^{208}\text{Pb}^*}{^{232}\text{Th}} + 1 \right) \end{aligned} \quad (5.3)$$

Some igneous minerals (notably zircon) conveniently incorporate lots of U and virtually no Pb upon crystallisation. For those minerals, the non-radiogenic Pb can be safely neglected (at least for relatively young ages), so that we can assume that $Pb \approx Pb^*$. This assumption cannot be made for other minerals, young ages, and high precision geochronology. In those cases, the inherited component (aka ‘common Pb’) needs to be quantified, which is done by normalising to non-radiogenic ^{204}Pb :

$$\begin{aligned}\frac{^{206}\text{Pb}}{^{204}\text{Pb}} &= \left(\frac{^{206}\text{Pb}}{^{204}\text{Pb}} \right)_o + \frac{^{238}\text{U}}{^{204}\text{Pb}} (e^{\lambda_{238}t} - 1) \\ \frac{^{207}\text{Pb}}{^{204}\text{Pb}} &= \left(\frac{^{207}\text{Pb}}{^{204}\text{Pb}} \right)_o + \frac{^{235}\text{U}}{^{204}\text{Pb}} (e^{\lambda_{235}t} - 1) \\ \frac{^{208}\text{Pb}}{^{204}\text{Pb}} &= \left(\frac{^{208}\text{Pb}}{^{204}\text{Pb}} \right)_o + \frac{^{232}\text{Th}}{^{204}\text{Pb}} (e^{\lambda_{232}t} - 1)\end{aligned}\tag{5.4}$$

where $\left(\frac{x\text{Pb}}{^{204}\text{Pb}} \right)_o$ stands for the common Pb component for isotope x. The corresponding age equations then become:

$$\begin{aligned}t_{206} &= \frac{1}{\lambda_{238}} \ln \left(\frac{\left(\frac{^{206}\text{Pb}}{^{204}\text{Pb}} \right) - \left(\frac{^{206}\text{Pb}}{^{204}\text{Pb}} \right)_o}{\frac{^{238}\text{U}}{^{204}\text{Pb}}} + 1 \right) \\ t_{207} &= \frac{1}{\lambda_{235}} \ln \left(\frac{\left(\frac{^{207}\text{Pb}}{^{204}\text{Pb}} \right) - \left(\frac{^{207}\text{Pb}}{^{204}\text{Pb}} \right)_o}{\frac{^{235}\text{U}}{^{204}\text{Pb}}} + 1 \right) \\ t_{208} &= \frac{1}{\lambda_{232}} \ln \left(\frac{\left(\frac{^{208}\text{Pb}}{^{204}\text{Pb}} \right) - \left(\frac{^{208}\text{Pb}}{^{204}\text{Pb}} \right)_o}{\frac{^{232}\text{Th}}{^{204}\text{Pb}}} + 1 \right)\end{aligned}\tag{5.5}$$

U-Pb dating grants access to two separate geochronometers ($^{206}\text{Pb}/^{238}\text{U}$ and $^{207}\text{Pb}/^{235}\text{U}$) based on different isotopes of the same parent-daughter pair (i.e. U & Pb). This built-in redundancy provides a powerful internal quality check which makes the method arguably the most robust and reliable dating technique in the geological toolbox. The initial Pb composition can either be determined by analysing the Pb composition of a U-poor mineral (e.g., galena or feldspar) or by applying the isochron method to samples with different U and Th concentrations. As is the case for any isotopic system, the system needs to remain ‘closed’ in order to yield meaningful isotopic ages. This sometimes is not the case, resulting in a loss of Pb and/or U. Such losses cause the $^{206}\text{Pb}/^{238}\text{U}$ - and $^{207}\text{Pb}/^{235}\text{U}$ -clocks to yield different ages. Note that isotopic closure is required for all intermediary isotopes as well. Critical isotopes are the highly volatile ^{226}Rn ($t_{1/2}=1.6\text{ka}$) and ^{222}Rn ($t_{1/2}=3.8\text{d}$). Initially, the U-Pb method was applied to U-ores, but nowadays it is predominantly applied to accessory minerals such zircon and, to a lesser extent, apatite, monazite and allanite.

5.2 The Pb-Pb method

The $^{207}\text{Pb}/^{206}\text{Pb}$ method is based on the U-Pb method and is obtained by dividing the two U-Pb members of Equation 5.2 (or 5.4), and taking into account that the average natural $^{238}\text{U}/^{235}\text{U}$ -ratio is 137.818:

$$\frac{^{207}\text{Pb}^*}{^{206}\text{Pb}^*} = \frac{\left(\frac{^{207}\text{Pb}}{^{204}\text{Pb}} \right) - \left(\frac{^{207}\text{Pb}}{^{204}\text{Pb}} \right)_o}{\left(\frac{^{206}\text{Pb}}{^{204}\text{Pb}} \right) - \left(\frac{^{206}\text{Pb}}{^{204}\text{Pb}} \right)_o} = \frac{1}{137.818} \frac{e^{\lambda_{235}t} - 1}{e^{\lambda_{238}t} - 1}\tag{5.6}$$

The left hand side of this equation contains only Pb isotopic ratios. Note that these are *only* a function of time. Equation 5.6 has no direct solution and must be solved iteratively. The Pb-Pb method has the following advantages over conventional U-Pb dating:

- There is no need to measure uranium.
- The method is insensitive to recent loss of U and even Pb, because this would not affect the isotopic ratio of the Pb.

In practice, the Pb-Pb method is rarely applied by itself but is generally combined with the U-Pb technique. The expected $(^{207}\text{Pb}/^{206}\text{Pb})^*$ -ratio for recently formed rocks and minerals can be calculated from Equation 5.6 by setting $t \rightarrow 0$:

$$\left(\frac{^{207}\text{Pb}}{^{206}\text{Pb}}\right)_p^* = \frac{\lambda_{235}}{137.818\lambda_{238}} = 0.04607 \quad (5.7)$$

This ratio was progressively higher as one goes back further in time. It was ≈ 0.6 during the formation of Earth.

5.3 Concordia

It sometimes happens that the U-Th-Pb trio of chronometers does not yield mutually consistent ages. It is then generally found that $t_{208} < t_{206} < t_{207} < t_{207/206}$ which, again, shows that the Pb-Pb clock is least sensitive to open system behaviour. From Equation 5.2, we find that:

$$\begin{aligned} \frac{^{206}\text{Pb}^*}{^{238}\text{U}} &= e^{\lambda_{238}t} - 1 \text{ and} \\ \frac{^{207}\text{Pb}^*}{^{235}\text{U}} &= e^{\lambda_{235}t} - 1 \end{aligned} \quad (5.8)$$

If we plot those $^{206}\text{Pb}^*/^{238}\text{U}$ - and $^{207}\text{Pb}^*/^{235}\text{U}$ -ratios which yield the same ages (t) against one another, they form a so-called ‘concordia’ curve. The concordia diagram is a very useful tool for investigating and interpreting disruptions of the U-Pb system caused by ‘episodic lead loss’. This means that a mineral (of age T_o , say) has lost a certain percentage of its radiogenic Pb at a time T_1 after its formation (e.g., during metamorphism), after which the system closes again and further accumulation of radiogenic Pb proceeds normally until the present. On the concordia diagram of multiple aliquots of a sample, this scenario will manifest itself as a linear array of datapoints connecting the concordant $^{206}\text{Pb}^*/^{238}\text{U}$ - $^{207}\text{Pb}^*/^{235}\text{U}$ composition expected at T_o with that expected at T_1 . With time, the data shift further away from the origin. The upper intercept of the linear array (aka *discordia* line) can be used to estimate the crystallisation age, whereas the lower intercept yields the age of metamorphism. The greater the distance from the expected composition at t , the greater the degree of Pb loss and the greater the linear extrapolation error on the crystallisation age (Figure 5.1).

5.4 Detrital geochronology

Zircon (ZrSiO_4) is a common U-Th-bearing accessory mineral in acidic igneous rocks, which form the main proto-sources of the siliciclastic sediments. Zircon is a very durable mineral that undergoes minimal chemical alteration or mechanical abrasion. Therefore, zircon crystals can be considered time capsules carrying the igneous and metamorphic history of their proto-sources. The probability distribution of a representative sample of zircon U-Pb ages from a detrital population can serve as a characteristic fingerprint that may be used to trace the flow of sand through sediment routing systems. As a provenance tracer, zircon U-Pb data are less susceptible to winnowing effects than conventional petrographic techniques. Using modern microprobe technology (SIMS and LA-ICP-MS, see Chapter 3.1), it is quite easy to date, say, a hundred grains of zircon in a matter of just a few hours. Due to the robustness of zircons as a

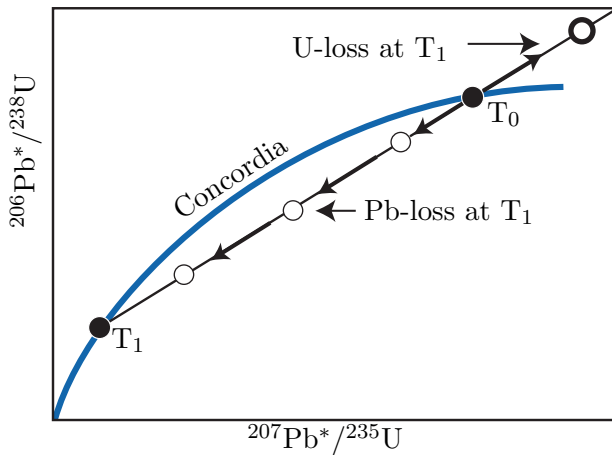


Figure 5.1: ‘Wetherill’ concordia diagram showing concordant (filled symbols) and discordant (empty symbols) analyses affected by different degrees of Pb (or U) loss (modified from Allègre, 2008).

tracer of sedimentary provenance, and the relative ease of dating them, the use of detrital zircon U-Pb geochronology has truly exploded in recent years. A literature survey using the keywords ‘detrital’, ‘zircon’, and ‘provenance’ indicates that the proliferation of detrital zircon studies has followed an exponential trend, with the number of publications doubling roughly every five years over the past two decades. At present, nearly a thousand detrital zircon publications appear each year.

An extensive survey of late Archaean sandstones from the Jack Hills in Australia have revealed a subpopulation of detrital zircons with Hadean (4.1-4.2 Ga) U-Pb ages. These are the oldest terrestrial minerals known to science, predating the oldest igneous rocks by 300 million years. The isotopic composition of oxygen, hafnium and other elements in the zircon represents a unique window into the earliest stages of Earth evolution. They indicate that liquid water was present on the surface of our planet early on in its history. This isotopic evidence is corroborated by the geological observation that the Hadean zircons are preserved in fluvial deposits.

Chapter 6

The K–Ar system

Potassium has three naturally occurring isotopes: ^{39}K , ^{40}K and ^{41}K . ^{40}K is radioactive and undergoes branched decay to ^{40}Ca (by electron emission $\lambda_{\beta-} = 4.962 \times 10^{-10} \text{yr}^{-1}$) and ^{40}Ar (by electron capture $\lambda_e = 0.581 \times 10^{-10} \text{yr}^{-1}$) with a combined half life of 1.248 billion years. The positron emission mechanism mentioned in Chapter 2.2 has an extremely long half life and can therefore safely be neglected. In addition to ^{40}Ar , argon has two more stable isotopes: ^{36}Ar and ^{38}Ar . Argon makes up $\sim 1\%$ of the terrestrial atmosphere, with a fixed isotopic composition of $^{40}\text{Ar}/^{36}\text{Ar} = 298.5$ and $^{38}\text{Ar}/^{36}\text{Ar} = 0.187$. The argon contained in K-bearing minerals is made up of a mixture of radiogenic ($^{40}\text{Ar}^*$) and non-radiogenic gas ($^{40}\text{Ar}_o$):

$$\begin{aligned} ^{40}\text{Ar} &= ^{40}\text{Ar}_o + ^{40}\text{Ar}^* \\ \text{where } ^{40}\text{Ar}^* &= \frac{\lambda_e}{\lambda} ^{40}\text{K} (e^{\lambda t} - 1) \end{aligned} \quad (6.1)$$

with λ the total decay constant of ^{40}K ($\lambda = \lambda_e + \lambda_{\beta-} = 5.543 \times 10^{-10} \text{yr}^{-1}$).

6.1 K-Ar dating

The $^{40}\text{K} \rightarrow ^{40}\text{Ar}^*$ decay scheme forms the basis of the K-Ar geochronometer, with the following age equation:

$$t = \frac{1}{\lambda} \ln \left[1 + \frac{\lambda}{\lambda_e} \left(\frac{^{40}\text{Ar}^*}{^{40}\text{K}} \right) \right] \quad (6.2)$$

Taking into account the ‘contaminated’ (aka ‘excess’ or ‘inherited’) argon component $^{40}\text{Ar}_o$ and analysing several cogenetic rocks or minerals with different K (and therefore $^{40}\text{Ar}^*$) contents, an *isochron* equation can be formed by division through ^{36}Ar :

$$\frac{^{40}\text{Ar}}{^{36}\text{Ar}} = \left(\frac{^{40}\text{Ar}}{^{36}\text{Ar}} \right)_o + \frac{\lambda_e}{\lambda} \frac{^{40}\text{K}}{^{36}\text{Ar}} (e^{\lambda t} - 1) \quad (6.3)$$

which can be solved for t . Alternatively, we can simply assume that all the inherited argon has an atmospheric origin, so that $(^{40}\text{Ar}/^{36}\text{Ar})_o = 298.5$.

6.2 $^{40}\text{Ar}/^{39}\text{Ar}$ dating

From an analytical perspective, K-Ar dating is a two step process. Because K (an alkali metal) and Ar (a noble gas) cannot be measured on the same analytical equipment, they must be analysed separately on two different aliquots of the same sample. This limitation is overcome by the $^{40}\text{Ar}/^{39}\text{Ar}$ technique, which is a clever variation of the K-Ar method. The idea is to

subject the sample to neutron irradiation and convert a small fraction of the ^{39}K to synthetic ^{39}Ar , which has a half life of 269 years. The age equation can then be rewritten as follows:

$$t_x = \frac{1}{\lambda} \ln \left[1 + J \left(\frac{{}^{40}\text{Ar}^*}{{}^{39}\text{Ar}} \right)_x \right] \quad (6.4)$$

where ‘x’ stands for ‘sample’ and J is a constant of proportionality which encapsulates the efficiency of the ^{39}K (n,p) ^{39}Ar reaction and into which the factor λ/λ_e is folded as well. The J-value can be determined by analysing a standard of known age t_s which was co-irradiated with the sample:

$$t_s = \frac{1}{\lambda} \ln \left[1 + J \left(\frac{{}^{40}\text{Ar}^*}{{}^{39}\text{Ar}} \right)_s \right] \quad (6.5)$$

In which the subscript ‘s’ stands for ‘standard’. The great advantage of equation 6.4 over 6.2 is that all measurements can be completed on the same aliquot and using a single instrument, namely a noble gas mass spectrometer, which can analyse extremely small (down to μg -sized) samples.

The $^{40}\text{Ar}/^{39}\text{Ar}$ -method also allows the analyst to investigate the extent of *argon loss* by means of stepwise heating experiments. This is done by degassing the sample under ultra-high vacuum conditions in a resistance furnace. At low temperatures, the weakly bound Ar is released, whereas the strongly bound Ar is released from the crystal lattice at high temperatures until the sample eventually melts. Plotting the *apparent ages* against the cumulative fraction of ^{39}Ar released yields an $^{40}\text{Ar}/^{39}\text{Ar}$ age spectrum (Figure 6.1). If a rock or mineral has remained closed since its formation, the $^{40}\text{Ar}/^{39}\text{Ar}$ -ratio should remain constant over the course of the different heating steps, forming an ‘age plateau’. More complex (e.g. rising) release spectra, on the other hand, are diagnostic of complex thermal histories featuring partial argon loss. ‘saddle’ shaped release spectra are indicative of ‘excess’ argon. The composition of the inherited argon gas can be determined using a variant of the isochron method, assuming that all ^{36}Ar is inherited:

$$\frac{{}^{40}\text{Ar}}{{}^{36}\text{Ar}} = \left(\frac{{}^{40}\text{Ar}}{{}^{36}\text{Ar}} \right)_o + \frac{{}^{39}\text{Ar}}{{}^{36}\text{Ar}} \frac{e^{\lambda t} - 1}{J} \quad (6.6)$$

If the Ar contamination is constant throughout the entire sample, then the $\frac{{}^{40}\text{Ar}}{{}^{36}\text{Ar}}$ -measurements will be arranged along a linear trend whose slope is a function of $\frac{{}^{40}\text{Ar}^*}{{}^{39}\text{Ar}}$ and, hence, the age.

6.3 Applications

The K-Ar and $^{40}\text{Ar}/^{39}\text{Ar}$ -methods are some of the most widely used geochronometers and important tools in the calibration of the geologic time scale. The method is applicable to rocks and minerals $> 10^6\text{yr}$. Obviously, younger materials require more careful treatment of the inherited argon components.

- Magmatic rocks: formation ages can only be obtained for rapidly cooled volcanic rocks, using either mineral separates (sanidine, biotite, hornblende) or whole rocks. Pyroclastics and obsidian may yield reliable ages only if they are unaltered and contain little non-radiogenic argon. Plutonic rocks typically cool much slower than volcanic rocks and generally yield cooling ages rather than formation ages.

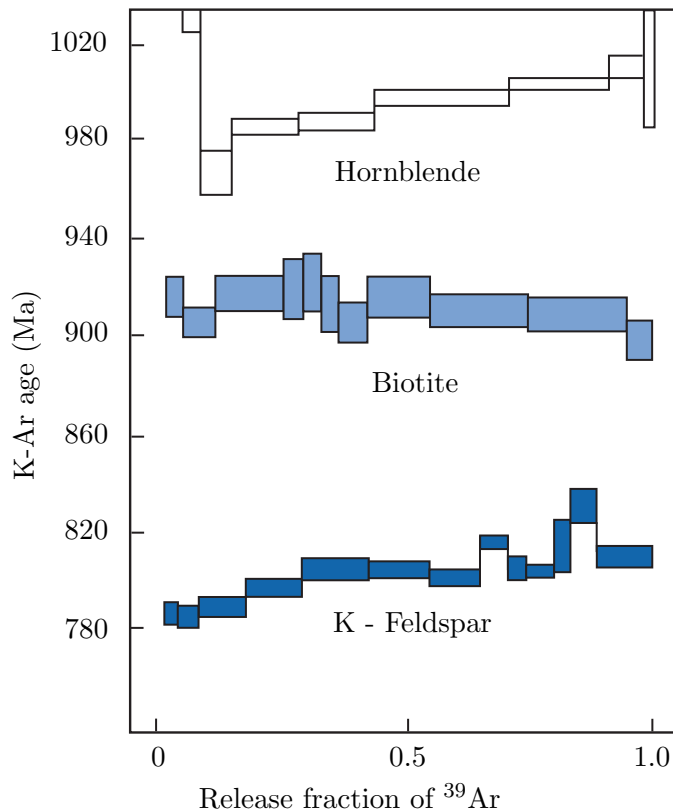


Figure 6.1: $^{40}\text{Ar}/^{39}\text{Ar}$ age spectra obtained by stepwise heating of three different K-bearing minerals. Biotite exhibits a flat ‘plateau’, indicating a simple history of rapid crystallisation and/or cooling. K-feldspar shows a rising age spectrum, consistent with a more complex evolution comprising multiple growth phases and/or thermal resetting. Finally, hornblende shows a ‘U-shaped’ release spectrum in which the first heating step releases a large amount of ‘excess’ argon (modified from Allègre, 2008).

- Sedimentary rocks: K-Ar dating of *authigenic* mineral phases has often been attempted but remains difficult. Glauconite has been used successfully in some cases. Dating detrital minerals such as white mica (muscovite, phengite) in fluvial sediments is frequently used to study the metamorphic history of the hinterland.
- Metamorphic rocks: pelitic metamorphic rocks tend to be rich in K-bearing micas and amphiboles, which can easily be dated with the K-Ar and $^{40}\text{Ar}/^{39}\text{Ar}$ methods, but require careful interpretation. In high grade metamorphic terranes, the apparent ages can either reflect the metamorphic crystallisation history or the postmetamorphic cooling history. Low grade metamorphic terranes, on the other hand, carry a risk of containing inherited argon components from previous evolutionary stages.

Chapter 7

Thermochronology

The temperature sensitivity of the K-Ar system (Section 6) is a characteristic feature not only of this method, but of a separate class of geochronometers known as ‘thermochronometers’. The most important of these methods are the U-Th-He 7.1 and fission track 7.2 techniques, which are becoming increasingly popular as a means of investigating Earth surface processes.

7.1 The U-Th-He method

When U and Th decay to various isotopes of Pb (Section 5.1), they do so by α -emission (Section 2.2). When α particles acquire electrons, they become helium atoms. Thus, not only Pb content, but also the He content increases relative to U and Th through time, forming the basis of the U-Th-He chronometer:

$$[{}^4\text{He}] = \left[8 \frac{137.818}{138.818} (e^{\lambda_{238}t} - 1) + 7 \frac{1}{138.818} (e^{\lambda_{235}t} - 1) \right] [\text{U}] + 6(e^{\lambda_{232}t} - 1)[\text{Th}] + 0.1499(e^{\lambda_{147}t} - 1)[\text{Sm}] \quad (7.1)$$

where $[{}^4\text{He}]$, $[\text{U}]$, $[\text{Th}]$ and $[\text{Sm}]$ are concentrations in atoms or moles per unit mass or volume. The values ‘8’, ‘7’ and ‘6’ refer to the number of α -particles produced in the decay chains of ${}^{238}\text{U}$, ${}^{235}\text{U}$ and ${}^{232}\text{Th}$, respectively (Figure 2.2), 137.818 is the ${}^{238}\text{U}/{}^{235}\text{U}$ ratio of naturally occurring uranium in accessory minerals, and the last term accounts for the (often negligible) accumulation of helium by Sm-decay (Section 4.4). It was Ernest Rutherford who first proposed that the U-Th-He decay scheme could be used as an absolute dating technique, making it the oldest radiometric chronometer. Early experiments on uraninite (UO_2) by Robert John Strutt (4th Baron Rayleigh) at Imperial College London in 1905 yielded ages that were systematically too young. This was correctly attributed to the volatile nature of the helium atom, which diffuses out of most minerals at low temperatures and therefore yields only *minimum ages*. As a result, the method was largely abandoned until 1987, when American geochronologist Peter Zeitler realised that this ‘leaky’ behaviour provided a powerful means of reconstructing the thermal evolution of rocks and minerals.

Let $C(x,y,z)$ be the He-concentration as a function of the spatial coordinates x , y and z . The evolution of C with time (t) is given by the diffusion equation (‘Fick’s law’):

$$\frac{\partial C}{\partial t} = D \left(\frac{\partial^2 C}{\partial x^2} + \frac{\partial^2 C}{\partial y^2} + \frac{\partial^2 C}{\partial z^2} \right) \quad (7.2)$$

Where D is the ‘diffusion coefficient’, which varies exponentially with temperature (T) according to the ‘Arrhenius Law’:

$$D = D_0 e^{-\frac{E_a}{RT}} \quad (7.3)$$

with D_0 the ‘frequency factor’, E_a the ‘activation energy’ and R the ideal gas constant (8.3144621 J/mol.K). By taking the logarithm of both sides of Equation 7.3, we obtain (Figure 7.1):

$$\ln(D) = \ln(D_0) - \frac{E_a}{RT} \quad (7.4)$$

Both the frequency factor and the activation energy can be determined from *diffusion experiments*, in which a He-bearing mineral is subjected to a step-heating experiment similar to the kind we saw in the $^{40}\text{Ar}/^{39}\text{Ar}$ method (Section 6.2).

Let us now consider the situation of a mineral which (a) accumulates He through radioactive decay of U and Th, (b) loses He by thermal diffusion, and (c) undergoes monotonic cooling at a variable rate dT/dt . At high temperatures, the He will be lost quickly but as time progresses, the thermal diffusion becomes increasingly sluggish until the He is eventually ‘locked’ into the crystal lattice and the isotopic system is effectively *closed*. If the thermal history is so that $1/T$ increases linearly with time, then it is possible to calculate an equivalent ‘closure temperature’ T_c . This is known as ‘Dodson’s equation’:

$$\frac{E_a}{RT_c} = \ln \left(\frac{ART_c^2 D_0 / r^2}{E_a dT/dt} \right) \quad (7.5)$$

where r = is the effective grain size (radius) of the mineral and A is a geometric factor (55 for a sphere, 27 for a cylinder and 8.7 for a plane sheet). Thus the U-Th-He age calculated at the end of the aforementioned thermal history equals that which would have been obtained if He accumulated linearly since the rock passed through T_c .

Although the closure temperature concept is an oversimplification of reality, it has great intuitive appeal. Consider, for example, a vertical transect in a rapidly exhuming mountain range. The *apparent* U-Th-He ages along such a transect are approximately given by the time elapsed since the respective rocks have passed through T_c . For apatite [$\text{Ca}_5(\text{PO}_4)_3(\text{OH}, \text{F}, \text{Cl})$], this is $\sim 60^\circ\text{C}$, which corresponds to a depth (assuming a thermal gradient of $30^\circ\text{C}/\text{km}$) of 1.5-2km. Thus, the rocks at the high elevations along the transect will have passed through T_c before those collected at the bottom of the transect, and the corresponding U-Th-He ages will therefore increase with elevation. Moreover, the rate of increase of age increase with elevation can be used to estimate the *exhumation rate* of the orogen.

7.2 Fission tracks

In addition to α , β and γ decay, which form the basis of the U-Th-Pb (Section 5) and U-Th-He (Section 7.1) methods, a tiny fraction (1/1,000,000) of the ^{238}U atoms decay by *spontaneous fission* (Section 2.2). In this decay mechanism, the parent nuclide (i.e., ^{238}U) decays into two daughter nuclides of roughly equal mass (e.g., Ba and Kr). These two particles carry a large amount of energy (~ 170 MeV) and, having a positive charge, strongly repel each other. Each of the two fission fragments travels through the crystal lattice of the host mineral, leaving a trail of damage behind. Although fission tracks can be directly observed by transmission electron microscopy (TEM), a more practical approach is to etch (a polished surface of) the host mineral

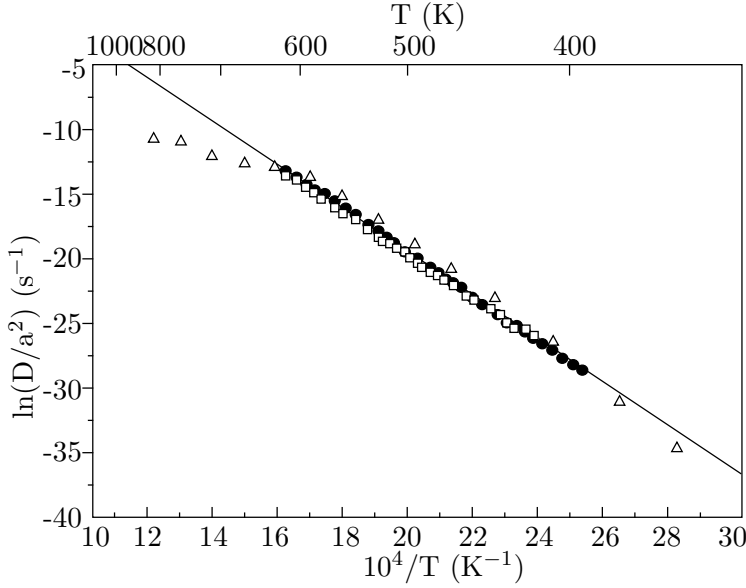


Figure 7.1: ‘Arrhenius’ diagram of three step-heating experiments of ^4He in apatite, showing simple diffusion behaviour in agreement with Equation 7.3. Extrapolating the linear trend to geological time scales yields a ‘closure temperature’ of $\sim 60^\circ\text{C}$ (Equation 7.5). Modified from Braun, Van Der Beek, and Batt (2006).

with acid. This enlarges the damage zones and makes it possible to count them under an ordinary petrographic microscope. The volume density n_s (in cm^{-3}) of the fission tracks is given by:

$$n_s = \frac{\lambda_f}{\lambda} [^{238}\text{U}] (e^{\lambda t} - 1) \quad (7.6)$$

where $[^{238}\text{U}]$ stands for the volume density the ^{238}U atoms, λ_f is the fission decay constant ($8.46 \times 10^{-17} \text{ yr}^{-1}$) and λ is the total decay constant of ^{238}U ($1.55125 \times 10^{-10} \text{ yr}^{-1}$, see Section 5). The (unobservable) volume density of the tracks is related to the (observable) surface density ρ_s (in cm^{-2}) by:

$$\rho_s = g_s L n_s \quad (7.7)$$

Where g_s is geometry factor ($g_s=1$ if determined on an internal and $g_s=1/2$ on an external surface) and L is the etchable length of a fission track ($\sim 15\mu\text{m}$). Rearranging Equation 7.6 for time:

$$t = \frac{1}{\lambda} \ln \left(\frac{\lambda}{\lambda_f} \frac{\rho_s}{[^{238}\text{U}] g_s L} + 1 \right) \quad (7.8)$$

In practice, $[^{238}\text{U}]$ is determined by irradiating the (etched) sample with thermal neutrons in a reactor. This irradiation induces synthetic fission of ^{235}U in the mineral (Equation 2.1). These tracks can be monitored by attaching a mica detector to the polished mineral surface and etching this monitor subsequent to irradiation (Figure 7.2). The surface density of the induced tracks in the mica detector (ρ_i) is a function of the nuclear cross section of the neutron-induced fission reaction on ^{235}U and the neutron fluence in the reactor, both of which are unknown. A pragmatic solution to this problem is found by irradiating the sample along with a standard of known age, and lumping all the unknown parameters together into a calibration factor (ζ), so that the age of the sample reduces to:

$$t = \frac{1}{\lambda} \ln \left(1 + \frac{g_i}{g_s} \lambda \zeta \rho_d \frac{\rho_s}{\rho_i} \right) \quad (7.9)$$

where $g_s = 1$, $g_i = 1/2$ and ρ_d is the surface density of the induced fission tracks in a dosimeter glass of known (and constant) U concentration. The latter value is needed to ‘recycle’ the ζ value from one irradiation batch to the next, as neutron fluences might vary through time, or

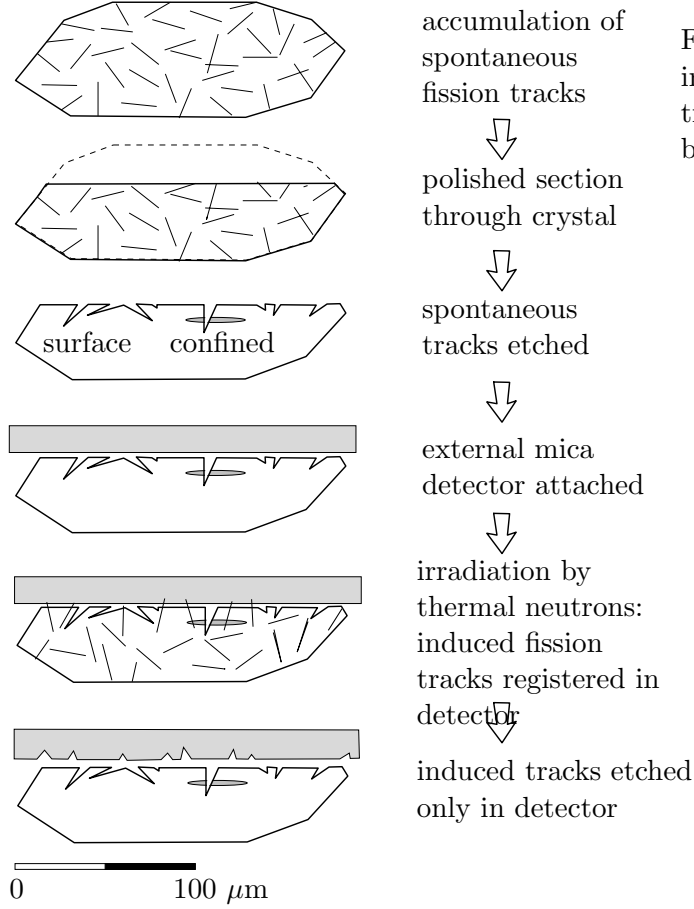


Figure 7.2: Schematic diagram illustrating the external detector method for fission track geochronology (modified from Galbraith, 2005).

within a sample stack.

Laboratory experiments have revealed that fission tracks are sensitive to heat. For example, it suffices that apatite is heated to 500°C for 1 hour for all the latent fission tracks to anneal. Moderate heating shortens the tracks and reduces their surface density and, hence, the apparent age of the sample. In boreholes, the apparent fission track age remains constant until a depth is reached where the ambient temperature is high enough for the tracks to be reduced in size and number. This region is called the *Partial Annealing Zone* (PAZ). Below the PAZ, no tracks are retained (Figure 7.3). The reduction of the surface density of the spontaneous tracks per unit time can be written as a function of temperature (T, in Kelvin):

$$\frac{d\rho_s}{dt} = -C\rho_s e^{-E_a/kT} \quad (7.10)$$

where C is a material constant, E_a is the activation energy for track shortening and k is the Boltzmann constant ($8.616 \times 10^{-5} \text{ eV/K}$). Integration of Equation 7.10 yields:

$$\ln \left(\frac{\rho_o}{\rho} \right) = C t e^{-E_a/kT} \quad (7.11)$$

where ρ_o is the initial track density prior to heating. Taking logarithms:

$$\ln(t) = \frac{E_a}{kT} + \ln \left[\ln \left(\frac{\rho_o}{\rho} \right) \right] - \ln(C) \quad (7.12)$$

For any given *retention coefficient* ρ_o/ρ , there exists a linear relationship between $\ln(t)$ and $1/T$. This is an *Arrhenius trend* similar to the one described by Equation 7.3 in the context of U-Th-He thermochronology. By extrapolating the Arrhenius diagram to long time scales ($t \sim 10^6$ yr), it is possible to calculate a ‘closure temperature’ T_c similar to that which is calculated for the U-Th-He system. For apatite, $T_c \approx 100^\circ\text{C}$, whereas for zircon, $T_c \approx 240^\circ\text{C}$.

If a sample has spent some of its time inside the PAZ, then the subpopulation of its fission tracks formed during that time will be shorter than those that subsequently formed above the PAZ. The probability distribution of the fission track lengths can be determined by measuring the distance between the two tips of a large number of (100, say) *horizontally confined* fission tracks under the optical microscope. Sophisticated inverse modelling algorithms have been developed to interpret these length distributions and extract continuous time-temperature (t-T) paths from them. Such modelling exercises have become an integral part of modern fission track studies.

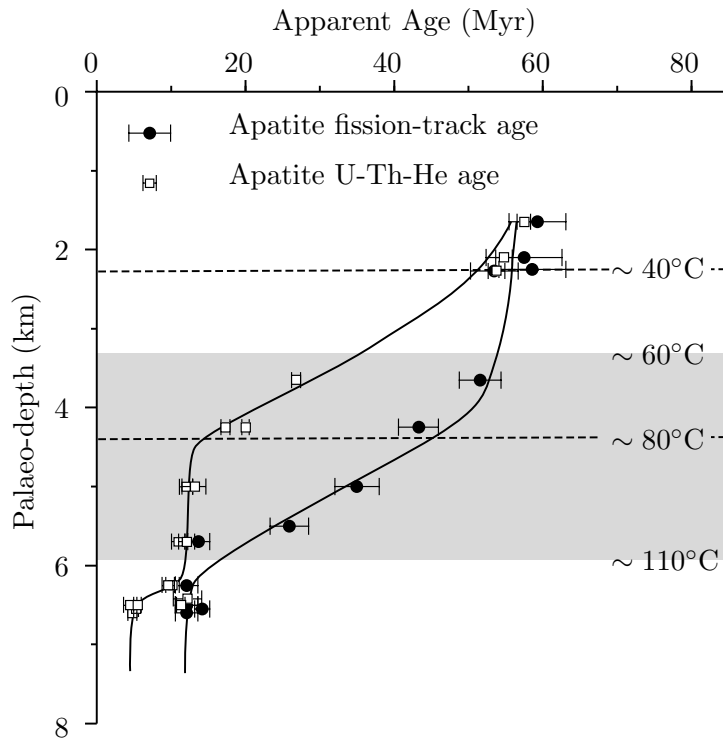


Figure 7.3: Vertical profile of U-Th-He and fission track ages in apatite, collected along the footwall of an exhumed normal fault block in the White Mountains of eastern California. Samples at the highest elevations have resided at shallow depths for up to 55 Myr. Dashed lines show the extent of the ‘Partial Retention Zone’ (PRZ), in which apatite has partially lost its radiogenic helium. The grey area indicates the ‘Partial Annealing Zone’, where fission tracks have been shortened. At low elevations, young ages are observed, indicating rapid exhumation by the normal fault at 12 Ma. Additionally, the U-Th-He data show a hint of a second exhumation phase at 5 Ma (modified from Stockli, Farley and Dumitru, 2000, *Geology* v. 28, no. 11, p. 983-986).

Chapter 8

U-series disequilibrium methods

In Section 2.4, we saw that the ^{235}U - ^{207}Pb and ^{238}U - ^{206}Pb decay series generally reach a state of *secular equilibrium*, in which the activity (expressed in decay events per unit time) of each intermediate daughter product is the same, so that:

$$D_n\lambda_n = \dots = D_2\lambda_2 = D_1\lambda_1 = P\lambda_P$$

as described by Equation 2.20. However, certain natural processes can disturb this equilibrium situation, such as chemical weathering, precipitation from a solution, (re-)crystallisation etc. This leads to two new types of chronometric systems:

1. An intermediate daughter isotope in the decay series is separated from its parent nuclide incorporated into a rock or sediment, and decays according to its own half life.
2. A parent nuclide has separated itself from its previous decay products and it takes some time for secular equilibrium to be re-established.

This idea is most frequently applied to the ^{238}U -decay series, notably ^{230}Th and ^{234}U . The first type of disequilibrium dating forms the basis of the ^{234}U - ^{238}U and ^{230}Th methods (Sections 8.1 and 8.2). The second forms the basis of the ^{230}Th - ^{238}U method (Section 8.3)

8.1 The ^{234}U - ^{238}U method

The activity ratio of ^{238}U to its third radioactive daughter ^{234}U in the world's oceans is $A(^{234}\text{U})/A(^{238}\text{U}) \equiv \gamma_o \approx 1.15$. The slight enrichment of the ^{234}U over ^{238}U is attributed to α -recoil of its immediate parent ^{234}Th and the fact that ^{234}U is more 'loosely bound' inside the crystal lattice of the host mineral, because it is preferentially seated in sites which have undergone radiation damage. Once the oceanic U is incorporated into the crystal structure of marine carbonates, the radioactive equilibrium gradually restores itself with time. The total activity of ^{234}U is made up of a component which is supported by secular equilibrium (and equals the activity of ^{238}U) and an 'excess' component, which decays with time:

$$A(^{234}\text{U}) = A(^{238}\text{U}) + A(^{234}\text{U})_o^x e^{-\lambda_{234}t} \quad (8.1)$$

where $A(^{234}\text{U})_o^x$ is the initial amount of excess ^{234}U and $\lambda_{234} = 2.8234 \times 10^{-6} \text{ yr}^{-1}$ ($t_{1/2} = 245.5 \text{ kyr}$). Let $A(^{234}\text{U})_o$ be the initial total ^{234}U activity. Then:

$$A(^{234}\text{U}) = A(^{238}\text{U}) + [A(^{234}\text{U})_o - A(^{238}\text{U})] e^{-\lambda_{234}t} \quad (8.2)$$

Dividing by $A(^{238}\text{U})$:

$$\frac{A(^{234}\text{U})}{A(^{238}\text{U})} = 1 + [\gamma_0 - 1]e^{-\lambda_{234}t} \quad (8.3)$$

Which can be solved for t until about 1 Ma.

8.2 The ^{230}Th method

U and Th are strongly incompatible elements. This causes chemical fractionation and disturbs the secular equilibrium of the ^{238}U decay series in young volcanic rocks. It is commonly found that the activity ratio $A(^{230}\text{Th})/A(^{238}\text{U}) > 1$. As expected, the secular equilibrium between ^{234}U and ^{238}U is not disturbed by chemical fractionation, so that $A(^{234}\text{U})/A(^{238}\text{U}) = 1$. The total ^{230}Th activity is given by:

$$A(^{230}\text{Th}) = A(^{230}\text{Th})_0^x e^{-\lambda_{230}t} + A(^{238}\text{U})(1 - e^{-\lambda_{230}t}) \quad (8.4)$$

where $A(^{230}\text{Th})_0^x$ is the initial amount of ‘excess’ ^{230}Th at the time of crystallisation and $A(^{238}\text{U}) = A(^{234}\text{U})$ due to secular equilibrium of the U isotopes. Thus, the first term of Equation 8.4 increases with time from 0 to $A(^{238}\text{U})$ while the second term decreases from $A(^{230}\text{Th})_0^x$ to 0. Dividing by $A(^{232}\text{Th})$ yields a linear relationship between $A(^{230}\text{Th})/A(^{232}\text{Th})$ and $A(^{238}\text{U})/A(^{232}\text{Th})$:

$$\frac{A(^{230}\text{Th})}{A(^{232}\text{Th})} = \frac{A(^{230}\text{Th})_0^x}{A(^{232}\text{Th})} e^{-\lambda_{230}t} + \frac{A(^{238}\text{U})}{A(^{232}\text{Th})} (1 - e^{-\lambda_{230}t}) \quad (8.5)$$

This forms an isochron with slope $(1 - e^{-\lambda_{230}t})$, from which the age t can be calculated. This method is applicable to volcanic rocks and pelitic ocean sediments ranging from 3ka to 1Ma.

8.3 The ^{230}Th -U method

Uranium is significantly more soluble in water than Th. As a result, the intermediate daughter ^{230}Th is largely absent from sea water. Thus, lacustrine and marine carbonate rocks contain some U but virtually no Th at the time of formation. The ^{230}Th activity increases steadily with time as a result of ^{234}U decay. The total ^{230}Th activity consists of a growing component $A(^{230}\text{Th})^s$ that is in secular equilibrium with ^{238}U and a shrinking component $A(^{230}\text{Th})^x$ of ‘excess’ ^{230}Th produced by the surplus of ^{234}U commonly found in ocean water (see section 8.1):

$$A(^{230}\text{Th}) = A(^{230}\text{Th})^s + A(^{230}\text{Th})^x \quad (8.6)$$

$$\text{with: } A(^{230}\text{Th})^s = A(^{238}\text{U})(1 - e^{-\lambda_{230}t}) \quad (8.7)$$

$$\text{and: } A(^{230}\text{Th})^x = \frac{\lambda_{230}}{\lambda_{230} - \lambda_{234}} A(^{234}\text{U})_0^x (e^{-\lambda_{234}t} - e^{-\lambda_{230}t}) \quad (8.8)$$

In which the expression for $A(^{230}\text{Th})^x$ follows from Equation 2.14 and $A(^{234}\text{U})_0^x$ denotes the initial amount of excess ^{234}U activity (as in Section 8.1). Taking into account that $A(^{234}\text{U})_0^x = A(^{234}\text{U})_0 - A(^{238}\text{U})$, and dividing by $A(^{238}\text{U})$, we obtain:

$$\frac{A(^{230}\text{Th})^x}{A(^{238}\text{U})} = \frac{\lambda_{230}}{\lambda_{230} - \lambda_{234}} (\gamma_0 - 1) (e^{-\lambda_{234}t} - e^{-\lambda_{230}t}) \quad (8.9)$$

in which $\gamma_o \equiv A(^{234}\text{U})/A(^{238}\text{U})$ as defined in Section 8.1. The formation age of the carbonate can be calculated by substituting Equations 8.7 and 8.9 into 8.6 and solving for t .

$$\frac{A(^{230}\text{Th})}{A(^{238}\text{U})} = 1 - e^{-\lambda_{230}t} + \frac{\lambda_{230}}{\lambda_{230} - \lambda_{234}}(\gamma_o - 1) \left(e^{-\lambda_{234}t} - e^{-\lambda_{230}t} \right) \quad (8.10)$$

If $\gamma_o = 1$ (i.e., the water is in secular equilibrium for U), then Equation 8.6 simplifies to:

$$\frac{A(^{230}\text{Th})}{A(^{238}\text{U})} = 1 - e^{-\lambda_{230}t} \quad (8.11)$$

If $\gamma_o \neq 0$, Equation 8.11 yields ages that are systematically too old, unless $t < 100\text{ka}$ and $\gamma_o \leq 1.15$.

Chapter 9

Error propagation

All the methods and equations presented thus far have assumed that all parameters are either known or measured with infinite precision. In reality, however, the analytical equipment used to measure isotopic compositions, elemental concentrations and radioactive half-lives is not perfect. It is crucially important that we quantify the resulting analytical uncertainty before we can reliably interpret the resulting ages.

For example, suppose that the extinction of the dinosaurs has been dated at 65 Ma in one field location, and a meteorite impact has been dated at 64 Ma elsewhere. These two numbers are effectively meaningless in the absence of an estimate of precision. Taken at face value, the dates imply that the meteorite impact took place 1 million years after the mass extinction, which rules out a causal relationship between the two events. If, however, the analytical uncertainty is significantly greater than 1 Myr (e.g. 64 ± 2 Ma and 65 ± 2 Ma), then such of a causal relationship remains very plausible.

9.1 Some basic definitions

Suppose that our geochronological age (t) is calculated as a function (f) of some measurements (x and y):

$$t = f(x, y) \quad (9.1)$$

Suppose that we have performed a large number (n) of replicate measurements of x and y :

$$\begin{cases} x = \{x_1, x_2, \dots, x_i, \dots, x_n\} \\ y = \{y_1, y_2, \dots, y_i, \dots, y_n\} \end{cases} \quad (9.2)$$

It is useful to define the following *summary statistics*:

1. The mean:

$$\begin{cases} \bar{x} \equiv \frac{1}{n} \sum_{i=1}^n x_i \\ \bar{y} \equiv \frac{1}{n} \sum_{i=1}^n y_i \end{cases} \quad (9.3)$$

is a useful definition for the ‘most representative’ value of x and y , which can be plugged into Equation 9.1 to calculate the ‘most representative’ age.

2. The variance:

$$\begin{cases} s[x]^2 \equiv \frac{1}{n-1} \sum_{i=1}^n (x_i - \bar{x})^2 \\ s[y]^2 \equiv \frac{1}{n-1} \sum_{i=1}^n (y_i - \bar{y})^2 \end{cases} \quad (9.4)$$

with $s[x]$ and $s[y]$ the ‘standard deviations’, is used to quantify the amount of dispersion around the mean.

3. The covariance:

$$s[x, y] \equiv \frac{1}{n-1} \sum_{i=1}^n (x_i - \bar{x})(y_i - \bar{y}) \quad (9.5)$$

quantifies the degree of correlation between variables x and y .

\bar{x} , \bar{y} , $s[x]^2$, $s[y]^2$ and $s[x, y]$ can all be estimated from the input data (x, y) . These values can then be used to infer $s[t]^2$, the variance of the calculated age t , a process that is known as ‘error propagation’. To this end, recall the definition of the variance (Equation 9.4):

$$s[t]^2 \equiv \frac{1}{n-1} \sum_{i=1}^n (t_i - \bar{t})^2 \quad (9.6)$$

We can estimate $(t_i - \bar{t})$ by differentiating Equation 9.1:

$$t_i - \bar{t} = (x_i - \bar{x}) \frac{\partial f}{\partial x} + (y_i - \bar{y}) \frac{\partial f}{\partial y} \quad (9.7)$$

Plugging Equation 9.7 into 9.6, we obtain:

$$s[t]^2 = \frac{1}{n-1} \sum_{i=1}^n \left[(x_i - \bar{x}) \left(\frac{\partial f}{\partial x} \right) + (y_i - \bar{y}) \left(\frac{\partial f}{\partial y} \right) \right]^2 \quad (9.8)$$

$$= s[x]^2 \left(\frac{\partial f}{\partial x} \right)^2 + s[y]^2 \left(\frac{\partial f}{\partial y} \right)^2 + 2 s[x, y] \frac{\partial f}{\partial x} \frac{\partial f}{\partial y} \quad (9.9)$$

This is the general equation for the propagation of uncertainty with two variables, which is most easily extended to more than two variables by reformulating Equation 9.9 into a matrix form:

$$s[t]^2 = \begin{bmatrix} \frac{\partial t}{\partial x} & \frac{\partial t}{\partial y} \end{bmatrix} \begin{bmatrix} s[x]^2 & s[x, y] \\ s[x, y] & s[y]^2 \end{bmatrix} \begin{bmatrix} \frac{\partial t}{\partial x} \\ \frac{\partial t}{\partial y} \end{bmatrix} \quad (9.10)$$

where the innermost matrix is known as the *variance-covariance* matrix and the outermost matrix (and its transpose) as the *Jacobian matrix*. Let us now apply this equation to some simple functions.

9.2 Examples

Let x and y indicate measured quantities associated with analytical uncertainty. And let a and b be some error free parameters.

1. addition:

$$\begin{aligned} t &= ax + by \Rightarrow \frac{\partial t}{\partial x} = a, \frac{\partial t}{\partial y} = b \\ \Rightarrow s[t]^2 &= a^2 s[x]^2 + b^2 s[y]^2 + 2ab s[x, y] \end{aligned} \quad (9.11)$$

2. subtraction:

$$t = ax - by \Rightarrow s[t]^2 = a^2 s[x]^2 + b^2 s[y]^2 - 2ab s[x, y] \quad (9.12)$$

3. multiplication:

$$\begin{aligned}
 t = axy &\Rightarrow \frac{\partial t}{\partial x} = ay, \frac{\partial t}{\partial y} = ax \\
 &\Rightarrow s[t]^2 = (ay)^2 s[x]^2 + (ax)^2 s[y]^2 + 2a^2 xy s[x, y] \\
 &\Rightarrow \left(\frac{s[t]}{t}\right)^2 = \left(\frac{s[x]}{x}\right)^2 + \left(\frac{s[y]}{y}\right)^2 + 2\frac{s[x, y]}{xy}
 \end{aligned} \tag{9.13}$$

4. division:

$$t = a \frac{x}{y} \Rightarrow \left(\frac{s[t]}{t}\right)^2 = \left(\frac{s[x]}{x}\right)^2 + \left(\frac{s[y]}{y}\right)^2 - 2\frac{s[x, y]}{xy} \tag{9.14}$$

5. exponentiation:

$$t = a e^{bx} \Rightarrow \frac{\partial f}{\partial x} = ab e^{bx} \Rightarrow s[t]^2 = (bt)^2 s[x]^2 \tag{9.15}$$

6. logarithms:

$$t = a \ln(bx) \Rightarrow \frac{\partial f}{\partial x} = \frac{a}{x} \Rightarrow s[t]^2 = a^2 \left(\frac{s[x]}{x}\right)^2 \tag{9.16}$$

7. power:

$$t = ax^b \Rightarrow \frac{\partial f}{\partial x} = b \frac{ax^b}{x} \Rightarrow \left(\frac{s[t]}{t}\right)^2 = b^2 \left(\frac{s[x]}{x}\right)^2 \tag{9.17}$$

9.3 Accuracy vs. precision

Recall the definition of the arithmetic mean (Equation 9.3):

$$\bar{x} \equiv \frac{1}{n} \sum_{i=1}^n x_i$$

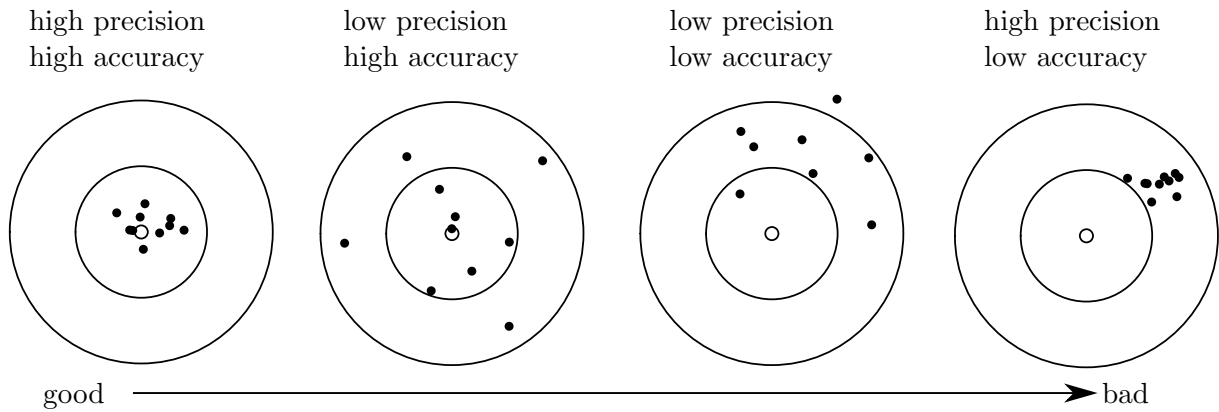
Applying the equation for the error propagation of a sum (Equation 9.11):

$$s[\bar{x}]^2 = \frac{1}{n} \sum_{i=1}^n s[x_i]^2 = \frac{s[x]^2}{n} \tag{9.18}$$

where we assume that all n measurements were done *independently*, so that $\text{cov}(x_i, x_j) = 0 \forall i, j$. The standard deviation of the mean is known as the standard error:

$$s[\bar{x}] = \frac{s[x]}{\sqrt{n}} \tag{9.19}$$

This means that the standard error of the mean monotonically decreases with the square root of sample size. In other words, we can arbitrarily increase the *precision* of our analytical data by acquiring more data. However, it is important to note that the same is generally not the case for the *accuracy* of those data. The difference between precision and accuracy is best explained by a darts board analogy:



Whereas the analytical precision can be computed from the data using the error propagation formulas introduced above, the only way to get a grip on the accuracy is by analysing another sample of independently determined age. Such test samples are also known as ‘secondary standards’.

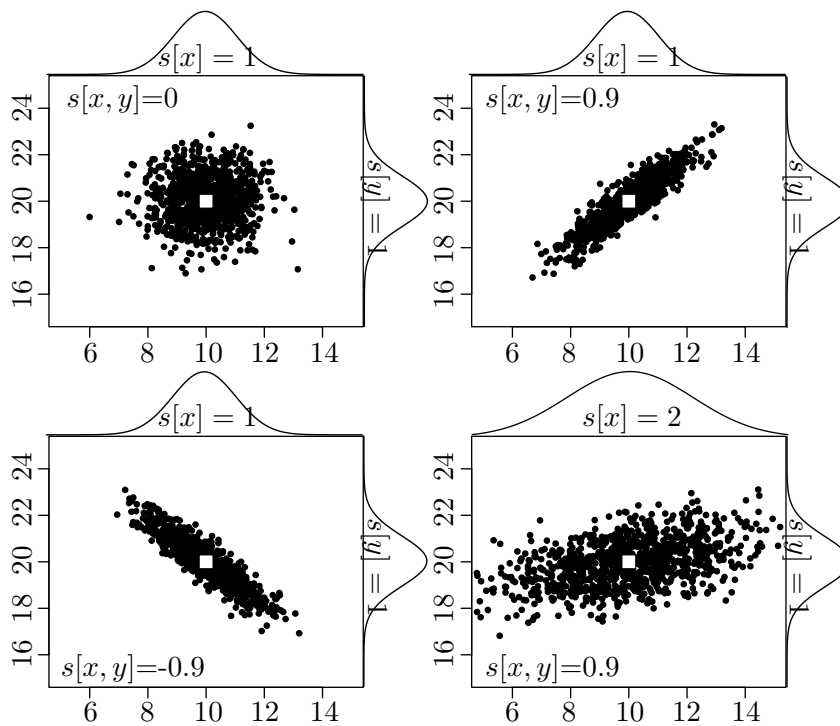


Figure 9.1: Four datasets of 100 random numbers (black dots) which have the same means (white squares) but different (co-)variance structures. The marginal distributions of the x and y variables are shown as ‘bell curves’ on the top and right axis of each plot.

Chapter 10

Exercises

1. If helium ions (mass number = 4) are accelerated with a voltage of 10 kV in a mass spectrometer, at what speed are they emitted from the source? Recall that 1 atomic mass unit (amu) = 1.66×10^{-27} kg and the elementary charge is 1.602×10^{-19} C. [s/ux 969 :xwstuv]
2. We are trying to estimate the Rb concentration in a rock for the purpose of whole rock Rb-Sr dating. To this end, we use a spike with a Rb concentration of 7.5 ppm containing 99.4% ^{87}Rb and 0.6% ^{85}Rb (these are atomic abundances). We mix 3.5g of the spike with 0.25g of sample dissolved in 50g. The $^{87}\text{Rb}/^{85}\text{Rb}$ -ratio of the mixture is 1.55, as measured by mass spectrometry. What is the Rb concentration in ppm? Note that natural Rb comprises of 27.825% ^{87}Rb and 72.165% ^{85}Rb . [udd 071 :xwstuv]
3. A biotite contains 465ppm Rb and 30ppm Sr with a $^{87}\text{Sr}/^{86}\text{Sr}$ -ratio of 2.50. Given an initial $^{87}\text{Sr}/^{86}\text{Sr}$ -ratio of 0.7035, what is the age of the biotite? Natural Rb has an atomic mass of 85.4678 and comprises 72.165% ^{85}Rb and 27.825% ^{87}Rb , which has a half life of $t_{1/2} = 48.8$ Gyr. Sr has an atomic mass of 87.62. Its non-radiogenic isotopes occur with the following abundances: $^{84}\text{Sr}/^{86}\text{Sr} = 0.056584$ and $^{86}\text{Sr}/^{88}\text{Sr} = 0.1194$. [eG 987 :xwstuv]
4. Consider a zircon with the following composition: U = 792.1 ppm, Th = 318.6 ppm, Pb = 208.2 ppm. Atomic masses for U, Th and Pb in the zircon are 238.04, 232.04 and 205.94, respectively. The isotopic composition of the Pb is as follows: $^{204}\text{Pb} = 0.048\%$, $^{206}\text{Pb} = 80.33\%$, $^{207}\text{Pb} = 9.00\%$, $^{208}\text{Pb} = 10.63\%$. Assume the following initial Pb composition: 204 : 206 : 207 : 208 = 1.00 : 16.25 : 15.51 : 35.73. The decay constants for ^{238}U , ^{235}U and ^{232}Th are given in Section 5. $^{238}\text{U}/^{235}\text{U} = 137.818$. Calculate the $^{206}\text{Pb}/^{238}\text{U}$, $^{207}\text{Pb}/^{235}\text{U}$, $^{208}\text{Pb}/^{232}\text{Th}$ and $^{207}\text{Pb}/^{206}\text{Pb}$ -age of the zircon. Give an account of its formation history. [eG 6891 pua 1.284 and 1.523, 9041 :xwstuv]
5. A biotite was separated from granite and dated with the K-Ar method. The analytical data are as follows: $\text{K}_2\text{O} = 8.45$ weight %, radiogenic $^{40}\text{Ar} = 6.015 \times 10^{-10}$ mol/g. What is the K-Ar age of the biotite? The atomic mass of K is 39.098 (and oxygen 15.9994), with an isotopic composition that comprises 93.258% ^{39}K , 6.730% ^{41}K and 0.01167% ^{40}K , which has a half-life of $t_{1/2} = 1.248$ Gyr. Recall that only 10.72% of the ^{40}K decays to ^{40}Ar , with the remaining 89.28% turning into ^{40}Ca . [eN 227 :xwstuv]
6. Consider a biotite with a conventional K-Ar age of 384Ma. A $^{40}\text{Ar}/^{39}\text{Ar}$ step-heating experiment yields the following data:

% ^{39}Ar released	7	15	20	25	35	70	100
$^{40}\text{Ar}^*/^{39}\text{Ar}$	2.27	4.97	6.68	9.58	10.25	10.10	10.26

The analysis was done using a co-irradiated 1.062 Ga biotite age standard yielding a $^{40}\text{Ar}^*/^{39}\text{Ar}$ -ratio of 27.64. Construct the $^{40}\text{Ar}/^{39}\text{Ar}$ age spectrum and use this to comment on the thermal history of the host rock. $t_{1/2}(^{40}\text{Ar}) = 1.248 \text{ Gyr}$.

[Answer: 115, 243, 319, 442, 470, 463 and 470 Ma]

7. How many cm^3 of helium does a rock weighing 1 kg and containing 2 ppm of uranium produce after 1 billion years? The molar volume of an ideal gas is 22.414 litres. Uranium has an atomic mass of 238.04 with $^{238}\text{U}/^{235}\text{U} = 137.818$. Decay constants of U are given in Section 5. [Answer: 27.0 cm^3]
8. Repeated analysis of the Fish Canyon zircon age standard ($t=27.8 \text{ Ma}$) yields the following fission track data:

ρ_s ($\times 10^5 \text{cm}^{-2}$)	ρ_i ($\times 10^6 \text{cm}^{-2}$)	ρ_d ($\times 10^5 \text{cm}^{-2}$)
36.56	6.282	2.829
38.97	7.413	3.313
56.53	7.878	2.457
41.05	8.578	3.485
45.87	6.985	2.482

Compute the average ζ -calibration factor and use this to calculate the zircon fission track ages of the following rocks:

	ρ_s ($\times 10^5 \text{cm}^{-2}$)	ρ_i ($\times 10^6 \text{cm}^{-2}$)	ρ_d ($\times 10^5 \text{cm}^{-2}$)
Tardree rhyolite	60.49	2.66	1.519
Bishop tuff	6.248	1.299	0.081

The half-life of ^{238}U is $t_{1/2} = 4.47 \text{ Gyr}$.

[Answer: Tardree – 57 Ma; Bishop – 643 ka]

9. A fossil mollusc has been found in a Quaternary beach formation and its activity ratio measured as $A(^{230}\text{Th}) / A(^{238}\text{U}) = 0.6782$. Determine the age of the fossil assuming that $\gamma_o = 1.15$ and given that the half lives of ^{230}Th and ^{234}U are 75,380 and 245,500 years, respectively. [Answer: 100 kyr]

Chapter 11

Programming practicals

In this Chapter you will process some real geochronological datasets using R. R is a free and open programming language that works on any operating system, including Windows, OS-X and Unix/Linux. It can be downloaded and installed from <http://r-project.org>. Section 11.1 presents a brief R tutorial, which covers most commands that you will need for the subsequent computer practicals.

11.1 Introduction to R

A number of different graphical user interfaces (GUIs) are available to interact with R. The most popular of these are Rgui, RStudio, RCommander and Tinn-R.

1. Starting these applications or running R in a text terminal presents the user with a command line prompt. Anything that is typed after the `>` symbol will be evaluated immediately. Thus, we can use R as a calculator:

```
> 1 + 1
> sqrt(2)
> exp(log(10))
> 31 %% 14
```

2. Alternatively, code can also be saved as text (using a built-in text editor) and saved as `mycode.R`, say. This code can then be copied and pasted at the command line prompt. Or it can be called from the command line using the `source()` function:

```
> source('mycode.R')
```

3. In the remainder of this tutorial, we will assume that your code is run from a text file unless explicitly stated otherwise. The `#` symbol marks the beginning of a comment. R ignores anything that follows it:

```
1 # The arrow symbol is used to assign a value to a
2 # variable. Note that the arrow can point both ways:
3 foo <- 2
4 4 -> bar
5 print(foo*bar)
```

```

6
7 # Defining a vector of multiple values:
8 myvec <- c(0,1,2,3,4,5)
9 # or, equivalently:
10 myvec <- seq(0,5)
11 # or
12 myvec <- seq(from=0,to=5,by=1)
13 # or
14 myvec <- 0:5
15
16 # Turn myvec into a 2x3 matrix:
17 mymat <- matrix(myvec,nrow=2)
18
19 # Accessing one or more items from a vector or matrix:
20 x <- myvec[3]
21 y <- myvec[1:3]
22 z <- mymat[1,2:3]
23
24 # Change the 2nd value in mymat's 3rd column to 10:
25 mymat[2,3] <- 10
26
27 # Change the entire second column of mymat to -1:
28 mymat[,2] <- -1
29
30 # Transpose of a matrix:
31 flipped <- t(mymat)
32
33 # Element-wise multiplication (*)
34 # vs. matrix multiplication (%*%):
35 rectangle <- mymat * mymat
36 square <- mymat %*% flipped

```

4. Lists are used to store more complex data objects:

```
1 mylist <- list(v=myvec,m=mymat,nine=9)
```

The three components of `mylist` can be accessed in a number of equivalent ways. For example, the first item (`v`) of `mylist` can be accessed either as `mylist$v`, as `mylist[[1]]` or as `mylist[['v']]`.

Data frames are list-like tables:

```

1 myframe <- data.frame(period=c('Cz','Mz','Pz','PC'),
2                       SrSr=c(0.708,0.707,0.709,0.708),
3                       fossils=c(TRUE,TRUE,TRUE,FALSE))

```

You can access the items in the data frame `myframe` either like a list (e.g. `myframe$period`) or like a matrix (`myframe[, 'period']`):

5. If you want to learn more about a function, type `help()` or `?` at the command line prompt:

```
> help(c)
> ?matrix
```

6. In addition to R's built-in functions, you can also define your own:

```
1 cube <- function(n){
2   return(n^3)
3 }
4
5 # Using this function to take the cube of 3:
6 c3 <- cube(3)
7
8 # Conditional statement:
9 toss <- function(){
10   if (runif(1)>0.5){ # runif(n) draws n random
11     print("head")   # numbers between 0 and 1
12   } else {
13     print("tail")
14   }
15 }
16
17 # Use a for loop to toss 10 virtual coins:
18 for (i in 1:10) {
19   toss()
20 }
```

7. The purpose of the practical exercises in Sections 11.2-11.5 is to process datasets contained in external data files. For this you will need to be able to navigate through your file system and load the necessary files:

```
> ls()           # list all the variables
> rm(list=ls())  # clear the current workspace
> getwd()        # get the current working directory
> setwd("path_to_a_valid_directory")
```

8. Use the above commands to navigate to the directory containing the file named `RbSr.csv`. Then read this file into memory:

```
1 RbSr <- read.csv("RbSr.csv",header=TRUE)
```

Type `names(RbSr)` or `colnames(RbSr)` at the command prompt to list the variable names (column headers) contained in this dataset.

9. Let us now perform an isochron regression (Section 4.2) through these Rb-Sr data:

```

2 # Plot Sr87Sr86 against Rb87Sr86:
3 plot(RbSr[, 'Rb87Sr86'], RbSr[, 'Sr87Sr86'], type="p")
4
5 # fit a linear model to the data
6 fit <- lm(Sr87Sr86 ~ Rb87Sr86, data = RbSr)

```

10. `fit` is a ‘list’ object. Type `str(fit)` at the command prompt to see its structure. One of its items is `fit$coefficients`, which contains the slope and the intercept of the linear fit. Alternatively, we can also access these values using the `coef()` function. The following code uses this function to calculate the isochron age:

```

7 # define the 87Rb decay constant (in Ma-1):
8 lam87 <- 1.3972e-5 # according to Villa et al. (2015)
9 # compute the age from the slope:
10 tRbSr <- log(1 + coef(fit)[2])/lam87
11
12 # add the best fit line to the existing plot:
13 abline(fit)
14 # label with the isochron age:
15 title(tRbSr)

```

11. One of the most powerful features of R is the availability of thousands of ‘packages’ providing additional functionality to the built-in functions. For example, let us download and install the `IsoplotR` package from the ‘Comprehensive R Archive Network’ (CRAN):

```
> install.packages('IsoplotR')
```

12. We can use `IsoplotR` to redo the isochron regression exercise using a more rigorous weighted regression algorithm that takes into account the analytical uncertainties in both the $^{87}\text{Sr}/^{86}\text{Sr}$ - and $^{87}\text{Rb}/^{86}\text{Sr}$ -ratios:

```

1 # load the functionality of the IsoplotR package:
2 library('IsoplotR')
3
4 # load the data (see ?read.data for details):
5 RbSr2 <- read.data('RbSr.csv', method='Rb-Sr', format=1)
6
7 # compute and plot the isochron diagram:
8 isochron(RbSr2)

```

Even though `IsoplotR` is powerful, convenient, and popular, we will not use it in the remainder of these notes. Instead, we will carry out all our calculations in base R because this will give you a more fundamental understanding of geochronology.

11.2 U-Th-Pb data reduction

You are supplied with two data files that were produced by the quadrupole laser ablation ICP-MS system at UCL's London Geochronology Centre. At the time of the analysis, this instrument could not resolve ^{204}Pb from the isobaric interference at ^{204}Hg . Therefore, it is not possible to apply a common lead correction as explained in Section 5. However, this does not cause any major issues to us because:

1. The mineral analysed is zircon, which incorporates very little common Pb in its crystal structure during crystallisation.
2. The ages are sufficiently old for the radiogenic Pb to dominate the common Pb component by orders of magnitude.

In this exercise, we will use standard-sample bracketing (Section 3.3) to process some raw mass spectrometer data in R :

1. Load the input files `91500.csv` (sample) and `GJ1.csv` (standard) into memory.
2. Plot the ^{238}U signal against time. The resulting curve consists of three segments: (i) the first 20 seconds record the background ('blank') signal of the ICP-MS, measured while the laser was switched off; (ii) 20 seconds into the run, the laser is turned on and the ions arrive in the ICP-MS; (iii) After the signal has ramped up quickly, it slowly drops over time as the laser goes out of focus whilst drilling deeper into the sample. This is the 'signal'.
3. Compute the arithmetic mean U and Pb blank (measurements before 20 seconds), and subtract them from the signal (measurements after 25 seconds). Do this for both the sample and the standard. You will get two times four vectors, for ^{206}Pb , ^{207}Pb , ^{235}U and ^{238}U .
4. Use the four blank corrected signal vectors to form two pairs of $^{206}\text{Pb}/^{238}\text{U}$ and $^{207}\text{Pb}/^{235}\text{U}$ vectors.
5. Take the arithmetic mean of the $^{206}\text{Pb}/^{238}\text{U}$ and $^{207}\text{Pb}/^{235}\text{U}$ ratio vectors. You will now have two pairs of numbers representing the *measured* $^{206}\text{Pb}/^{238}\text{U}$ and $^{207}\text{Pb}/^{235}\text{U}$ ratios for the sample and the standard.
6. Given that GJ-1 has a known age of 600.4 Ma, what are its *expected* $^{206}\text{Pb}/^{238}\text{U}$, and $^{207}\text{Pb}/^{235}\text{U}$ ratios? Is there a significant difference between the measured and the expected ratios? What could be causing this?
7. Calculate a correction factor by dividing the expected GJ-1 ratios by the measured values.
8. Apply the correction factor calculated in step 7 to the measured ratios for sample 91500. This gives us two estimated atomic $^{206}\text{Pb}/^{238}\text{U}$ and $^{207}\text{Pb}/^{235}\text{U}$ ratios.
9. What is the age of 91500?
10. Can you plot the results on a Wetherill concordia diagram?

11.3 $^{40}\text{Ar}/^{39}\text{Ar}$ data reduction

In this exercise, we will reduce some synthetic $^{40}\text{Ar}/^{39}\text{Ar}$ data. You are provided with three input files:

1. `smp1.csv`: ^{36}Ar , ^{39}Ar and ^{40}Ar as a function of time (t) for the sample.
2. `stnd.csv`: the same data for the standard, which is a Fish Canyon sanidine with a conventional K-Ar age of 27.8 Ma.
3. `blnk.csv`: a ‘blank’ run, i.e. a measurement of the background levels of Argon present in the mass spectrometer in the absence of a sample.

To perform the data reduction, please follow the following steps:

1. Load the three input files.
2. Plot the ^{40}Ar signal of the sample against time. Do the same for the ^{36}Ar signal in the blank. What is the difference?
3. Perform a linear regression of the ^{36}Ar , ^{39}Ar and ^{40}Ar signals through time and determine the intercept at $t=0$.
4. Subtract the ‘time zero’ intercepts of the blank from those of the sample and standard.
5. Apply an atmospheric correction assuming that all ^{36}Ar has an atmospheric origin.
6. Calculate the J-value of the standard.
7. Calculate the age of the sample.

11.4 Error propagation

This exercise will build on the results from the previous two practicals.

1. Plot the $^{206}\text{Pb}/^{238}\text{U}$ -ratios of the sample against those of the standard (data from Section 11.2). Verify that the covariance between the two can safely be neglected.
2. Calculate the standard errors of the mean $^{206}\text{Pb}/^{238}\text{U}$ signal ratios for the sample (91500) and the standard (GJ-1) using the `mean` and `sd` functions.
3. Propagate the standard errors of the atomic $^{206}\text{Pb}/^{238}\text{U}$ and $^{207}\text{Pb}/^{235}\text{U}$ -ratios calculated in step 8 of Section 11.2.
4. Propagate the analytical uncertainties of the U-Pb age, ignoring the covariance terms. Recall that

$$t = \frac{1}{\lambda_{238}} \ln \left(1 + \frac{^{206}\text{Pb}}{^{238}\text{U}} \right)$$

If you want you can use the simplifying approximation that $\ln(1 + X) \approx X$ if $X \ll 1$ (this assumption may not be correct for the $^{207}\text{Pb}/^{235}\text{U}$ -age).

5. Compute the analytical uncertainties associated with the linear extrapolation of the argon signals of the sample and the standard in Section 11.3. In **R**, the covariance matrix of the slope and intercept can be simply obtained from the `vcov(fit)` function, where `fit` is the output of the `lm` function (see item 9 of Section 11.1). The corresponding standard errors are then found by taking the square root of the diagonal elements of this matrix.
6. Use these error estimates to propagate the analytical uncertainty of the J-value and the sample age. Again you can use the linear approximation to the age equation mentioned in point 4.

11.5 Fission tracks

In this exercise, you will use your programming skills to calculate some fission track ages. You are given the following datasets:

1. `DUR.csv`: a table with two columns listing the number of spontaneous tracks N_s and induced tracks N_i counted in 25 grains of an apatite age standard ($t = 31.4$ Ma) from Durango, Mexico. Note that these pairs of tracks were counted over the same area, so that $\rho_s/\rho_i = N_s/N_i$ in Equation 7.9.
2. `MD.csv`: a similar table for an apatite sample from Mount Dromedary, Australia.

You will need to:

1. Rewrite Equation 7.9 in terms of the ζ calibration factor and use this new formula to calculate the ζ factor for each single grain analysis of the Durango age standard. Use a dosimeter track density of $\rho_D = 300,000 \text{ cm}^{-2}$.
2. Use the mean of these ζ factors to calculate the age of the Mount Dromedary sample (i.e., the single grain ages and their mean).
3. Propagate the analytical uncertainties for each of those single grain ages, using the fact that fission track counts (N , say) follow a Poisson distribution for which it is true that:

$$\sigma_N^2 = N$$

To simplify the calculations, you can also use the following approximation:

$$\frac{1}{\lambda} \ln \left(1 + \frac{g_i}{g_s} \lambda \zeta \rho_d \frac{N_s}{N_i} \right) \approx \frac{g_i}{g_s} \zeta \rho_d \frac{N_s}{N_i}$$

4. How does the single grain age precision of the fission track method compare to the U-Pb and $^{40}\text{Ar}/^{39}\text{Ar}$ age uncertainties in Sections 11.2 and 11.3? Also compare with the standard deviation and standard error of the mean age of Mount Dromedary apatite.

Part II

Advanced geochronology

Chapter 12

Introduction

Part 1 of these notes gave a very basic introduction to geochronology. At this basic level, it is possible to write one's own data processing software from scratch, as we have done in the R practicals. Unfortunately this is not so easy at a more advanced level. Research-grade geochronological data processing chains involve several layers of highly specialised software packages:

1. A first layer of software controls the mass spectrometer and extracts the raw time resolved isotopic signals from it. This software generally comes with the mass spectrometer, and was written and designed by engineers who may be completely unfamiliar with the geological applications of the equipment.
2. The output files from this low level software are passed on to a second layer of software, which processes the raw mass spectrometer, combines standard with standards, performs isotope dilution calculations, etc. This 'middleware' is sometimes written by geologists, and sometimes by companies. Examples are `Iolite`, `GLITTER`, `Squid`, `LADR` and `ET_Redux` for U–Pb geochronology; `ArArCalc` and `Pychron` for Ar–Ar geochronology, etc.
3. The output files produced by the second layer of data processing software require further processing for more advanced statistical analysis and visualisation. `IsoplotR` is a software package that fulfils this role.

Chapter 23 provides a brief introduction to the design philosophy and operating principles of `IsoplotR`, which will be explored further in later chapters. Chapter 13 introduces the important subject of error correlations, and shows how these are captured by `IsoplotR`'s different input formats. We will see that error correlations plays a fundamental role in all of `IsoplotR`'s methods. Chapter ?? reviews the subject of linear regression, which underpins the construction of isochrons. `IsoplotR` currently implements three different types of error weighted linear regression algorithms that account for error correlations between variables and between aliquots in two or three dimensions. Chapter ?? explains how these three methods represent different approaches of dealing with overdispersion. Chapter ?? introduces a weighted mean plot to visualise multiple age estimates and proposes a heuristic method to detect outliers. Chapter ?? presents three approaches to construct confidence intervals for isochron ages, weighted means and so forth. It introduces a profile log-likelihood method for the calculation of asymmetric confidence intervals.

Chapter ?? discusses three further methods to visualise multi-aliquot collections of ages. Cumulative age distributions (CADs) and kernel density estimates (KDEs) show the frequency distribution of the age measurements but do not explicitly take into account the analytical

uncertainties. The radial plot is introduced as a more appropriate data visualisation tool for ‘heteroscedastic’ data (i.e. data with unequal measurements uncertainties). The radial plot provides a good vehicle to assess the dispersion of multi-aliquot datasets. Overdispersed datasets require further processing with continuous or discrete mixture models that are discussed in Chapter ??.

With these basic statistical building blocks in place, the remainder of the notes cover issues that are specific to individual geochronometers and their geological applications. They will be discussed in the same order as they are listed in **IsoplotR**’s graphical user interface.

Chapter ?? provides an in-depth discussion of **IsoplotR**’s U–Pb functionality. This includes an overview of the various input formats, concordia ages, discordia regression, common-Pb correction methods and initial disequilibrium corrections.

The U–Th–He and fission track methods are two relatively new chronometers that were never implemented in Ludwig (2003)’s **Isoplot** program. Despite their short history, the statistical treatment of the U–Th–He method and especially the fission track method are well developed and in some ways more advanced than that of more established geochronometers. For example, both the radial plot of Section 14.3 and the mixture models of Section 14.4 were originally developed for fission track data (Galbraith, 1990; Galbraith and Green, 1990), but are generalised to all chronometric methods by **IsoplotR**. And in this chapter we will see that the U–Th–He method was the first to be cast in a logratio context (Vermeesch, 2010), which is slowly being adopted by other chronometers and promises to become even more important in the future.

Chapter ?? covers U–Th dating and Chapter ?? thermochronology, including both the traditional external detector method and the new LA-ICP-MS based approach.

Chapter ?? covers the subject of detrital geochronology, which includes a discussion of maximum depositional age estimation and multidimensional scaling analysis.

Finally, Section ?? sets out a roadmap for future developments to improve the accuracy and precision of geochronological data, and to provide closer integration of **IsoplotR** with earlier steps of the data processing chain.

Chapter 13

Statistical considerations

13.1 The normal distribution

Geochronological data processing is generally concerned with isotopic ratio measurements, which are acquired by mass spectrometers and are affected by random detector noise. Unless explicitly specified otherwise, we will assume that this noise follows a Gaussian distribution. In one dimension, this distribution is described by the following probability density function (pdf):

$$\mathcal{N}(x|\mu, \sigma^2) = \frac{1}{\sigma\sqrt{2\pi}} \exp\left[-\frac{(x - \mu)^2}{2\sigma^2}\right] \quad (13.1)$$

where μ is the **mean** and σ is the **standard deviation**.

1. the **mean** μ controls the **location** of the distribution.
2. the **standard deviation** σ quantifies the **dispersion** of the distribution.

The interval from $\mu - \sigma$ to $\mu + \sigma$ covers 68.27% of the area under the PDF, and the interval from $\mu - 2\sigma$ to $\mu + 2\sigma$ covers 95.45%. Conversely 95% of the area under the normal PDF is contained within an interval of $\mu \pm 1.96\sigma$.

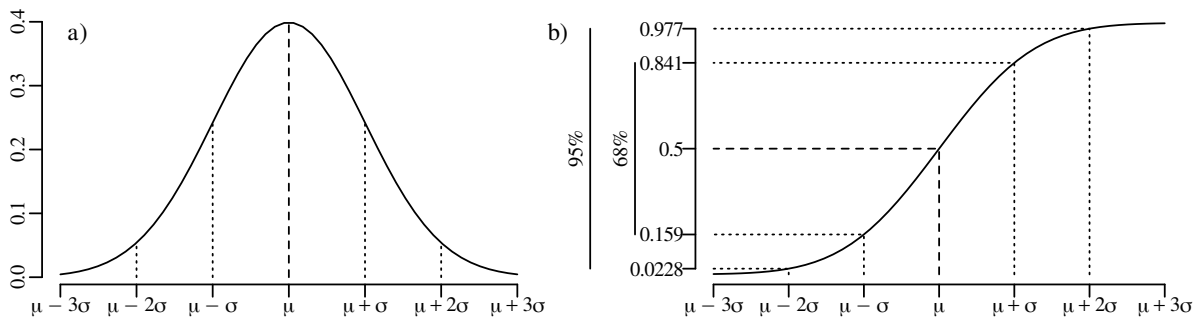


Figure 13.1: a) pdf and b) cumulative distribution function (cdf, i.e., the integral of the pdf) of the normal distribution. The $\mu \pm \sigma$ and $\mu \pm 2\sigma$ intervals cover $\sim 68\%$ and $\sim 95\%$ of the distribution, respectively.

It can be mathematically proven that the *sum* of n randomly selected values converges to a Gaussian distribution, provided that n is large enough. This convergence is guaranteed *regardless of the distribution of the original data*. This mathematical law is called the **Central Limit Theorem**. Physically processes such as thermal diffusion are characterised by white noise and

Brownian walks which are, in effect, additive processes. So it makes sense that these give rise to Gaussian distributions. In fact, these additive processes are so common that the Gaussian distribution is also known as the normal distribution, implying that all other distributions are ‘abnormal’.

The normal distribution can be generalised to two dimensions using a pdf that comprises five parameters: the means μ_x and μ_y , the standard deviations σ_x and σ_y , and the covariance $\sigma_{x,y}$:

$$\mathcal{N}(x, y | \mu_x, \mu_y, \sigma_x^2, \sigma_y^2, \sigma_{x,y}) = \frac{\exp\left(-\frac{1}{2} \begin{bmatrix} x - \mu_x & y - \mu_y \end{bmatrix} \begin{bmatrix} \sigma_x^2 & \sigma_{x,y} \\ \sigma_{x,y} & \sigma_y^2 \end{bmatrix}^{-1} \begin{bmatrix} x - \mu_x \\ y - \mu_y \end{bmatrix}\right)}{2\pi \sqrt{\begin{vmatrix} \sigma_x^2 & \sigma_{x,y} \\ \sigma_{x,y} & \sigma_y^2 \end{vmatrix}}} \quad (13.2)$$

where we recognise the **covariance matrix** as

$$\Sigma_{x,y} = \begin{bmatrix} \sigma_x^2 & \sigma_{x,y} \\ \sigma_{x,y} & \sigma_y^2 \end{bmatrix}$$

Finally, we can define the **correlation coefficient** as:

$$\rho[x, y] \equiv \frac{s[x, y]}{\sqrt{s[x]s[y]}} \approx \frac{\sigma[x, y]}{\sqrt{\sigma[x]\sigma[y]}} \equiv \rho \quad (13.3)$$

$\rho[x, y]$ is akin to a normalised covariance, whose values range from -1 (perfect negative correlation) to $+1$ (perfect positive correlation).

13.2 The method of maximum likelihood

The parameters μ and σ of the normal distribution are *unknown* but can be *estimated* from the data. This can be done using the **method of maximum likelihood**. Given n data points $\{x_1, x_2, \dots, x_n\}$ drawn from a normal distribution, we can formulate the normal likelihood function as

$$\mathcal{L}(\mu, \sigma^2 | x_1, x_2, \dots, x_n) = \prod_{i=1}^n \mathcal{N}(x_i | \mu, \sigma^2) \quad (13.4)$$

μ and σ can be estimated by maximising the likelihood or, equivalently, the log-likelihood:

$$\begin{aligned} \mathcal{LL}(\mu, \sigma^2 | x_1, x_2, \dots, x_n) &= \sum_{i=1}^n \ln [\mathcal{N}(x_i | \mu, \sigma^2)] \\ &= \sum_{i=1}^n -\ln[\sigma] - \frac{1}{2} \ln[2\pi] - \frac{(x_i - \mu)^2}{2\sigma^2} \end{aligned} \quad (13.5)$$

Taking the derivative of \mathcal{LL} with respect to μ and setting it to zero:

$$\begin{aligned} \frac{\partial \mathcal{LL}}{\partial \mu} &= -\sum_{i=1}^n \frac{x_i - \mu}{\sigma^2} = 0 \\ \Rightarrow n\mu - \sum_{i=1}^n x_i &= 0 \\ \Rightarrow \bar{x} &= \frac{1}{n} \sum_{i=1}^n x_i \end{aligned} \quad (13.6)$$

which is the same as Equation 9.3. Using the same strategy to estimate σ :

$$\begin{aligned}\frac{\partial \mathcal{LL}}{\partial \sigma} &= \sum_{i=1}^n -\frac{1}{\sigma} + \frac{(x_i - \mu)^2}{\sigma^3} = 0 \\ \Rightarrow \sum_{i=1}^n \frac{(x_i - \mu)^2}{\sigma^3} &= \frac{n}{\sigma} \\ \Rightarrow \hat{\sigma} &= \sqrt{\frac{1}{n} \sum_{i=1}^n (x_i - \mu)^2}\end{aligned}\tag{13.7}$$

which is nearly identical to the formula for the standard deviation that we saw in Section 9.1:

$$s[x] = \sqrt{\frac{1}{n-1} \sum_{i=1}^n (x_i - \bar{x})^2}\tag{13.8}$$

There are just two differences between Equations 13.8 and Equation 13.7:

1. Equation 13.7 uses the population mean μ , whereas Equation 13.8 uses the sample mean \bar{x} .
2. Equation 13.7 divides the sum of the squared differences between the measurements and the mean by n , whereas Equation 13.8 divides it by $(n-1)$.

The two differences are related to each other. The subtraction of 1 from n is called the **Bessel correction** and accounts for the fact that by using an estimate of the mean (\bar{x}), rather than the true value of the mean (μ), we introduce an additional source of uncertainty in the estimate of the standard deviation. This additional uncertainty is accounted for by subtracting one **degree of freedom** from the model fit.

Again using the method of maximum likelihood, it is possible to estimate the covariance for bivariate normal distributions as (proof omitted):

$$\hat{\sigma}_{x,y} = \sum_{i=1}^n \frac{1}{n} (x_i - \mu_x)(y_i - \mu_y)\tag{13.9}$$

or, if μ_x and μ_y are unknown and must be estimated from the data as well:

$$s[x,y] = \sum_{i=1}^n \frac{1}{n-1} (x_i - \bar{x})(y_i - \bar{y})\tag{13.10}$$

Thus we can estimate the **covariance matrix** (Equation 9.10) of the bivariate normal distribution as:

$$\Sigma_{x,y} = \begin{bmatrix} s[x]^2 & s[x,y] \\ s[x,y] & s[y]^2 \end{bmatrix}\tag{13.11}$$

Finally, we can define the **correlation coefficient** as:

$$r \equiv \frac{s[x,y]}{\sqrt{s[x]s[y]}} \approx \frac{\sigma[x,y]}{\sqrt{\sigma[x]\sigma[y]}} \equiv \rho\tag{13.12}$$

Besides providing a powerful tool to estimate parameters from data, the method of maximum likelihood can also be used to estimate the standard errors of those parameters. Let \hat{z} be the

maximum likelihood estimate of some parameter z . We can approximate the log-likelihood with a second order Taylor series in the vicinity of \hat{z} :

$$\mathcal{LL}(z) \approx \mathcal{LL}(\hat{z}) + \frac{\partial \mathcal{LL}}{\partial z}(z - \hat{z}) + \frac{1}{2} \frac{\partial^2 \mathcal{LL}}{\partial z^2}(z - \hat{z})^2$$

By definition, $\partial \mathcal{LL} / \partial z = 0$ at \hat{z} . Therefore, the likelihood ($\mathcal{L}(z) = \exp[\mathcal{LL}(z)]$) is proportional to:

$$\mathcal{L}(z) \propto \exp \left[\frac{1}{2} \frac{\partial^2 \mathcal{LL}}{\partial z^2}(z - \hat{z})^2 \right]$$

which can also be written as:

$$\mathcal{L}(z) \propto \exp \left[-\frac{1}{2} \frac{(z - \hat{z})^2}{-\frac{1}{\frac{\partial^2 \mathcal{LL}}{\partial z^2}}}} \right]$$

This equation fits the functional form of the normal distribution (Equation 13.1):

$$\mathcal{L}(z) \propto \exp \left[-\frac{1}{2} \frac{(z - \hat{z})^2}{\sigma[z]^2} \right]$$

which leads to

$$\sigma[z]^2 = \frac{1}{-\frac{\partial^2 \mathcal{LL}}{\partial z^2}} \quad (13.13)$$

$-\frac{\partial^2 \mathcal{LL}}{\partial z^2}$ is known as the **Fisher Information**. Equation 13.13 can be generalised to multiple dimensions:

$$\Sigma = -\mathcal{H}^{-1} \quad (13.14)$$

where Σ is the covariance matrix and $(\mathcal{H})^{-1}$ is the inverse of the ('Hessian') matrix of second derivatives of the log-likelihood function with respect to the parameters.

13.3 The mean square of weighted deviates (MSWD)

Let $t = \{t_1, \dots, t_n\}$ be a set of n age estimates determined on different aliquots of the same sample with a true age $\mu[t]$, and let $\sigma[t] = \sigma[t_1] = \dots = \sigma[t_n]$ be their normally distributed analytical uncertainty. Then we can estimate $\mu[t]$ and $\sigma[t]$ with Equations 13.6 and 13.8, respectively. However, if each of the n age estimates has its own analytical uncertainty ($\sigma[t_1] \neq \dots \neq \sigma[t_n]$), then it is important to account for this *heteroscedasticity*. Consider, for example, the following dataset of four samples:

i	1	2	3	4
t_i	1005	1000	995	1125
$s[t_i]$	10	10	10	100

Table 13.1: Heteroscedastic dataset of four age estimates (in Ma).

Then the arithmetic mean is 1031 Ma, which plots outside the 95% confidence intervals of all three of the four aliquots. The **error weighted mean** addresses this issue:

$$\bar{t}_w = \frac{\sum_{i=1}^n (t_i / s[t_i]^2)}{\sum_{i=1}^n (1 / s[t_i]^2)} \quad (13.15)$$

Applying Equation 13.15 to the example dataset attaches a smaller weight to the imprecise fourth measurement, yielding a \bar{t}_w value of 1000.4 Ma:

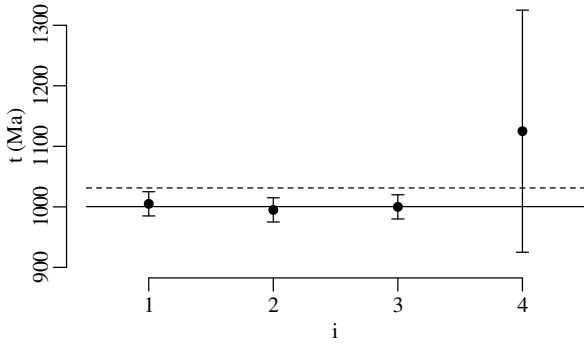


Figure 13.2: The data of Table 13.1 with 95% confidence intervals shown as error bars, the weighted mean as a dashed horizontal line and the error weighted mean as a solid line.

The extent to which the observed scatter in the data around the weighted mean can be explained by the analytical uncertainties can be assessed using a chi-square test. To this end, we define the chi-square statistic as:

$$\chi_{stat}^2 = \sum_{i=1}^n \frac{(t_i - \bar{t}_w)^2}{s[t_i]^2} \quad (13.16)$$

For the data of Table 13.1:

$$\chi_{stat}^2 = \frac{(1005 - 1000.4)^2}{10^2} + \frac{(1000 - 1000.4)^2}{10^2} + \frac{(995 - 1000.4)^2}{10^2} = 6.17$$

We can compare this value with a chi-square distribution with $df = n - 1$ degrees of freedom. In the case of the example dataset, $n = 4$ and $df = 3$. The **p-value** is defined as the probability of observing a value greater than χ_{stat}^2 under this distribution:

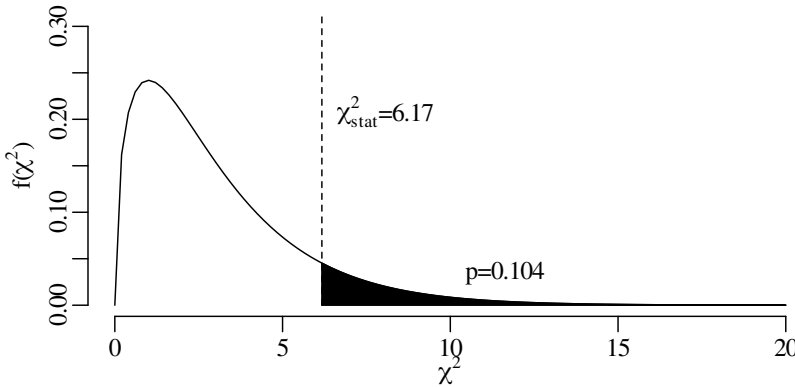


Figure 13.3: Chi-square distribution with 3 degrees of freedom. The p-value for an outcome of $\chi_{stat}^2 = 6.17$ is the integral of the black area.

A cutoff of $\alpha = 0.05$ is often used to assess whether the observed scatter of the data around the weighted mean can be accounted for by the analytical uncertainty alone. For the example dataset, the p-value is 0.10, which is greater than this **significance level**. Therefore, we have no reason to suspect that there are any other sources of dispersion in the data besides analytical uncertainty.

An alternative way to assess the data scatter is by dividing the chi-square statistic χ_{stat}^2 by the number of degrees of freedom df . The resulting numerical value is called the ‘Mean Square of the Weighted Deviates’ (MSWD, McIntyre et al., 1966) by geochronologists, but is known as the ‘reduced chi-square statistic’ elsewhere.

$$MSWD = \frac{\chi_{stat}^2}{n - 1} \quad (13.17)$$

For sufficiently large samples and, hence, degrees of freedom, the distribution of the MSWD statistic converges to a normal distribution with a mean of 1. However for small samples there

is a comparatively greater probability of obtaining an MSWD value that is greater or smaller than 1:

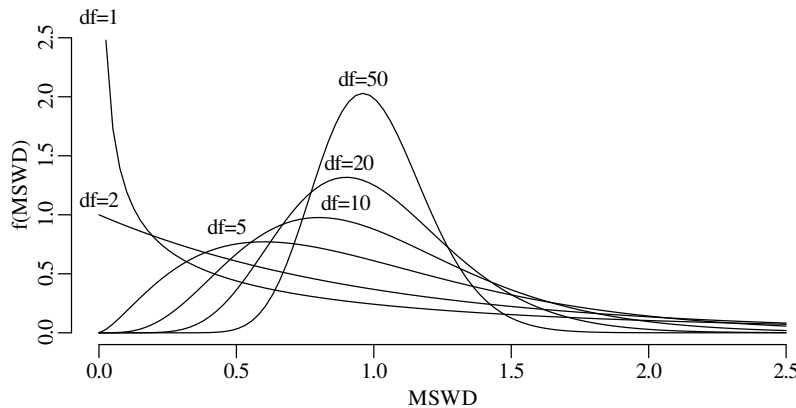


Figure 13.4: Expected distribution of the MSWD for different degrees of freedom. With increasing sample size, the distribution of the MSWD converges to a normal distribution with mean 1.

The MSWD is a very useful device to assess the degree to which the observed scatter of the data around the best fit can be explained by the analytical uncertainties. Three scenarios are possible:

1. If the analytical uncertainties alone explain the total scatter around the true mean, then the MSWD is expected to take on a value of ≈ 1 .
2. Data sets that exhibit MSWD values close to zero are said to be “underdispersed” with respect to the analytical uncertainties. This indicates some problem with the error propagation, which is often due to undetected systematic effects.
3. Finally, MSWD values > 1 can often be attributed to some form of geological dispersion. This overdispersion carries geological significance.

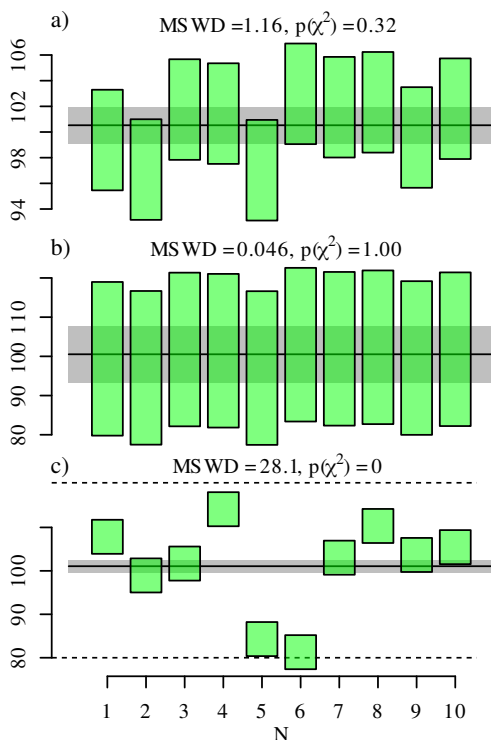


Figure 13.5: Three different synthetic data sets shown as weighted mean plots. The analytical uncertainties are shown as 95% error bars. Each of the data sets consists of 10 aliquots that are affected by a combination of analytical and geological dispersion. The relative importance of these two sources of scatter can be assessed using the mean square of weighted deviates (MSWD) and the p-value of the chi-square test. The case where $\text{MSWD} \approx 1$ is the easiest to interpret: it means that the scatter of the data around the best fit line can be completely explained by the analytical uncertainty. The case where $\text{MSWD} < 1$ may seem like a good outcome but it is in fact a bad one because it indicates that there may be a problem with the error propagation. A high p-value or low MSWD may happen once but red flags should go up if all samples in a study show this type of behaviour. Finally the case where $\text{MSWD} > 1$ is not good or bad but ‘interesting’. The dashed lines mark the overdispersion ($\omega = 10 + 7/-4$ Ma) as discussed in Section 13.4.

13.4 Dealing with overdispersion

IsoplotR offers three strategies (‘models’) to deal with overdispersed datasets:

1. Model-1: inflate the analytical uncertainties until MSWD=1

A ‘model-1’ average assumes that the overdispersion of the data is due to an underestimation of the analytical uncertainties by a common factor f . To ‘fix’ the overdispersion, the model-1 fit simply multiplies the uncertainties with this number and plugs the resulting value into Equation 13.17:

$$\sum_{i=1}^n \frac{(t_i - \bar{t}_w)^2}{(n-1)(f s[t_i])^2} = 1 \Rightarrow f = \sqrt{MSWD}$$

Thus, we can account for any overdispersion by replacing Equation 13.31 with:

$$\mu \in \left\{ \bar{x} \pm t_{df, \alpha/2} s[\bar{x}] \sqrt{MSWD} \right\} \quad (13.18)$$

2. Model-2: ignore the analytical uncertainties

Although the \sqrt{MSWD} trick is attractive from a mathematical point of view, the physical meaning of the overdispersion factor is not always clear. It effectively means that the reported analytical uncertainties are not reliable. But if this is the case, then one might wonder why the degree of unreliability should be the same (i.e. a factor of \sqrt{MSWD}) for all aliquots. An alternative way to deal with unreliable uncertainty estimates is to ignore them altogether and use the ordinary arithmetic mean as a fallback solution.

3. Model-3: quantify the overdispersion

The most sophisticated, and arguable most realistic method to deal with overdispersed dataset is to attribute them to geological effects. A ‘model-3’ weighted mean assumes that the data were drawn from a normal distribution with two sources of variance:

$$\mathcal{N}(x|\mu, \sigma^2 + \omega^2) = \frac{1}{\sqrt{2\pi(\sigma^2 + \omega^2)}} \exp \left[-\frac{(x - \mu)^2}{2(\sigma^2 + \omega^2)} \right] \quad (13.19)$$

where ω is the **overdispersion**. μ and ω can be estimated by maximising the following log-likelihood function:

$$\mathcal{LL}_w \propto \sum_{i=1}^n -\frac{1}{2} \ln(s[t_i]^2 + \omega^2) + \left[-\frac{(x - \mu)^2}{2(s[t_i]^2 + \omega^2)} \right] \quad (13.20)$$

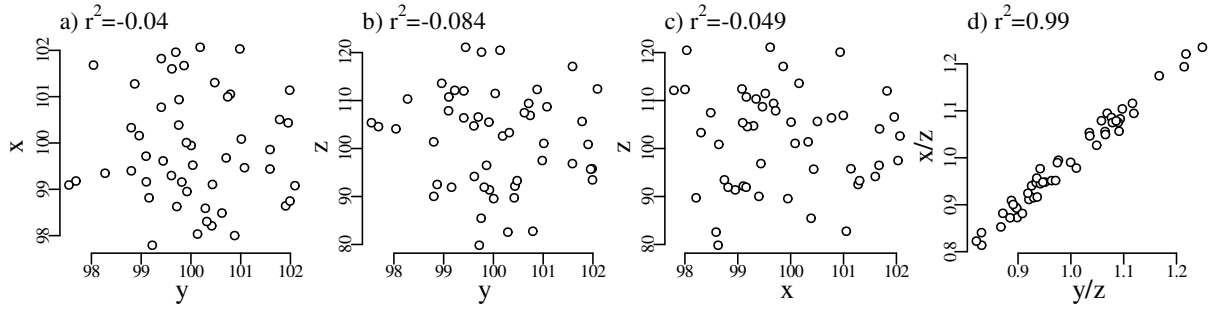
In mathematical terms, model-3 is known as a **random effects model**. The overdispersion ω has physical meaning and may be as useful as the mean age itself. Consider, for example, a batholith whose emplacement age is determined by TIMS U–Pb geochronology of igneous zircon. The analytical precision of TIMS measurements is on the order of a few ‰. So if the batholith was intruded at 20 Ma, then the zircon ages can be determined to within 20ka. Large intrusions often take much longer than 20kyr to crystallise. Therefore it is unlikely that all the zircons have exactly the same age. The resulting geological dispersion will cause high MSWD values. The ω parameter of a model-3 weighted mean would quantify this dispersion and thereby estimate the residence time of zircon in the magma chamber.

13.5 Error correlations

Consider the generic age equation for a radioactive parent P that decays to a radiogenic daughter D in the presence of an inherited component that can be traced by normalising to a non-radiogenic isotope d of the daughter element:

$$t = \frac{1}{\lambda} \ln \left(\frac{[D/d] - [D/d]_0}{[P/d]} + 1 \right) \quad (13.21)$$

For example, P , D and d might be ^{87}Rb , ^{87}Sr and ^{86}Sr for Rb–Sr geochronology, or ^{238}U , ^{206}Pb and ^{204}Pb for U–Pb geochronology. Chapter 9 showed that error propagation of the age t requires the characterisation of the full covariance structure of the isotopic ratio data including their mean values, their standard errors and their covariances or error correlations. This covariance structure is estimated from the raw mass spectrometer data using the low level data processing software mentioned in Chapter 12. The error propagation of isotopic ratio data could be greatly simplified if the covariances were negligible. Unfortunately this is generally not the case. To prove this point, consider the following set of synthetic mass spectrometer data:



where x , y and z are uncorrelated (normally distributed) random numbers, but the ratios y/z and x/z are strongly correlated. The *spurious correlation* between ratios like this was first described by Pearson (1896). It is strongest when the common nuclide z is measured less precisely than the remaining two nuclides x and y . If the summary statistics of x , y and z are known, then it is possible to predict the correlation coefficient:

$$r \left[\frac{y}{z}, \frac{x}{z} \right] \approx \frac{(s[z]/z)^2}{\sqrt{(s[x]/x)^2 + (s[z]/z)^2} \sqrt{(s[y]/y)^2 + (s[z]/z)^2}} \quad (13.22)$$

For example, consider the following hypothetical Re–Os abundance estimates:

$$y = ^{187}\text{Os} = 2,000 \pm 10 \text{ fmol}; \quad x = ^{187}\text{Re} = 30,000 \pm 100 \text{ fmol} \text{ and } z = ^{188}\text{Os} = 200 \pm 2 \text{ fmol}$$

then the $(^{187}\text{Os}/^{188}\text{Os})$ and $(^{187}\text{Re}/^{188}\text{Os})$ isotope ratio estimates exhibit a correlation coefficient of

$$r \left[\frac{^{187}\text{Os}}{^{188}\text{Os}}, \frac{^{187}\text{Re}}{^{188}\text{Os}} \right] = \frac{\left(\frac{2}{200}\right)^2}{\sqrt{\left(\frac{100}{30,000}\right)^2 + \left(\frac{2}{200}\right)^2} \sqrt{\left(\frac{10}{2,000}\right)^2 + \left(\frac{2}{200}\right)^2}} = 0.85$$

The strong error correlation between the two variables on the Re–Os isochron diagram are manifested as narrow and steeply inclined error ellipses. The same phenomenon manifests itself in all isotopic ratio data to a lesser or greater degree:

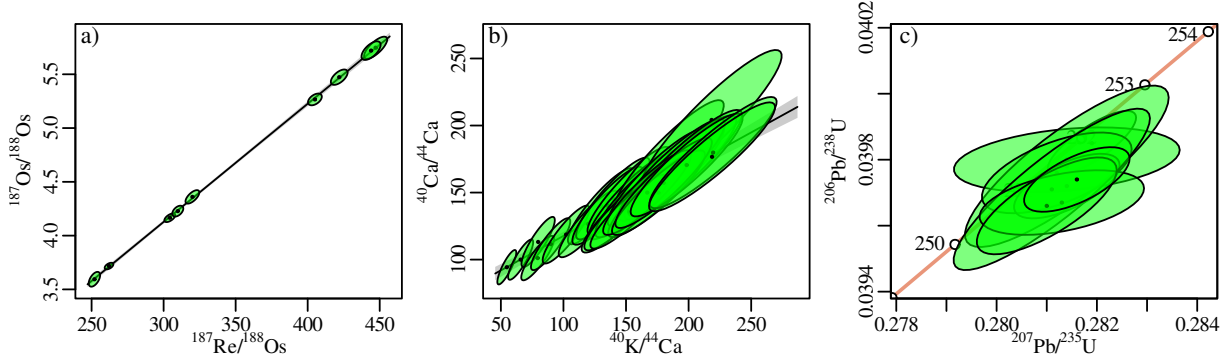


Figure 13.6: Examples of correlated uncertainties shown as confidence ellipses in a) Re–Os and b) K–Ca isochron and c) Wetherill U–Pb concordia space.

For some geochronometers, the error correlations can be reduced by recasting the isotopes into two new ratios z/y vs. x/y . If y is measured more precisely than x and z , then this reduces the spurious correlation coefficient. For example, revisiting the earlier Re–Os example:

$$r \left[\frac{^{188}\text{Os}}{^{187}\text{Os}}, \frac{^{187}\text{Re}}{^{187}\text{Os}} \right] = \frac{\left(\frac{10}{2000}\right)^2}{\sqrt{\left(\frac{100}{30,000}\right)^2 + \left(\frac{10}{2000}\right)^2} \sqrt{\left(\frac{2}{200}\right)^2 + \left(\frac{10}{2000}\right)^2}} = 0.37$$

The same change of variables can be applied to other geochronometers as well:

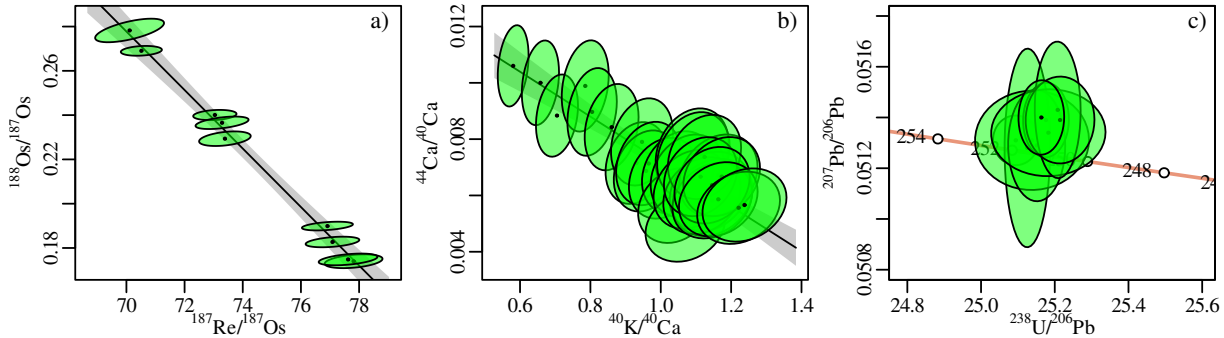


Figure 13.7: Recasting the data of Figure 13.6 into an inverse ratio form reduces the error correlations for the Re–Os, K–Ca and U–Pb data.

Given a data table of conventional ratios ($X = x/z$ and $Y = y/z$), it is possible to calculate the inverse ratios ($X' = x/y$ and $Y' = z/y$), their uncertainties ($s[X']$ and $s[Y']$) and error correlations ($r[X', Y']$) using the following equations:

$$\begin{cases} X' = \frac{X}{Y} \\ Y' = \frac{1}{Y} \\ \left(\frac{s[X']}{X'}\right)^2 = \left(\frac{s[X]}{X}\right)^2 - 2r[X, Y] \left(\frac{s[X]}{X}\right) \left(\frac{s[Y]}{Y}\right) + \left(\frac{s[Y]}{Y}\right)^2 \\ \left(\frac{s[Y']}{Y'}\right)^2 = \left(\frac{s[Y]}{Y}\right)^2 \\ r[X'Y'] = \left(\frac{X'}{s[X']}\right) \left[\left(\frac{Y}{s[Y]}\right) - r[X, Y] \left(\frac{X}{s[X]}\right) \right] \end{cases} \quad (13.23)$$

This transformation is perfectly symmetric in the sense that it can also be used to convert inverse isochron ratios to conventional ones. To do this, it suffices to swap X' and Y' for X and Y and vice versa. `IsoplotR` carries out these conversions on the fly. So if a data file provides

the isotopic composition as conventional ratios, then it is possible to plot the data as inverse ratios without worrying about the details of the conversion.

13.6 Linear regression

As briefly discussed in Chapter 4, isochrons are an important instrument of high precision, high accuracy geochronology. Given several aliquots from a single sample, they allow the non-radiogenic component of the daughter nuclide to be quantified and separated from the radiogenic component. A conventional isochron is obtained by fitting a straight line through the conventional isochron ratios introduced in Section 13.5. The slope and intercept then yield the radiogenic daughter-parent ratio and the non-radiogenic daughter composition, respectively (Nicolaysen, 1961). In its simplest form, isochrons are fitted by ordinary least squares regression.

Consider a set of n bivariate data points $x = \{x_1, x_2, \dots, x_n\}$ and $y = \{y_1, y_2, \dots, y_n\}$. The best fit straight line through these data can be found by minimising the sum of the squared residuals:

$$S = \sum_{i=1}^n (y_i - a - bx_i)^2 \quad (13.24)$$

where a is the intercept and b the slope. However this method does not take into account the analytical uncertainties of the isotopic ratio measurements. In a first step, let us consider the situation where only the dependent variable (y) is affected by significant analytical uncertainty, and let $s[y] = \{s[y_1], s[y_2], \dots, s[y_n]\}$ be the corresponding standard errors. Then the least squares criterion can be modified to create a weighted regression algorithm:

$$S_w = \sum_{i=1}^n \left(\frac{y_i - a - bx_i}{s[y_i]} \right)^2 \quad (13.25)$$

Alternatively (and equivalently), the best fit line can also be obtained by maximising the log-likelihood:

$$\mathcal{LL} = - \sum_{i=1}^n \ln(2\pi s[y_i]) - \frac{S_w}{2} \quad (13.26)$$

To illustrate the usefulness of the weighted regression algorithm, consider a simple three-point example. Let $\mathbf{x} = \{10, 20, 40\}$ and $\mathbf{y} = \{20, 30, 50\}$ be the *true* x - and y -coordinates of the three points¹. It is easy to see that these fall on a perfect line with intercept $\mathbf{a} = 10$ and slope $\mathbf{b} = 1$. Let $s[\mathbf{y}] = \{1, 1, 10\}$ be the analytical uncertainties of \mathbf{y} , so that the third point is ten times less precise than the first two. Further let $y = \{20, 30, 60\}$ be a random realisation of \mathbf{y} . Then the best ordinary least squares fit through $x = \mathbf{x}$ and y has an intercept of $a = 5.0$ and a slope of $b = 1.36$. This poor result is strongly influenced by the third, least precise data point. Subjecting the same dataset to weighted linear regression yields $a = 9.4$ and $b = 1.04$. This is a far more accurate result (Figure 13.8.a).

In isochron regression, it is typical for not only y but also x to be affected by analytical uncertainty. In this case, the best fit line can be found by modifying the likelihood function (Titterton and Halliday, 1979; York, 1969; York et al., 2004):

$$\mathcal{LL}_y = -\frac{1}{2} \sum_{i=1}^n \ln(2\pi |\Sigma_i|) - \frac{1}{2} \sum_{i=1}^n \left[X_i - \hat{X}_i \right]^T \Sigma_i^{-1} \left[X_i - \hat{X}_i \right] \quad (13.27)$$

¹In the remainder of this paper, bold face will be used to mark the true values, whereas normal face will be used to mark the actual measurements (i.e. the true value plus some random analytical uncertainty).

where

$$X_i = \begin{bmatrix} x_i \\ y_i \end{bmatrix}, \hat{X}_i = \begin{bmatrix} \hat{x}_i \\ a + b\hat{x}_i \end{bmatrix} \text{ and } \Sigma_i = \begin{bmatrix} s[x_i]^2 & s[x_i, y_i] \\ s[x_i, y_i] & s[y_i]^2 \end{bmatrix} \quad (13.28)$$

where \hat{x}_i are the *estimated* values of \mathbf{x}_i for any value of a or b . $s[x_i, y_i]$ is the covariance of the i^{th} measurement's x- and y-uncertainties. To illustrate the importance of these covariance terms, consider a second three-point example:

i	\mathbf{x}	$s[\mathbf{x}]$	\mathbf{y}	$s[\mathbf{y}]$	$s[\mathbf{x}_i, \mathbf{y}_i]$
1	10	1	20	1	0.9
2	20	1	30	1	0.9
3	30	1	40	1	-0.9

which again defines a straight line with intercept $a = 10$ and slope $b = 1$. Let $x = \{10, 20, 28\}$ and $y = \{20, 30, 42\}$ be a random realisation of \mathbf{x} and \mathbf{y} . Suppose that we ignored or did not know the covariance terms. In that case the ordinary and weighted regression algorithms would yield the same outcome because all the samples have the same standard errors ($s[x_i] = s[y_i] = 1$ for all i). The resulting intercept and slope would then be $a = 7.2$ and $b = 1.21$. However, if we do take into account the covariances, then the maximum likelihood algorithm yields $a = 9.3$ and $b = 1.05$, which is much closer to the true values of $\mathbf{a} = 10$ and $\mathbf{b} = 1$ (Figure 13.8.b).

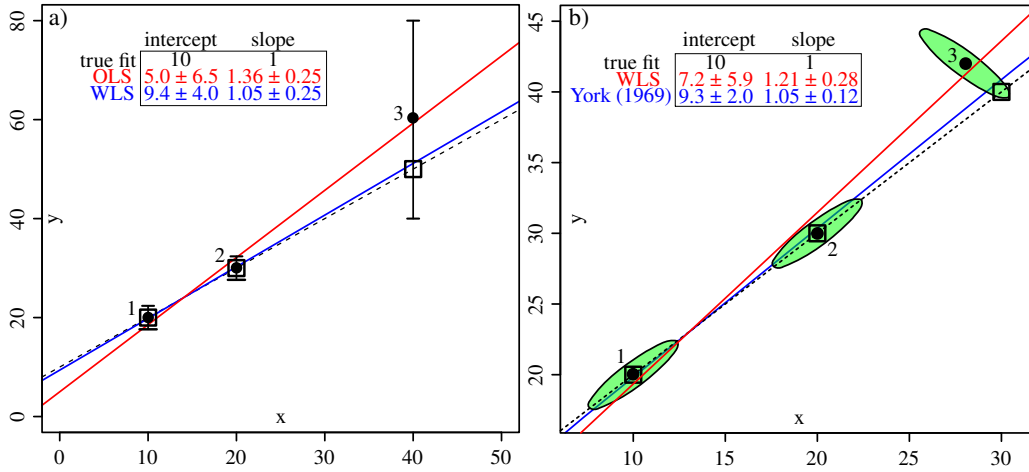


Figure 13.8: Illustration of the benefits of error-weighted linear regression. The black squares mark the true (x,y)-coordinates of three samples drawn from a (dashed) line with intercept $\mathbf{a} = 10$ and slope $\mathbf{b} = 1$. The black dots mark random realisations of these samples, given Gaussian uncertainties with uncertainties shown as 95% confidence bars or ellipses. a) three samples with analytical uncertainty in the y-variable only. The ordinary least squares fit ignoring these uncertainties is shown in red ($a = 5.0, b = 1.36$), the weighted least squares fit in blue ($a = 9.4, b = 1.04$). b) three samples with correlated uncertainties in both the x- and y-variable. Ignoring the error correlations yields the red fit ($a = 7.2, b = 1.21$). Accounting for the error correlations produces the blue fit ($a = 9.3, b = 1.05$).

The extent to which the observed scatter in the data around the best fit isochron line can be explained by the analytical uncertainties can be assessed using a chi-square test, in nearly exactly the same manner as described for the weighted mean in Section 13.3. In the case of linear regression, the chi-square statistic is defined as:

$$\chi_{stat}^2 = \sum_{i=1}^n \left[X_i - \hat{X}_i \right]^T \Sigma_i^{-1} \left[X_i - \hat{X}_i \right] \quad (13.29)$$

in which we recognise the second term of Equation 13.27, which is the matrix formulation of the sum of squares. We can compare this value with a chi-square distribution with $df = (k-1)n - k$ degrees of freedom, where k is the dimensionality of the linear fit. The MSWD is again defined as

$$MSWD = \chi_{stat}^2 / df$$

In complete analogy to the weighted mean of Section 13.3, the MSWD can be used to assess whether the scatter of the data falls within the range expected from the analytical uncertainties, or whether the data is over- or underdispersed. In the case of overdispersion, there are three ways ('models') to deal with this overdispersion:

1. model-1: inflate the analytical uncertainties by a factor \sqrt{MSWD} ;
2. model-2: ignore the uncertainties and fall back to ordinary least squares regression;
3. model-3: attribute the overdispersion to a second source of uncertainty in the intercept or slope of the line.

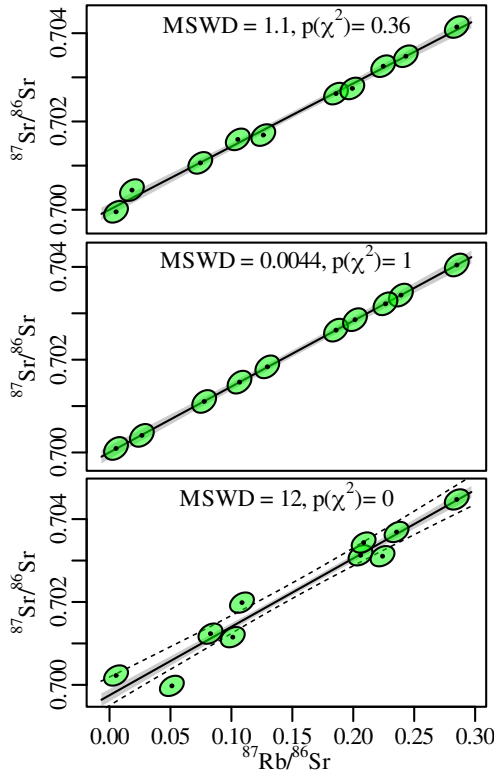


Figure 13.9: Three different synthetic Rb–Sr data sets shown as conventional isochron plots. The analytical uncertainties are shown as 95% error ellipses. The grey band represents a 95% confidence envelope for the best fit line using the York (1969) algorithm. Each of the data sets consists of 10 aliquots that are affected by a combination of analytical and geological dispersion. The relative importance of these two sources of scatter can be assessed using the mean square of weighted deviates (MSWD) and the p-value of the chi-square test. The case where $MSWD \approx 1$ is the easiest to interpret: it means that the scatter of the data around the best fit line can be completely explained by the analytical uncertainty. The case where $MSWD < 1$ may seem like a good outcome but it is in fact a bad one because it indicates that there may be a problem with the error propagation. A high p-value or low MSWD may happen once but red flags should go up if all samples in a study show this type of behaviour. Finally the case where $MSWD > 1$ is not good or bad but 'interesting'. The dashed line marks the 'overdispersion' estimated by a model-3 regression.

13.7 Confidence intervals

Figure 13.1 showed that approximately 95% of the normal distribution falls within two standard deviations of the mean. Thus, if we know that x was drawn from a normal distribution with standard deviation σ and an unknown mean μ , then 95% of all x -values are expected to fall in the interval

$$\mu - 2\sigma \leq x \leq \mu + 2\sigma$$

Subtracting x and μ from all terms:

$$-x - 2\sigma \leq -\mu \leq -x + 2\sigma$$

Multiplying with -1 :

$$x + 2\sigma \geq \mu \geq x - 2\sigma$$

which gives rise to the following 95% confidence interval for μ :

$$\mu \in \{x \pm 2\sigma\}$$

which gives rise to the popular ‘2-sigma’ confidence interval. Chapter 9 showed that the standard error of the mean is given by

$$s[\bar{x}] = s[x]/\sqrt{n}$$

One might be tempted to assume that $\bar{x} \pm 2s[\bar{x}]$ constitutes a 95% confidence interval for μ . However, this would be incorrect because \bar{x} does *not* follow a normal distribution. To construct a 95% confidence for μ based on \bar{x} , we first define the ‘t-statistic’ as follows:

$$\mathbf{t} = \frac{\bar{x} - \mu}{s[\bar{x}]} \quad (13.30)$$

where \mathbf{t} is written in bold to avoid confusion with the geological age t used elsewhere in these notes. \mathbf{t} follows a ‘t-distribution with $n-1$ degrees of freedom’. By definition, the 95% confidence interval is the collection of all those values of μ for which

$$t_{df,\alpha/2} \leq \mathbf{t} \leq t_{df,1-\alpha/2}$$

where $t_{df,\alpha/2}$ and $t_{df,1-\alpha/2}$ are the $\alpha/2$ and $(1-\alpha/2)$ quantiles of a t-distribution with df degrees of freedom, respectively. Hence:

$$t_{df,\alpha/2} \leq \frac{\bar{x} - \mu}{s[\bar{x}]} \leq t_{df,1-\alpha/2}$$

Rearranging:

$$\bar{x} - t_{df,\alpha/2}s[\bar{x}] \geq \mu \geq \bar{x} - t_{df,1-\alpha/2}s[\bar{x}]$$

Because the t-distribution is symmetric around zero, we can also write:

$$t_{df,1-\alpha/2} = -t_{df,\alpha/2}$$

Hence

$$\bar{x} + t_{df,\alpha/2}s[\bar{x}] \leq \mu \leq \bar{x} - t_{df,\alpha/2}s[\bar{x}]$$

or

$$\mu \in \{\bar{x} \pm t_{df,\alpha/2}s[\bar{x}]\} \quad (13.31)$$

For large samples (and, hence, degrees of freedom), the t-statistic is approximately equal to 2. But for small samples, it is greater than 2 and the 95% confidence interval for μ is wider as a consequence.

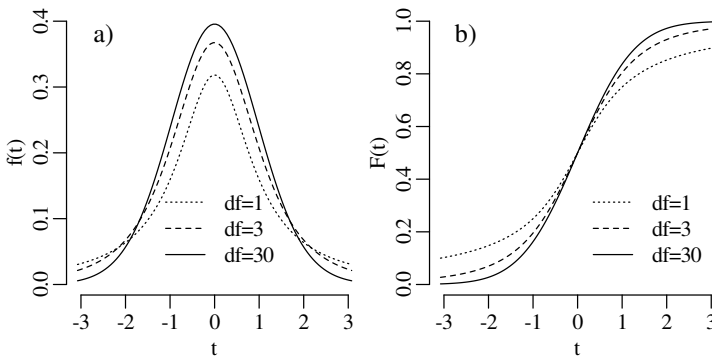


Figure 13.10: a) pdfs and b) cdfs of the t-distribution for three different degrees of freedom (df). For small sample sizes (low df), the t-distribution has long tails towards low and high values. With increasing sample size, the tails become shorter and the t-distribution sharper. When $df > 30$, the t-distribution is indistinguishable from a standard normal distribution with $\mu = 0$ and $\sigma = 1$.

IsoplotR reports the age uncertainties in the following form:

$$t = \hat{t} \pm x \mid y \mid z$$

where

\hat{t} is the age estimate

x is the standard error of \hat{t}

$y = t_{df,1-\alpha/2} \times x$ is the 95% confidence interval for \hat{t}

$z = \sqrt{MSWD} \times y$ is the 95% confidence interval for \hat{t} adjusted for overdispersion. This value is only reported for model-1 fits when the p-value of the chi-square test is less than 0.05.

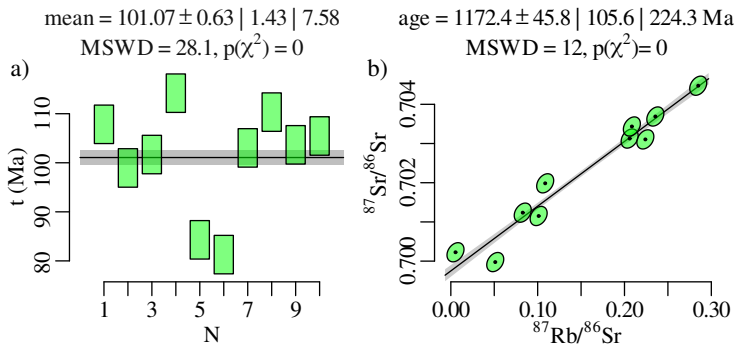


Figure 13.11: a) weighted mean (Figure 13.5c) and b) Rb–Sr isochron (Figure 13.9c) regression using a model-1 fit. The legend reports the best fit age and uncertainties reported as standard errors, and 95% confidence intervals with and without overdispersion.

With regards to error propagation, it is important to make a distinction between **random** and **systematic** sources of uncertainty. Random uncertainties can be reduced to arbitrarily low levels by averaging an arbitrarily large number of aliquots. In contrast, systematic uncertainties impose absolute limits on the precision of geochronological dates. For example, no absolute age determination can be more precise than the decay constants involved. Similarly, for dating methods such as $^{40}\text{Ar}/^{39}\text{Ar}$ or fission tracks, no sample date can be more precise than the J and ζ calibration factors, respectively.

When solving Equation 13.15, IsoplotR only incorporates the random sources of uncertainty into $s[t_i]$. If the user wishes to include the systematic uncertainties as well, then this is done by first computing the isotopic composition corresponding to the weighted mean age (and its uncertainty), and then re-propagating the analytical uncertainty of the weighted mean age, this time including the decay or calibration constant uncertainties.

Note that this procedure is unable to handle the systematic uncertainties associated with stable isotope ratios, molar masses etc. Those comparably small uncertainties demand a different approach in which not the ages but the isotopic data are averaged. Doing so would require the addition of new input formats that can trace error correlations between samples (Chapter ??). It would also require the development of a new generation of low-level data-processing software (Vermeesch, 2015; McLean, Bowring, and Gehrels, 2016).

References

McIntyre, G. A. et al. (1966). “The Statistical Assessment of Rb-Sr Isochrons”. In: *Journal of Geophysical Research* 71, pp. 5459–5468.

- McLean, N. M., J. F. Bowring, and G. Gehrels (2016). “Algorithms and software for U-Pb geochronology by LA-ICPMS”. In: *Geochemistry, Geophysics, Geosystems* 17.7, pp. 2480–2496.
- Nicolaysen, L. (1961). “Graphic interpretation of discordant age measurements on metamorphic rocks”. In: *Annals of the New York Academy of Sciences* 91.1, pp. 198–206.
- Pearson, K. (1896). “Mathematical contributions to the theory of evolution.—on a form of spurious correlation which may arise when indices are used in the measurement of organs”. In: *Proceedings of the Royal Society of London* 60.359-367, pp. 489–498.
- Titterton, D. M. and A. N. Halliday (1979). “On the fitting of parallel isochrons and the method of maximum likelihood”. In: *Chemical Geology* 26, pp. 183–195.
- Vermeesch, P. (2015). “Revised error propagation of $^{40}\text{Ar}/^{39}\text{Ar}$ data, including covariances”. In: *Geochimica et Cosmochimica Acta* 171, pp. 325–337.
- York, D. (1969). “Least squares fitting of a straight line with correlated errors”. In: *Earth and Planetary Science Letters* 5, pp. 320–324.
- York, D. et al. (2004). “Unified equations for the slope, intercept, and standard errors of the best straight line”. In: *American Journal of Physics* 72.3, pp. 367–375.

Chapter 14

Generic functions

14.1 Weighted mean and outlier detection

`IsoplotR` uses a modified version of Chauvenet’s criterion for outlier detection. Given a set of n age estimates $t = \{t_1, \dots, t_n\}$, and their standard errors $\{s[t_1], \dots, s[t_n]\}$, the conventional version of this criterion proceeds as follows:

1. Compute the (unweighted) arithmetic mean (\bar{t}) and standard deviation ($s[t]$) of the n age determinations:

$$\bar{t} = \sum_{i=1}^n t_i/n \text{ and } s[t] = \sqrt{\sum_{i=1}^n (t_i - \bar{t})^2 / (n - 1)}$$

2. For each of the t_i s, compute the probability p_i that $|\tau| > |t_i - \bar{t}|$ for

$$\tau \sim \mathcal{N}(\mu = 0, \sigma^2 = s[t]^2)$$

3. Let $p_j \equiv \min(p_1, \dots, p_n)$. If $p_j < 0.05/n$, then reject the j^{th} date, reduce n by one (i.e., $n \rightarrow n - 1$) and repeat steps 1 through 3 until all the surviving dates pass the third step.

Although this procedure is effective at removing outliers in *homoscedastic* datasets, in which all datapoints are derived from a single Normal distribution, it is unable to account for *heteroscedasticity*, in which different samples are characterised by different analytical uncertainties ($s[t_i]$ in Equation 13.15). `IsoplotR` introduces a heuristic modification to Chauvenet’s criterion that detects outliers among heteroscedastic data. For model-1 fits:

1. Compute the error-weighted mean of the n age determinations t_i using their analytical uncertainties $s[t_i]$ by solving Equation 13.15 for μ .
2. Let $\hat{\mu}$ be the maximum likelihood estimate for μ and let $\sigma[\hat{\mu}]$ be its standard error. For each t_i , compute the probability p_i that $|\tau| > |t_i - \hat{\mu}|$ under a normal distribution with mean $\mu = 0$ and variance $\sigma^2 = s[t_i]^2$ (if the data are not overdispersed), or $\sigma^2 = MSWD \times s[t_i]^2$ (if the data are significantly overdispersed).
3. Proceed as before.

For a model-3 fit, the algorithm becomes:

1. Compute the error-weighted mean of the n age determinations t_i using their analytical uncertainties $s[t_i]$ by solving Equation 13.20 for μ and ω . Let $\hat{\mu}$ and $\hat{\omega}$ be their respective maximum likelihood estimates.

2. For each t_i , compute the probability p_i that $|\tau| > |t_i - \hat{\mu}|$ under a normal distribution with mean $\mu = 0$ and variance $\sigma^2 = s[t_i]^2 + \hat{\omega}^2$.
3. Proceed as before.

If the analytical uncertainties are small compared to the scatter between the dates (i.e., if the p-value of the chi-square test is less than α in a model-1 fit, or if $\omega \gg s[t_i]$ for all i in a model-2 fit), then this generalised algorithm reduces to the conventional Chauvenet criterion. If, on the other hand, the analytical uncertainties are large and the data do not exhibit any overdispersion, then the heuristic outlier detection method is similar to Ludwig (2003)'s 'modified 2-sigma' approach.

The weighted mean calculation is accompanied by a diagram that consists of a number of rectangular boxes (one for each date) whose vertical position and height reflect the ages and their analytical uncertainties, respectively (Figure 13.5). Outliers are marked in a different colour if so requested. The weighted mean plot offers an effective way, although arguably not *the* most effective way, to assess the dispersion of geochronological data. A better alternative is discussed in Section 14.3.

14.2 Frequency distributions

Empirical cumulative distribution functions or 'Cumulative Age Distributions' (CADs) are the most straightforward way to visualise the frequency distribution of multiple dates. A CAD is a step function that sets out the rank order of the dates against their numerical value:

$$\text{CAD}(t) = \sum_{i=1}^n 1(t < t_i) / n \quad (14.1)$$

where $1(*) = 1$ if $*$ is true and $1(*) = 0$ if $*$ is false. CADs have two desirable properties (Vermeesch, 2007). First, they do not require any pre-treatment or smoothing of the data. This Section will show that this is not the case for all data visualisation methods. Second, it is easy to superimpose several CADs on the same plot. This facilitates the intercomparison of multiple samples.

The interpretation of CADs is straightforward but not very intuitive. The prominence of individual age components is proportional to the steepness of the CAD (Figure 14.2.a). This is different from probability density estimates such as histograms, in which such components stand out as peaks (Figure 14.2.b). Peaks are arguably easier to identify than inflection points and this is probably why CADs are not more widely used as a data visualisation tool. But the ease of interpretation of density estimates comes at a cost, as they require smoothing and cannot as easily be combined as CADs. `IsoplotR` implements two kinds of density estimates.

Histograms smooth data by binning. `IsoplotR` uses Sturges' Rule ($\log_2[n] + 1$, where n is the number of data points) to determine the default number of histogram bins, but this can be changed to any other positive integer by the user. Alternatively, kernel density estimates (KDEs Vermeesch, 2012) smooth data by applying a (Gaussian) kernel:

$$\text{KDE}(t) = \sum_{i=1}^n \mathcal{N}(t | \mu = t_i, \sigma^2 = h_i^2) / n \quad (14.2)$$

where h_i is the smoothing parameter or ‘bandwidth’ of the kernel density estimate. Using a constant value for h_i across the entire range of measurements produces a ‘fixed’ bandwidth estimator. If h_i varies between the sample points, then $\text{KDE}(t)$ is known as an ‘adaptive’ KDE.

The rationale behind adaptive kernel density estimation is to use a narrower bandwidth near the peaks of the sampling distribution (where the ordered dates are closely spaced in time), and a wider bandwidth in the distribution’s sparsely sampled troughs. Thus, the resolution of the density estimate is optimised according to data availability.

The default bandwidth used by `IsoplotR` is calculated using the algorithm of Botev, Gro-towski, and Kroese (2010) and modulated by the adaptive smoothing approach of Abramson (1982), whereby:

$$h_i = h\sqrt{G/kde(t_i)}$$

in which $kde(t_i)$ is the ‘pilot density’ using a fixed bandwidth (h) evaluated at t_i , and G is the geometric mean of the pilot density over all the sample points (Van Kerm, 2003).

Kernel density estimates are not to be confused with `Isoplot`’s ‘probability density plots’ (PDPs). The mathematical definition of a PDP closely resembles that of the KDE, the only difference being the substitution of the bandwidth h_i by the analytical uncertainty $s[t_i]$ in Equation 14.2. This similarity in appearance and definition is the source of much confusion.

The rationale behind PDPs is to emphasise the ‘good’ data (the most precise measurements stand out as peaks), and to reduce the prominence of ‘bad’ data (imprecise measurements are smoothed out by a broad kernel). Reasonable though that might seem at first glance, this procedure does not stand up to further scrutiny. For example, when applied to high precision datasets, where $s[t_i]$ is very small compared to the range of t_i -values, the PDP breaks down into a sequence of spikes. Further examples and a more complete discussion of the case against PDPs are presented by Vermeesch (2012) and Vermeesch (2018a).

This discussion leaves us with one question: if PDPs are not a valid data visualisation tool, then how should one account for the heteroscedasticity of geochronological data? `IsoplotR` implements two alternative options. The first of these is the weighted mean plot (Section 14.1). Although this diagram does show both the individual age estimates and their analytical uncertainties, it is not very effective at revealing components of clustered ages, especially in large ($n > 50$, say) datasets. The second option is the radial plot, which is discussed in Section 14.3.

14.3 Radial plots

The radial plot is a graphical device that was specifically designed to display heteroscedastic data, and is constructed as follows. Consider the usual set of dates t_i and uncertainties $s[t_i]$ (for $1 \leq i \leq n$); define $z_i = z(t_i)$ to be a transformation of t_i ; and let $s[z_i]$ be its propagated analytical uncertainty. For example,

$$\begin{cases} z_i &= \ln[t_i] \\ s[z_i] &= s[t_i]/t_i \end{cases} \quad (14.3)$$

in the case of a logarithmic transformation. Then the radial plot is a scatter plot of (x_i, y_i)

values, where

$$x_i = 1/s[z_i]$$

$$\text{and } y_i = \frac{z_i - z_o}{s[z_i]} \quad (14.4)$$

in which z_o is some reference value such as the mean. The slope of a line connecting the origin of this scatter plot with any of the (x_i, y_i) s is proportional to z_i and, hence, a function of the date t_i .

It is helpful to draw a radial scale at some convenient distance from the origin and annotating it with labelled ticks at the appropriate angles. While the angular position of each data point represents the date, its horizontal distance from the origin is proportional to the precision. Imprecise measurements plot on the left-hand side of the radial plot, whereas precise age determinations are found further towards the right. Thus, radial plots allow the observer to assess both the magnitude and the precision of quantitative data in one glance (Figure 14.1).

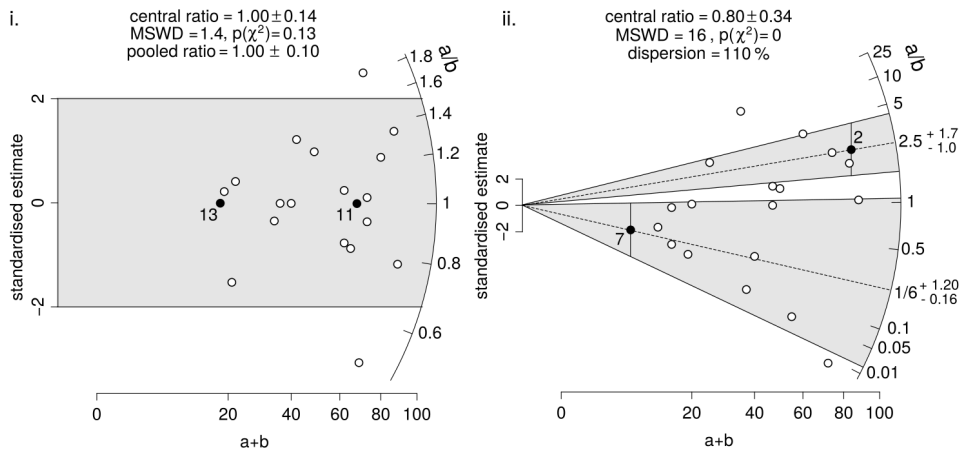


Figure 14.1: Radial plots for two synthetic datasets from Vermeesch (2018b). i) approximately 95% of the samples in Data 1 plot within a symmetric ‘2-sigma’ band around the origin. These data are therefore compatible with a single homogeneous population, and pass the chi-square test. ii) the age of each aliquot can be obtained by projecting the corresponding scatter point onto the radial scale. Projecting a ‘2-sigma’ error bar onto the same scale yields the 95% confidence intervals of $t_2 = 2.5 + 1.7 / -1.0$ and $t_7 = 0.17 + 1.20 / -0.16$. The second sample does not fit within a ‘2-sigma’ band, and is more adequately described by a random effects model with two parameters: the central ratio and the dispersion.

Radial plots are widely used in fission track and luminescence dating (Galbraith, 1990; Galbraith et al., 1999), but are yet to find their way into other branches of geochronology. *IsoplotR* generalises this valuable tool to all types of geochronological data. In addition to being an effective way to visualise heteroscedastic data, the radial plot also represents a convenient vehicle for further data interpretation and modelling, as will be discussed Section 14.4.

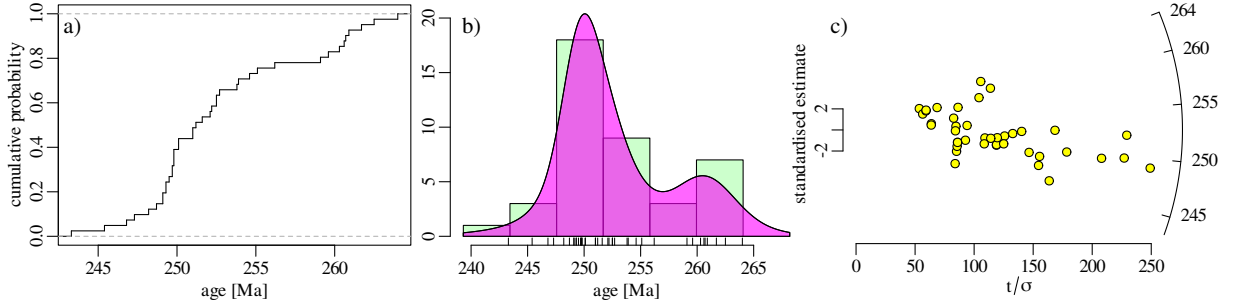


Figure 14.2: a) CAD, b) histogram/KDE and c) radial plot of the same dataset (from Ludwig, 2003).

14.4 Mixture models

The weighted mean algorithm outlined in Sections 13.3 and 14.1 assumes that geochronological data obey normal statistics. This assumption may be approximately correct for high precision datasets but must inevitably be incorrect for low precision ones.

Geologic time is a strictly positive quantity that is incompatible with the symmetric Gaussian bell curve, which is defined over the range of values from $-\infty$ to $+\infty$. Because geochronological datasets must be strictly positive, their uncertainty distributions must be asymmetric, with skewness being inversely proportional to precision. This asymmetry is removed by the logarithmic transformation that is used to construct radial plots (Equation 14.3), and which can also be applied to KDEs:

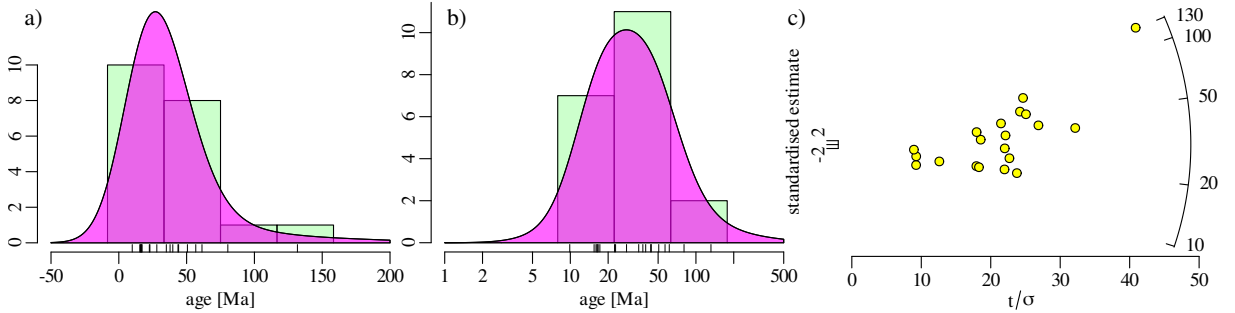


Figure 14.3: Young U–Pb carbonate dates shown a) on a linear scale, whose KDE spills over into nonsensical negative data space, and b) on a logarithmic scale, which fixes this problem. c) shows the same data as a radial plot with a logarithmic time scale.

We can reformulate Equation 13.15 in terms of the transformed variables z_i :

$$p(z_i|\mu, \omega) = \mathcal{N}(\mu, \sigma^2 = s[z_i]^2 + \omega^2) \quad (14.5)$$

which can be solved by the method of maximum likelihood as before, yielding two estimates $\hat{\mu}$ and $\hat{\omega}$. The **central age** is defined as $\exp(\hat{\mu})$, and $\hat{\omega}$ represents the (over)dispersion of the data. This is a relative quantity (due to the log-transform) that estimates the coefficient of variation of the true ages. The difference between the central age and the weighted mean age is usually small unless the data are imprecise and/or strongly overdispersed. In those cases, the central age yields the geologically most meaningful value.

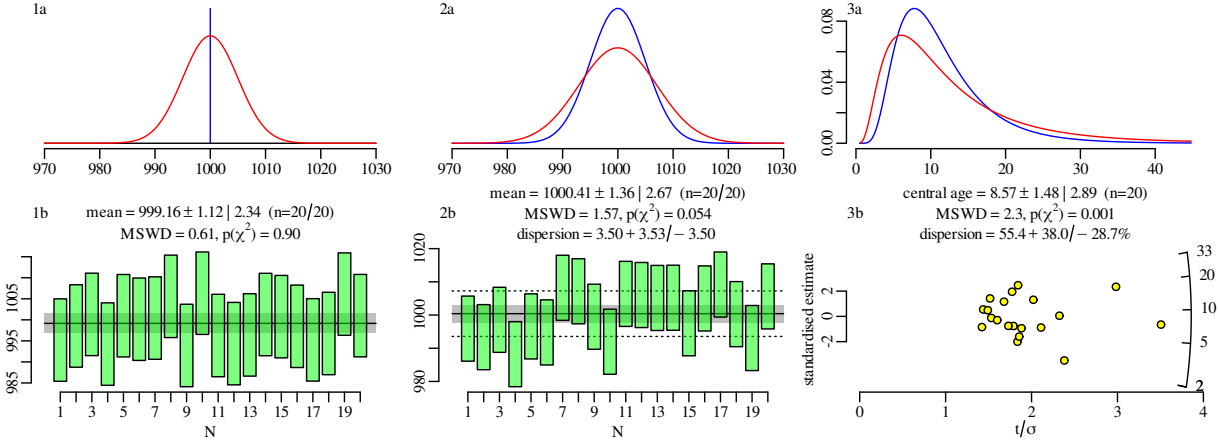


Figure 14.4: Three different age models implemented in `IsoplotR`. 1a) If the true age is a discrete event (blue peak at 1000 Ma), and the analytical uncertainties follow a normal distribution with zero mean and 5 Ma standard deviation, then the predicted distribution of the dates (red line) is a normal distribution with mean at 1000 Ma and a 5 Ma standard deviation. 1b) In this case the ordinary weighted mean (Equation 13.15) is the most appropriate estimator of the true age. 2a) If the true age is drawn from a normal distribution with a mean of 1000 Ma and a standard deviation of 5 Ma (blue line), and if the analytical uncertainties follow a normal distribution with zero mean and 5 Ma standard deviation, then the predicted distribution of the dates (red line) is a normal distribution with mean at 1000 Ma and a $\sqrt{50}$ Ma standard deviation. 2b) In this case the random effects model of Equation 13.20 is the most appropriate estimator of the mean *and* the standard deviation of the true ages. The latter parameter is reported as the dispersion in the legend. 3a) If the true ages are drawn from a lognormal distribution with location parameter 10 Ma and a dispersion parameter of 50% (blue line), and the analytical uncertainties are $\sim 50\%$, then the distribution of the measured dates (red line) is a lognormal distribution with $10/\sqrt{2}\%$ dispersion parameter. 3b) In this case the random effects model of Equation 14.5 is the best way to average the data, and the radial plot with logarithmic scale is the best way to visualise the results.

The random effects model represented by Equation 14.5 is referred to as a **continuous mixture** model. It assumes that the overdispersion of the data is caused by a continuous process that yields a (log)normal distribution of true ages. As previously mentioned in Section 13.4, one example of such a process is the fractional crystallisation of plutons, which may take hundreds of thousands of years, resulting in a range of zircon U-Pb ages. A second example is the gradual cooling of tectonic blocks during exhumation, which may cause the fission track system in compositionally heterogeneous apatite populations to ‘close’ at different times. However, such continuous processes are by no means the only cause of overdispersion in geochronology.

Consider, for instance, a detrital mixture originating from two or more differently aged sources. Such a **discrete mixture** is more adequately described by the following equation:

$$\mathcal{LL}(\boldsymbol{\mu}, \boldsymbol{\pi} | \mathbf{z}, \mathbf{s}[\mathbf{z}]) = \sum_{i=1}^n \ln \left[\sum_{j=1}^k \pi_j \mathcal{N}(z_i | \mu_j, s[z_i]^2) \right] \quad (14.6)$$

where $\boldsymbol{\mu} = \{\mu_1, \dots, \mu_k\}$, $\boldsymbol{\pi} = \{\pi_1, \dots, \pi_k\}$, $\mathbf{z} = \{z_1, \dots, z_k\}$, $\mathbf{s}[\mathbf{z}] = \{s[z_1], \dots, s[z_k]\}$, k is the number of components, μ_j is the mean of the j^{th} component (so that $\exp[\mu_j]$ is the corresponding age), and π_j is the proportion of the population that belongs to the j^{th} component. Equation 14.6 comprises n measurements and $2k - 1$ unknowns (μ_j and π_j for $1 \leq j \leq k$ with

$\pi_k = 1 - \sum_{j=1}^{k-1} \pi_j$). It can be solved by the method of maximum likelihood.

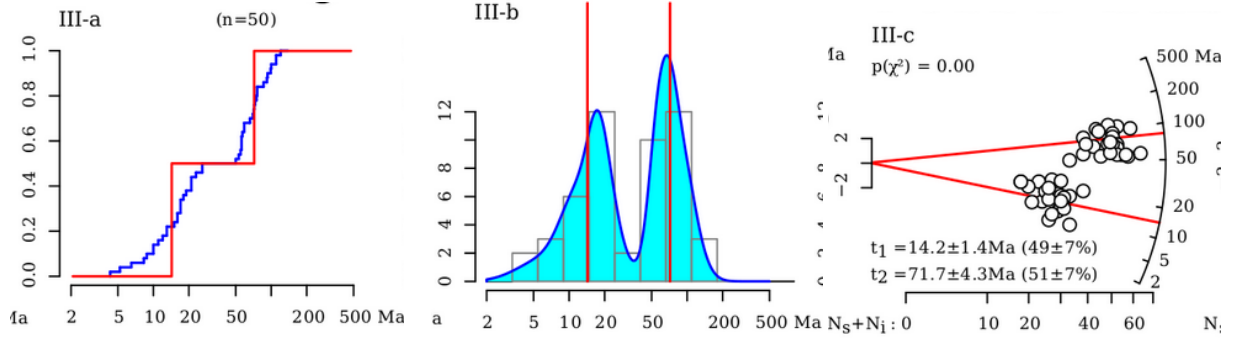


Figure 14.5: a) cumulative distribution of the true ages of a binary mixture of two discrete age components (red) and the CAD of the measured ages of 50 measured dates (blue). b) histogram and KDE of the binary mixture. c) results of the mixture model, shown as a radial plot.

Choosing the right number of components (k) is a problem that merits further discussion. *IsoplotR* implements the Bayes Information Criterion (BIC) as a way to automatically pick the ‘optimal’ value of k for any given dataset (Section 5.6 of Galbraith, 2005). But this option should be used with caution because, for real datasets, the number of components always increases with sample size. This happens because the power of Equation 14.6 to resolve even the smallest degree of overdispersion increases with sample size.

Suppose that one uses the youngest component produced by the BIC algorithm to estimate the maximum depositional age of a sedimentary sequence. Then the resulting value would never converge to a specific value. Instead, one would find this minimum age to drift to ever younger values until a point where the youngest age component in a large dataset becomes younger than the actual depositional age. In most cases it is, therefore, best to resist the temptation to use the automatic peak fitting option. It is better to choose a specific number of components instead, based on geological considerations.

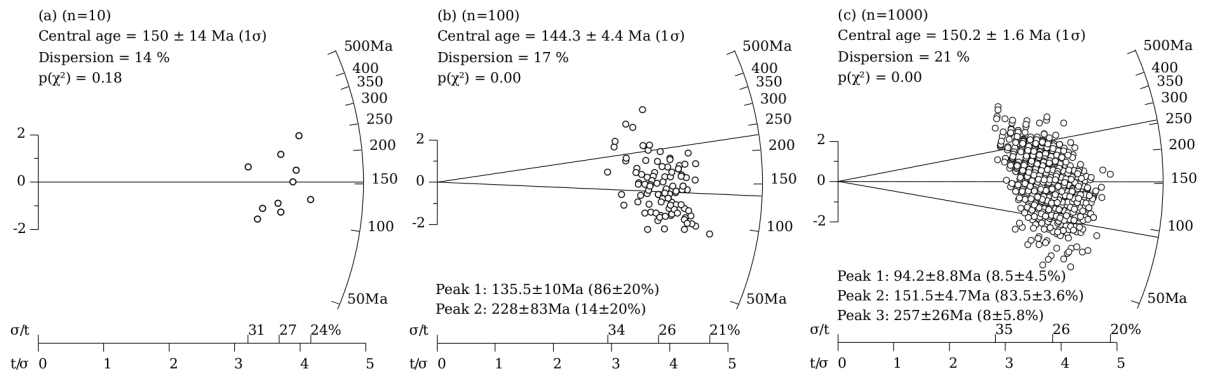


Figure 14.6: Application of finite mixture modelling to a continuous mixture. Increasing sample size from left (a) to right (c) provides statistical justification to fit more components. Note that the age of the youngest age component gets progressively younger with increasing sample size, from 150 Ma for sample (a) to 94 Ma for sample (c), and is therefore not a reliable estimator of the minimum age. Figure adapted from Vermeesch (2018c).

If one is mainly interested in the youngest age component, then it is more productive to

use an alternative parameterisation, in which all grains are assumed to come from one of two components, whereby the first component is a single discrete age peak ($\exp[\gamma]$, say) and the second component ($\mathcal{N}'(\dots)$) is a continuous distribution such as Equation 14.5, but truncated at this discrete value.

$$\mathcal{LL}(\pi, \gamma, \mu, \omega | \mathbf{z}, \mathbf{s}[\mathbf{z}]) = \sum_{j=1}^n \ln[\pi \mathcal{N}(z_i | \gamma, s[z_i]^2) + (1 - \pi) \mathcal{N}'(z_i | \mu, s[z_i]^2 + \omega^2)] \quad (14.7)$$

One caveat is that, if this minimum age model is applied to relatively small and/or high precision datasets such as most U-Pb measurements, then the minimum age estimate will simply be equal to the youngest date. It is only for large and/or low precision datasets (such as fission tracks), that the minimum age estimate will be older than the youngest grain. Crucially, this value will not drift to smaller values with increasing sample size, but will converge to a distinct minimum age.

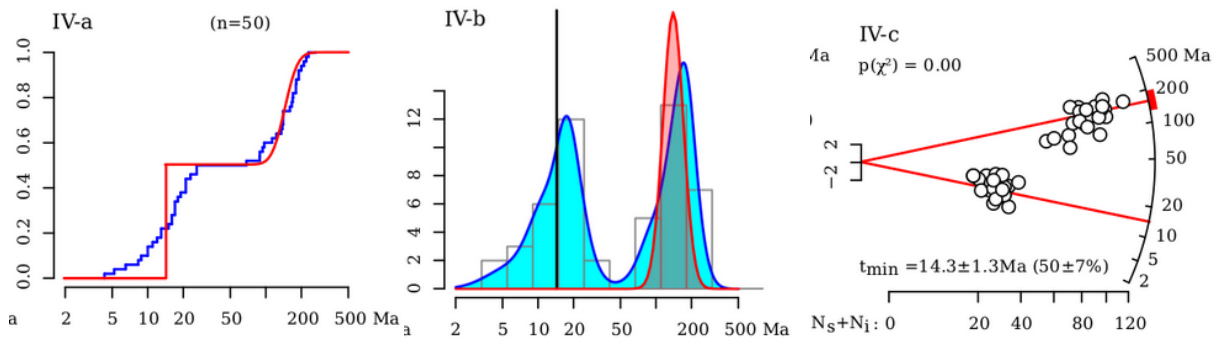


Figure 14.7: A binary mixture combining discrete and continuous age components shown as a) CADs and b) histograms and KDEs, with the true age components shown in red, and the measured age distribution in blue. c) radial plot with the minimum age model of Equation 14.7.

References

- Abramson, I. S. (1982). “On bandwidth variation in kernel estimates – a square root law”. In: *The Annals of Statistics*, pp. 1217–1223.
- Botev, Z. I., J. F. Grotowski, and D. P. Kroese (2010). “Kernel density estimation via diffusion”. In: *Annals of Statistics* 38 (5), pp. 2916–2957.
- Galbraith, R. F. (1990). “The radial plot: graphical assessment of spread in ages”. In: *Nuclear Tracks and Radiation Measurements* 17, pp. 207–214.
- (2005). *Statistics for fission track analysis*. CRC Press, p. 219.
- Galbraith, R. F. et al. (1999). “Optical dating of single and multiple grains of quartz from Jinmium rock shelter, northern Australia: Part I, experimental design and statistical models”. In: *Archaeometry* 41.2, pp. 339–364.
- Ludwig, K. R. (2003). “User’s manual for Isoplot 3.00: a geochronological toolkit for Microsoft Excel”. In: *Berkeley Geochronology Center Special Publication* 4 4.
- Van Kerm, P. (2003). “Adaptive kernel density estimation”. In: *The Stata Journal* 3.2, pp. 148–156.
- Vermeesch, P. (2007). “Quantitative geomorphology of the White Mountains (California) using detrital apatite fission track thermochronology”. In: *Journal of Geophysical Research (Earth Surface)* 112.F11, p. 3004. DOI: 10.1029/2006JF000671.
- (2012). “On the visualisation of detrital age distributions”. In: *Chemical Geology* 312-313, pp. 190–194. DOI: 10.1016/j.chemgeo.2012.04.021.

- (2018a). “Dissimilarity measures in detrital geochronology”. In: *Earth-Science Reviews* 178, pp. 310–321. DOI: 10.1016/j.earscirev.2017.11.027.
- (2018b). “Statistical models for point-counting data”. In: *Earth and Planetary Science Letters* 501, pp. 1–7.
- (2018c). “Statistics for fission tracks”. In: *Fission track thermochronology and its application to geology*. Ed. by M. Malusá and P. Fitzgerald. Springer.

Chapter 15

U–Pb geochronology

The U–(Th–)Pb method is a rich and complex system of three radioactive decay chains that provide chronometric constraints on a wide range of geological processes, mineral phases and time scales. U–Pb data acquisition may focus on high throughput (using LA-ICP-MS), on high spatial resolution (SIMS) or on high precision (TIMS), and each of these analytical approaches comes with its own tradeoffs. To accommodate this diversity in equipment and applications, `IsoplotR`'s U–Pb functions are more extensive than those of any other geochronometer. This Chapter provides an in-depth overview of these functions.

Section 15.1 introduces eight different input formats that accommodate different types of input data. Section 15.2 discusses three different types of concordia diagrams that can be used to visually assess the degree to which the data form a closed isotopic system, and to calculate the best age of such ‘concordant’ data. Concordant data form the bedrock of the high precision geochronology and the geologic time scale. The remainder of the Chapter discusses various strategies to deal with discordant U–Pb compositions. Discordance can be caused by a range of mechanisms, such as:

1. non-radiogenic (‘common’) Pb.
2. mixing of different growth zones in a texturally complex mineral grain.
3. Pb-loss (or U-gain).
4. initial disequilibrium of the ^{235}U and ^{238}U decay chains.

The first three mechanisms give rise to linear (or planar) trends in Wetherill or Tera-Wasserburg concordia space. Section 15.3 shows how to fit a line (or plane) through such data by constrained optimisation. Section 15.4 shows how such isochrons (or ‘discordia’) lines provides one way to correct for common Pb, but introduces a few other correction strategies as well. Section 15.5 shows how initial enrichment or depletion of short-lived nuclides such as ^{234}U , ^{230}Th , ^{226}Ra or ^{231}Pa can bias U–Pb ages by as much as a million years, and reviews some strategies to reduce this bias. Finally, Section 15.6 introduces methods to filter discordant datasets for detrital geochronology.

15.1 Input formats

`IsoplotR` offers eight different input formats:

1. $\frac{07}{35}$, $\text{err}[\frac{07}{35}]$, $\frac{06}{38}$, $\text{err}[\frac{06}{38}]$, $r[\frac{06}{38}, \frac{06}{38}]$

2. $\frac{38}{06}, \text{err}[\frac{38}{06}], \frac{07}{06}, \text{err}[\frac{07}{06}], (r[\frac{38}{06}, \frac{07}{06}])$
3. $\frac{07}{35}, \text{err}[\frac{07}{35}], \frac{06}{38}, \text{err}[\frac{06}{38}], \frac{07}{06}, \text{err}[\frac{07}{06}], (r[\frac{07}{35}, \frac{06}{38}]), (r[\frac{07}{35}, \frac{07}{06}]), (r[\frac{06}{38}, \frac{07}{06}])$
4. $\frac{07}{35}, \text{err}[\frac{07}{35}], \frac{06}{38}, \text{err}[\frac{06}{38}], \frac{04}{38}, \text{err}[\frac{04}{38}], (r[\frac{07}{35}, \frac{06}{38}]), (r[\frac{07}{35}, \frac{04}{38}]), (r[\frac{06}{38}, \frac{04}{38}])$
5. $\frac{38}{06}, \text{err}[\frac{38}{06}], \frac{07}{06}, \text{err}[\frac{07}{06}], \frac{04}{06}, \text{err}[\frac{04}{06}], (r[\frac{38}{06}, \frac{07}{06}]), (r[\frac{38}{06}, \frac{04}{06}]), (r[\frac{07}{06}, \frac{04}{06}])$
6. $\frac{07}{35}, \text{err}[\frac{07}{35}], \frac{06}{38}, \text{err}[\frac{06}{38}], \frac{04}{38}, \text{err}[\frac{04}{38}], \frac{07}{06}, \text{err}[\frac{07}{06}], \frac{04}{07}, \text{err}[\frac{04}{07}], \frac{04}{06}, \text{err}[\frac{04}{06}]$
7. $\frac{07}{35}, \text{err}[\frac{07}{35}], \frac{06}{38}, \text{err}[\frac{06}{38}], \frac{08}{32}, \text{err}[\frac{08}{32}], \frac{32}{38}, \text{err}[\frac{32}{38}],$
 $(r[\frac{07}{35}, \frac{06}{38}]), (r[\frac{07}{35}, \frac{08}{32}]), (r[\frac{07}{35}, \frac{32}{38}]), (r[\frac{06}{38}, \frac{08}{32}]), (r[\frac{06}{38}, \frac{32}{38}]), (r[\frac{08}{32}, \frac{32}{38}])$
8. $\frac{38}{06}, \text{err}[\frac{38}{06}], \frac{07}{06}, \text{err}[\frac{07}{06}], \frac{08}{06}, \text{err}[\frac{08}{06}], \frac{32}{38}, \text{err}[\frac{32}{38}],$
 $(r[\frac{38}{06}, \frac{07}{06}]), (r[\frac{38}{06}, \frac{08}{06}]), (r[\frac{38}{06}, \frac{32}{38}]), (r[\frac{07}{06}, \frac{08}{06}]), (r[\frac{07}{06}, \frac{32}{38}]), (r[\frac{08}{06}, \frac{32}{38}])$

where 04, 06, 07, 08, 32, 35 and 38 stand for ^{204}Pb , ^{206}Pb , ^{207}Pb , ^{208}Pb , ^{232}Th , ^{235}U and ^{238}U , respectively. ‘err[*]’ stands for the analytical uncertainty of *, which can be specified as a standard error or as two times the standard error, either in absolute or relative units. And ‘r[x,y]’ stands for the error correlation between x and y .

Formats 1–3 are meant for mass spectrometers that are unable to accurately measure ^{204}Pb . This is the case for single collector ICP-MS instruments that are unable to resolve the isobaric interference on ^{204}Hg , which is often present in the plasma gas. Formats 4–6 include ^{204}Pb , as measured by SIMS, TIMS or multi-collector ICP-MS. Finally, formats 7 and 8 include ^{208}Pb and ^{232}Th . These nuclides can be used for hybrid U–Th–Pb dating, as discussed in Section 5.1.

Formats 1, 4 and 7 are ‘Wetherill style’ input formats, in which the radioactive parent appears in the denominator of the isotopic ratio data. As explained in Section 13.5 and shown in Figure 13.6, these formats are associated with strong error correlations ($r[\frac{07}{35}, \frac{06}{38}]$), which must be specified so as to avoid inaccurate inferences. Formats 2, 5 and 8 are ‘Tera-Wasserburg style’ input formats, in which the most abundant radiogenic daughter (i.e., ^{206}Pb) appears in the denominator of the isotopic ratio data. As shown in Figure 13.7, this greatly reduces the error correlations which, consequently, are optional (hence the brackets around $r[\frac{38}{06}, \frac{07}{06}]$).

Finally, formats 3 and 6 provide an alternative input format designed for users whose low level data processing software does not provide error correlation data. It uses redundant ratios to infer the correlation coefficients. Let $X \equiv \frac{07}{35}$, $Y \equiv \frac{07}{35}$, $Z \equiv \frac{07}{06}$ and $U \equiv \frac{38}{35}$, let $s[X]$, $s[Y]$ and $s[Z]$ be the standard errors of X , Y and Z , and assume that $s[U] = 0$ for the sake of simplicity. Then it is easy to see that $Z = X/(UY)$, and

$$\left(\frac{s[Z]}{Z}\right)^2 = \left(\frac{s[X/Y]}{X/Y}\right)^2 \approx \left(\frac{s[X]}{X}\right)^2 + \left(\frac{s[Y]}{Y}\right)^2 - 2\frac{s[X,Y]}{XY} \quad (15.1)$$

from which the covariance (and, hence, the correlation coefficient) between X and Y can be inferred as

$$s[X,Y] \approx \frac{XY}{2} \left[\left(\frac{s[X]}{X}\right)^2 + \left(\frac{s[Y]}{Y}\right)^2 - \left(\frac{s[Z]}{Z}\right)^2 \right] \quad (15.2)$$

It is important to note that this approach makes the crucial assumption that all three standard errors ($s[X]$, $s[Y]$ and $s[Z]$) are based on the same number of data points. This means that formats 3 and 6 are not applicable to TIMS data.

15.2 Concordia diagrams and ages

IsoplotR implements three types of concordia diagram:

1. The **Wetherill** concordia diagram sets out the $^{206}\text{Pb}/^{238}\text{U}$ vs. the $^{207}\text{Pb}/^{235}\text{U}$ ratios. This format introduces relatively strong error correlations (see Section 13.5). The addition of common Pb pulls samples away from concordia along a line whose slope is proportional to the common Pb composition. Isotopic compositions above the concordia line are ‘forbidden’. They could, in principle, be caused by U-loss. But in practice this mechanism is implausible.
2. The **Tera-Wasserburg** concordia diagram uses the inverse isochron ratios $^{207}\text{Pb}/^{206}\text{Pb}$ vs. and $^{238}\text{U}/^{206}\text{Pb}$. This format exhibits weaker error correlations. The addition of common Pb creates a binary mixing line between radiogenic and common Pb compositions (see Section 15.3). The area below the concordia line is ‘forbidden’ and the only reason why samples may plot there is due to random chance and analytical imprecision.
3. The **U–Th–Pb concordia** diagram sets out the conventional isochron ratios of $^{208}\text{Pb}/^{232}\text{Th}$ vs. $^{206}\text{Pb}/^{238}\text{U}$. Like the Wetherill diagram, the U–Th–Pb diagram also exhibits strong error correlations. But in contrast with the Wetherill diagram, the addition of common Pb does not necessarily create linear trends on the U–Th–Pb diagram. Instead, different aliquots may end up on either side of the concordia line depending on their Th/U ratio.

The Wetherill and Tera-Wasserburg concordia plots are available to datasets from any of IsoplotR’s eight input formats, irrespective of whether the ratios are stored in a Wetherill or Tera-Wasserburg format. IsoplotR automatically handles the data conversions internally. The U–Th–Pb concordia plot is only available for data formats 7 and 8, because these are the only formats that account for ^{208}Pb and ^{232}Th . The remainder of this Chapter will focus on the Wetherill and Tera-Wasserburg diagrams, except for Section 15.4, which will briefly mention the U–Th–Pb diagram again.

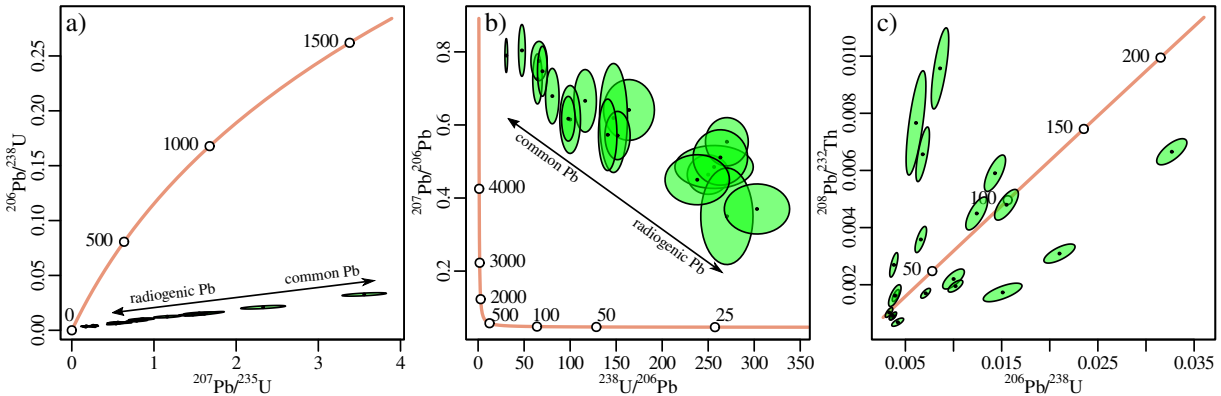


Figure 15.1: The allanite dataset of Janots and Rubatto (2014) shown on a) Wetherill, b) Tera-Wasserburg and c) U–Th–Pb concordia diagrams.

In the absence of (or after correction for) common Pb or other complications, multiple aliquots from the same sample may plot on the concordia line. Such samples are said to be concordant. Their ‘most likely’ age (in a statistical sense) is known as the **concordia age**. Calculating a concordia age involves two steps (Ludwig, 1998):

1. Calculate the two-dimensional error-weighted average ($\{\bar{x}, \bar{y}\}$) of the U–Pb ratios, by minimising the sum of squares S or, equivalently, by maximising the likelihood for equivalence

\mathcal{LL}_e . In Wetherill space:

$$\mathcal{LL}_e \propto -\frac{S_e}{2} = -\frac{1}{2} \sum_{i=1}^n \left[\begin{bmatrix} \frac{07}{35} \\ \frac{06}{38} \end{bmatrix}_i - \bar{x} \right]^T \begin{bmatrix} s \left[\frac{07}{35} \right]_i^2 & s \left[\frac{07}{35}, \frac{06}{38} \right]_i \\ s \left[\frac{07}{35}, \frac{06}{38} \right]_i & s \left[\frac{06}{38} \right]_i^2 \end{bmatrix}^{-1} \begin{bmatrix} \left[\frac{07}{35} \right]_i - \bar{x} \\ \left[\frac{06}{38} \right]_i - \bar{y} \end{bmatrix} \quad (15.3)$$

or in Tera-Wasserburg space:

$$\mathcal{LL}_e \propto -\frac{S_e}{2} = -\frac{1}{2} \sum_{i=1}^n \left[\begin{bmatrix} \frac{38}{06} \\ \frac{07}{06} \end{bmatrix}_i - \bar{x} \right]^T \begin{bmatrix} s \left[\frac{38}{06} \right]_i^2 & s \left[\frac{38}{06}, \frac{07}{06} \right]_i \\ s \left[\frac{38}{06}, \frac{07}{06} \right]_i & s \left[\frac{07}{06} \right]_i^2 \end{bmatrix}^{-1} \begin{bmatrix} \left[\frac{38}{06} \right]_i - \bar{x} \\ \left[\frac{07}{06} \right]_i - \bar{y} \end{bmatrix} \quad (15.4)$$

Using standard maximum likelihood theory, the covariance matrix of the weighted mean composition ($\Sigma_{\bar{x}, \bar{y}}$) is obtained by inverting the Fisher information matrix.

2. Given the concordia composition $\{\bar{x}, \bar{y}\}$ obtained in the previous step, compute the most likely age (t_c) of this concordia composition. This is done by maximising the likelihood of concordance. In Wetherill space:

$$\mathcal{LL}_c \propto -\frac{S_c}{2} = -\frac{1}{2} \sum_{i=1}^n \left[\begin{array}{c} \bar{x} - (\exp[\lambda_{235} t_c] - 1) \\ \bar{y} - (\exp[\lambda_{238} t_c] - 1) \end{array} \right]^T \Sigma_{\bar{x}, \bar{y}}^{-1} \left[\begin{array}{c} \bar{x} - (\exp[\lambda_{235} t_c] - 1) \\ \bar{y} - (\exp[\lambda_{238} t_c] - 1) \end{array} \right] \quad (15.5)$$

Or in Tera-Wasserburg space:

$$\mathcal{LL}_c \propto -\frac{S_c}{2} = -\frac{1}{2} \sum_{i=1}^n \left[\begin{array}{c} \bar{x} - \frac{1}{\exp[\lambda_{238} t_c] - 1} \\ \bar{y} - \left[\frac{35}{38} \right] \frac{\exp[\lambda_{235} t_c] - 1}{\exp[\lambda_{238} t_c] - 1} \end{array} \right]^T \Sigma_{\bar{x}, \bar{y}}^{-1} \left[\begin{array}{c} \bar{x} - \frac{1}{\exp[\lambda_{238} t_c] - 1} \\ \bar{y} - \left[\frac{35}{38} \right] \frac{\exp[\lambda_{235} t_c] - 1}{\exp[\lambda_{238} t_c] - 1} \end{array} \right] \quad (15.6)$$

Again, the uncertainty of t_c is obtained from the Fisher information matrix.

The same concordia age is obtained regardless of whether the calculations are carried out in Wetherill or Tera-Wasserburg space.

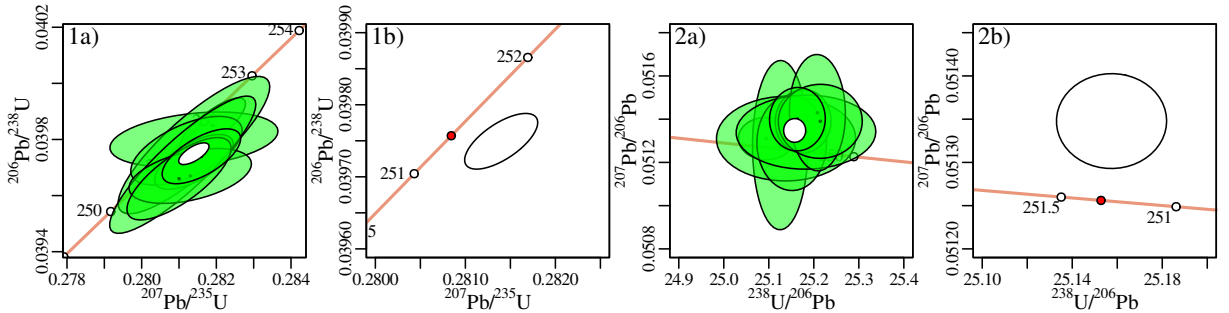


Figure 15.2: 1) Wetherill and 2) Tera-Wasserburg concordia diagram with a) the weighted mean composition shown as white error ellipse, and b) the concordia age (251.3 Ma) is shown as a red circle.

The goodness-of-fit can be quantified either using a chi-square test, or with the MSWD. We can define three p-values and three MSWD values:

concordance: $\text{MSWD}_c = S_c$

equivalence: $\text{MSWD}_e = S_e / (2n - 2)$

combined: $\text{MSWD} = (S_e + S_c)/(2n - 1)$

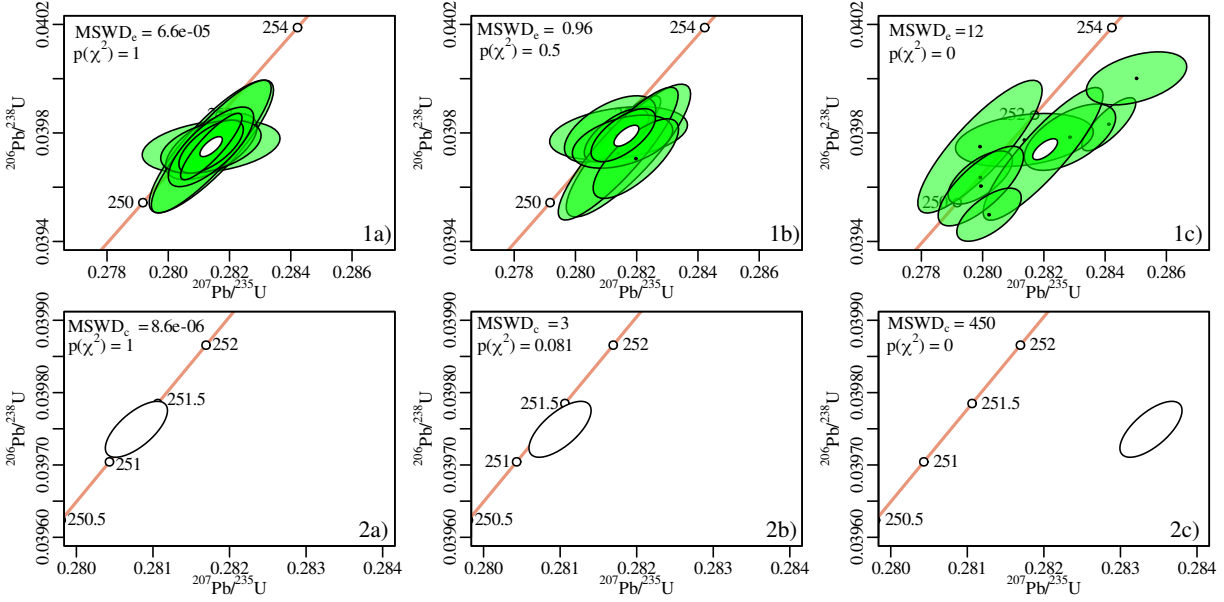


Figure 15.3: MSWDs and p-values for 1) equivalence and 2) concordance for data that are a) underdispersed, b) dispersed by an amount that is consistent with the analytical uncertainties, and c) overdispersed with respect to the analytical uncertainties.

In high precision geochronology, the analytical uncertainty of the uranium decay constants becomes a significant factor in assessing the degree of concordance. This uncertainty represents a systematic error, which can be added to the covariance matrix of the weighted mean composition:

$$\Sigma'_{\bar{x},\bar{y}} = \Sigma_{\bar{x},\bar{y}} + t_c^2 \begin{bmatrix} \exp[\lambda_{235}t_c] \\ \exp[\lambda_{238}t_c] \end{bmatrix}^T \begin{bmatrix} \sigma[\lambda_{235}]^2 & \sigma[\lambda_{235}, \lambda_{238}] \\ \sigma[\lambda_{235}, \lambda_{238}] & \sigma[\lambda_{238}]^2 \end{bmatrix} \begin{bmatrix} \exp[\lambda_{235}t_c] \\ \exp[\lambda_{238}t_c] \end{bmatrix} \quad (15.7)$$

where $\sigma[\lambda_{235}]$, $\sigma[\lambda_{238}]$ and $\sigma[\lambda_{235}, \lambda_{238}]$ are the (co)variances of the ^{235}U and ^{238}U decay constants. **IsoplotR** visualises the decay constant uncertainties by increasing the width of the concordia line, and takes them into account when calculating the MSWD and p-value of concordance:

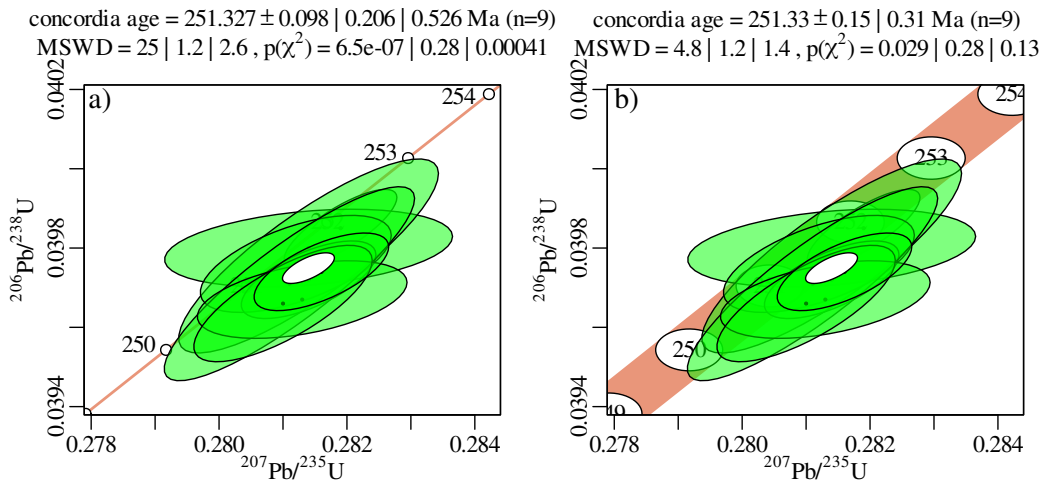


Figure 15.4: Wetherill concordia diagram with concordia age calculations a) without and b) with decay constant uncertainties. The legends report the MSWD and p-value for concordance | equivalence | concordance + equivalence. Taking into account the decay constant uncertainty decreases the value of MSWD_c and increases the p-value of concordance.

15.3 Discordia/isochron regression

As discussed in the introductory paragraphs of this Chapter, U–Pb data can form linear trends in Wetherill or Tera–Wasserburg concordia space due to:

1. the addition of non-radiogenic Pb components ('common Pb');
2. binary mixing of different aged growth zones;
3. partial loss of radiogenic Pb.

IsoplotR uses three different algorithms to fit these linear trends:

1. formats 1–3: Semitotal-U/Pb regression using $^{206}\text{Pb}/^{238}\text{U}$ and $^{207}\text{Pb}/^{238}\text{U}$. Let $\left[\frac{07}{06}\right]_i$ and $\left[\frac{38}{06}\right]_i$ be n $^{207}\text{Pb}/^{206}\text{Pb}$ and $^{238}\text{U}/^{206}\text{Pb}$ ratio measurements¹, respectively. Then this algorithm chooses the common Pb composition $\left[\frac{07}{06}\right]_o$ and concordia intercept age t that best fits the following mixing line in a maximum likelihood sense:

$$\left[\frac{07}{06}\right]_i = \left[\frac{07}{06}\right]_o - \left[\frac{38}{06}\right]_i \left\{ \left[\frac{07}{06}\right]_o (\exp[\lambda_{238}t] - 1) - \left[\frac{35}{38}\right]_i (\exp[\lambda_{235}t] - 1) \right\} \quad (15.8)$$

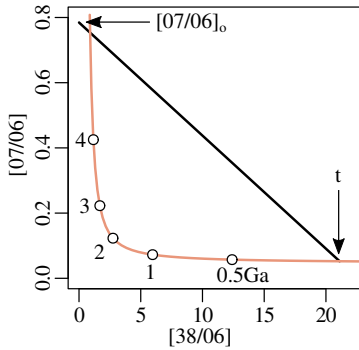


Figure 15.5: The semitotal-U/Pb isochron is a binary mixture line between a non-radiogenic Pb component with $^{207}\text{Pb}/^{206}\text{Pb}$ ratio $\left[\frac{07}{06}\right]_o$ and a radiogenic $^{238}\text{U}/^{206}\text{Pb}$ ratio that marks a point on the concordia line corresponding to an age t .

2. formats 4–6: Total-U/Pb regression using $^{204}\text{Pb}/^{238}\text{U}$ and $^{235}\text{U}/^{238}\text{U}$ (Ludwig, 1998). Given n sets of three-dimensional isotopic ratio measurements this algorithm can be formulated as a system of two equations that describe two coupled mixing lines with two common Pb intercepts ($\left[\frac{04}{06}\right]_o$ and $\left[\frac{04}{07}\right]_o$) and a single concordia intercept age t :

$$\left[\frac{04}{06}\right]_i = \left[\frac{04}{06}\right]_o \left\{ 1 - \left[\frac{38}{06}\right]_i (\exp[\lambda_{238}t] - 1) \right\} \quad (15.9)$$

$$\left[\frac{04}{07}\right]_i = \left[\frac{04}{07}\right]_o \left\{ 1 - \left[\frac{35}{07}\right]_i (\exp[\lambda_{235}t] - 1) \right\} \quad (15.10)$$

¹the same calculation can also be carried out in Wetherill space but is omitted here for brevity.

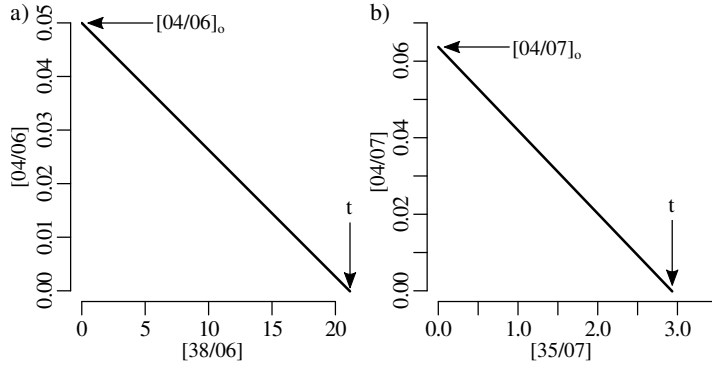


Figure 15.6: The total-U/Pb isochron is a binary mixture line between a non-radiogenic Pb component with $^{204}\text{Pb}/^{206}\text{Pb}$ and $^{204}\text{Pb}/^{207}\text{Pb}$ ratios $[04/06]_o$ and $[04/07]_o$, and radiogenic $^{238}\text{U}/^{206}\text{Pb}$ and $^{235}\text{U}/^{207}\text{Pb}$ ratios that mark a point on the concordia line corresponding to an age t . a) shows Equation 15.9, b) shows Equation 15.10.

3. formats 7 and 8: Total-U-Th/Pb regression using $^{206}\text{Pb}/^{238}\text{Pb}$, ^{232}Th and ^{235}U (Vermeesch, 2021). If ^{204}Pb cannot be measured precisely enough, then we can use ^{208}Pb as a proxy for common Pb, after correction for the radiogenic contribution from ^{232}Th :

$$\left[\frac{08}{06} \right]_i - \left[\frac{32}{38} \right]_i \left[\frac{38}{06} \right]_i (\exp[\lambda_{232}t] - 1) = \left[\frac{08}{06} \right]_o \left\{ 1 - \left[\frac{38}{06} \right]_i (\exp[\lambda_{238}t] - 1) \right\} \quad (15.11)$$

$$\left[\frac{08}{07} \right]_i - \left[\frac{32}{38} \right]_i \left[\frac{38}{07} \right]_i (\exp[\lambda_{232}t] - 1) = \left[\frac{08}{07} \right]_o \left\{ 1 - \left[\frac{35}{07} \right]_i (\exp[\lambda_{235}t] - 1) \right\} \quad (15.12)$$

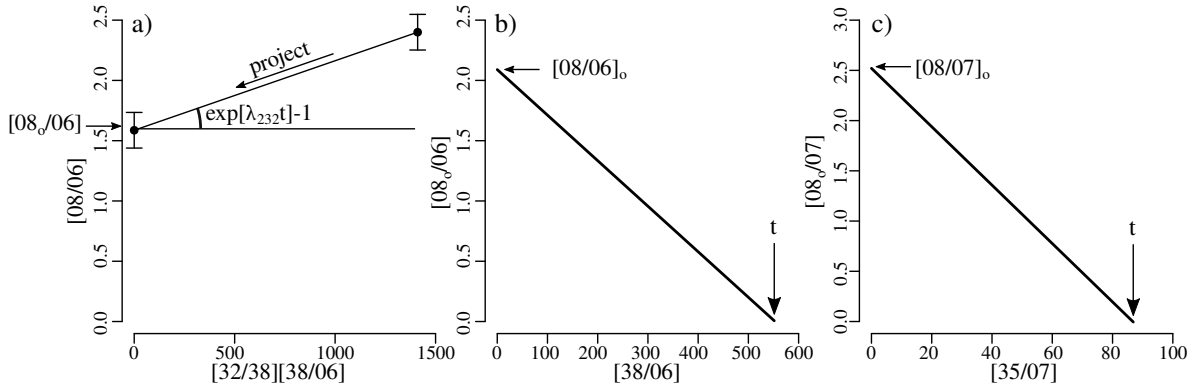


Figure 15.7: The total-U-Th/Pb isochron is constructed in a similar way to the total-U/Pb isochron of Figure 15.6, but using the non-radiogenic ^{208}Pb component instead of ^{204}Pb . The first step in the calculation algorithm (panel a, left hand side of Equation 15.11) is the removal of the radiogenic ^{208}Pb component for each aliquot in the dataset. This is achieved by projecting the $^{208}\text{Pb}/^{206}\text{Pb}$ ratio onto the $^{208}\text{Pb}/^{206}\text{Pb}$ -axis along a line whose slope is given by the ^{232}Th - ^{208}Pb ingrowth equation. The algorithm then iterates over the parameters $[08/06]_o$, $[08/07]_o$ and t until convergence is reached. Panel b) shows Equation 15.11, whereas panel c) shows Equation 15.12.

The parameterisation of these three discordia regression algorithms implies that the discordance is caused by common Pb. However, the results can also be used to interpret different scenarios such as Pb-loss and mixing of different aged growth zones. These mechanisms produce mixing lines between two concordant compositions on the concordia line. These intercepts can be visualised using *IsoplotR*'s Wetherill concordia function:

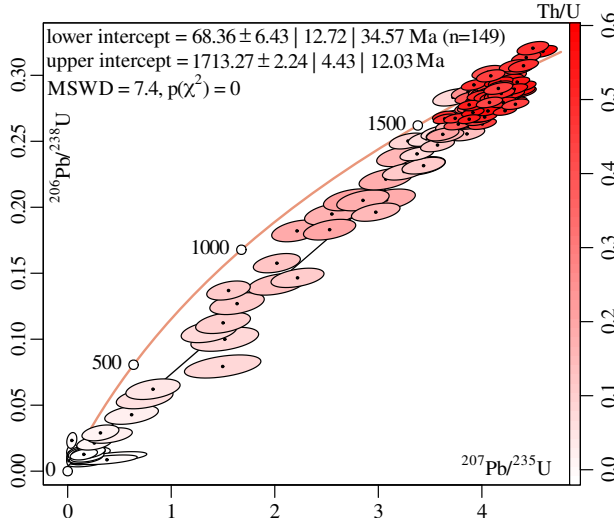


Figure 15.8: Wetherill concordia diagram of a depth-drilling experiments for a cycle-by-cycle LA-ICP-MS depth drilling experiment by Jeremy Hourigan (UC Santa Cruz). As the laser drills through the grain, it exposes different mixtures between two compositional end members with distinct Th/U ratios as shown by the colour scale. *IsoplotR* fits the mixing line by semitotal-U/Pb regression (Equation 15.8), the results are subsequently used to infer the upper intercept as well as the lower intercept with the concordia line.

15.4 Common Pb

There are a number of different strategies to remove the non-radiogenic Pb component from U–(Th)–Pb measurements. Which of these is most appropriate depends on the data format and geological setting:

1. In igneous and ortho-metamorphic rocks, where one can safely assume that all the aliquots are cogenetic and share the same common Pb composition, isochron regression is the most reliable method.
 - (a) The common Pb composition as well as the concordia intercept age can be obtained using the methods reviewed in Section 15.3.

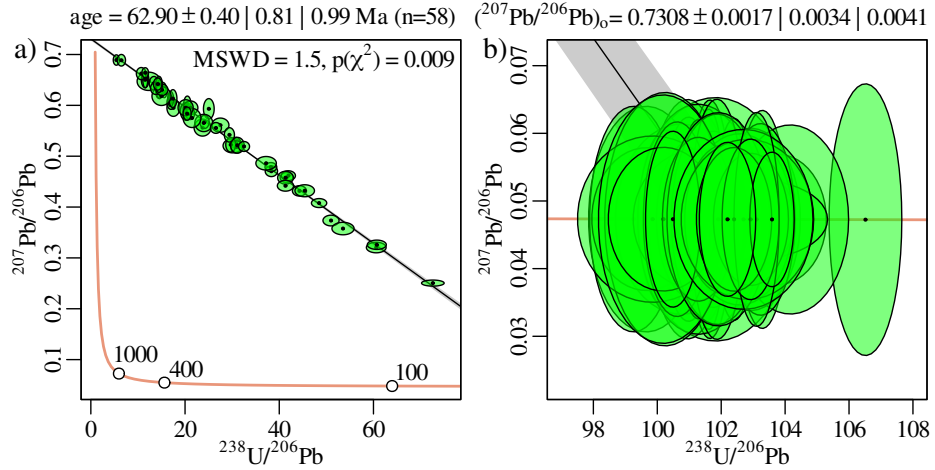


Figure 15.9: For LA-ICP-MS data stored in formats 1–3, the isochron regression is done by semitotal-U/Pb regression (a). Projecting the data onto the concordia line (b) produces common-Pb corrected U–Pb compositions that are perfectly concordant by definition. The legend applies to both panels.

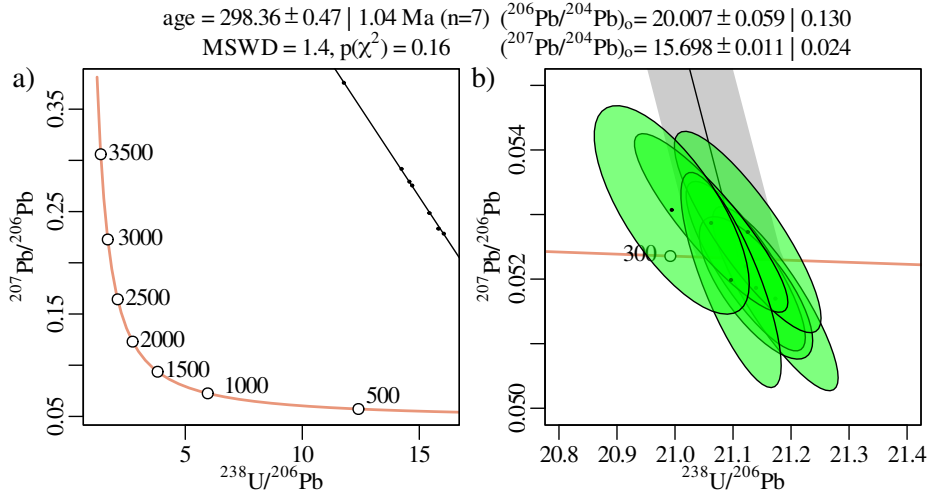


Figure 15.10: For SIMS or TIMS data (note the small error ellipses) stored in formats 4–6, the isochron regression is done by total-U/Pb regression (a). Projecting the data along this 3-dimensional isochron line produces common-Pb corrected compositions that do not plot exactly on the concordia line. The legend applies to both panels.

- (b) Alternatively, a nominal common Pb correction can be made by analysing a cogenetic mineral (such as feldspar) that is poor in U, and using its Pb composition as an ‘anchor’ for a constrained discordia regression.

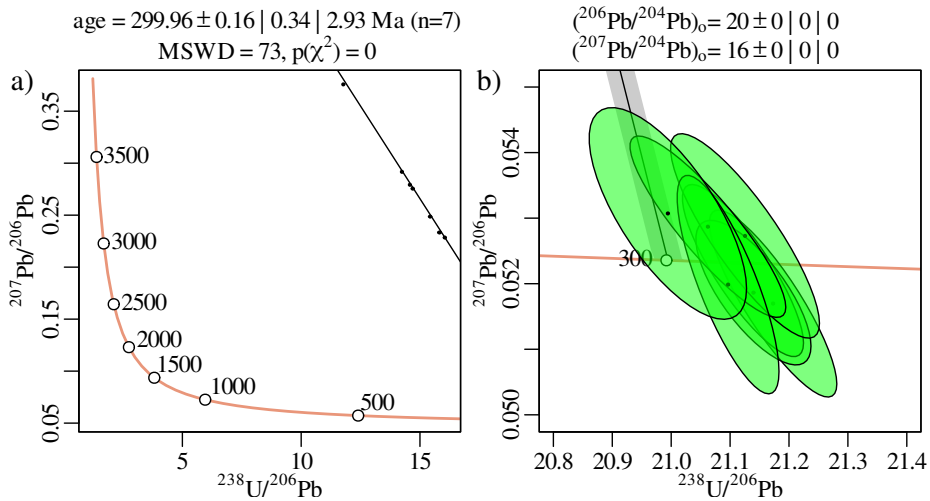


Figure 15.11: Common-Pb correction of the same data as Figure 15.9, but using an isochron that is anchored at a nominal common Pb composition of $^{206}\text{Pb}/^{204}\text{Pb} = 20$ and $^{207}\text{Pb}/^{204}\text{Pb} = 16$ (note the zero uncertainties in the legend). In this example, this procedure is less accurate (intentionally, for the sake of illustration) than the unconstrained regression of Figure 15.9.

2. In sedimentary and para-metamorphic rocks, in which the grains cannot safely be assumed to be cogenetic, each aliquot must be treated separately.

- (a) If there is some independent evidence to support a shared common-Pb composition for

all the aliquots, then the radiogenic composition can be obtained by two-point isochron regression between that common-Pb composition and each aliquot.

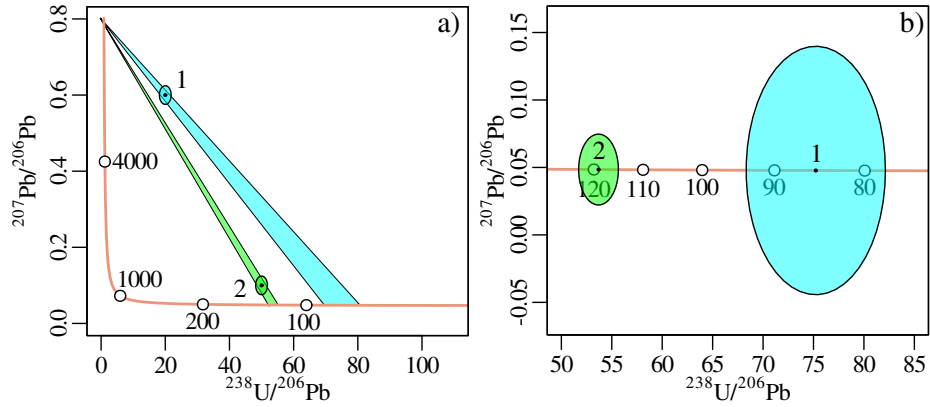


Figure 15.12: Common-Pb correction of two LA-ICP-MS based detrital measurements (formats 1–3) using the same nominal common Pb composition with $^{206}\text{Pb}/^{206}\text{Pb} = 0.8$. Each aliquot forms its own mixing line, and its uncertainties are magnified by the extrapolation, in proportion to its distance to the concordia line. This is different from the joint isochron regression of Figures 15.9 and 15.11, in which all aliquots are projected parallel to a joint regression line and the uncertainties are only mildly affected by the extrapolation.

- (b) In the absence of external evidence about the common Pb composition, one can infer the composition from the age using a mantle evolution model (e.g., Stacey and Kramers, 1975). If $t < 3.7$ Ga:

$$\left[\frac{^{206}\text{Pb}}{^{204}\text{Pb}} \right]_o = 11.152 + 9.74 (\exp[\lambda_{238}3.7] - \exp[\lambda_{238}t]) \quad (15.13)$$

$$\left[\frac{^{207}\text{Pb}}{^{204}\text{Pb}} \right]_o = 12.998 + 0.0707 (\exp[\lambda_{235}3.7] - \exp[\lambda_{235}t]) \quad (15.14)$$

$$\left[\frac{^{208}\text{Pb}}{^{204}\text{Pb}} \right]_o = 31.23 + 36.84 (\exp[\lambda_{232}3.7] - \exp[\lambda_{232}t]) \quad (15.15)$$

Each value of t represents a mixing line between a point on the concordia line and a point on the common-Pb intercept of the concordia diagram. Using the method of maximum likelihood, `IsoplotR` finds the mixing line that is closest to the each U–Pb measurement in a detrital dataset. For formats 1–3, it is generally possible to find an exact solution to this problem (i.e., the mixing line goes directly through the measurement). For formats 4–7, the problem is overconstrained and the fit is generally not perfect.

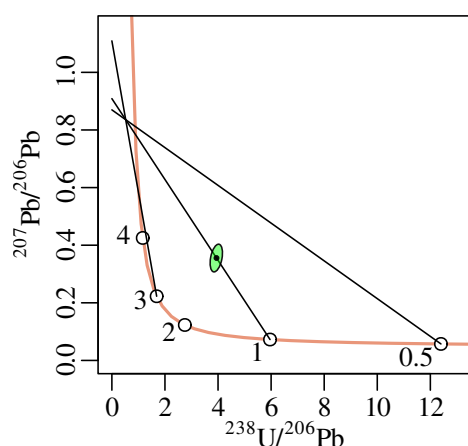


Figure 15.13: Three mixing lines between the radiogenic composition of 0.5, 1 and 3 Ga samples and the inferred Pb-composition of the mantle reservoir (according to Stacey and Kramers, 1975) from which these samples were hypothetically extracted. The y-intercepts correspond to $^{207}\text{Pb}/^{206}\text{Pb}$ ratios of 0.87, 0.91 and 1.11, respectively. For the error ellipse shown on this diagram, the mixing line at $t = 1$ Ga best describes the composition of the sample. Hence, the common-Pb corrected age of this analysis is 1 Ga.

15.5 Initial disequilibrium

Even though the U–Pb decay systems consist of numerous steps (14 for ^{238}U and 11 for ^{235}U), this complexity is ignored in conventional U–Pb geochronology and the method is mathematically treated as a simple parent-daughter pair. Section 2.4 showed that this assumption is justified once a state of secular equilibrium is established between all the intermediate daughter products in the decay chains. Such secular equilibrium automatically emerges after 1 to 2 million years. Any disequilibrium that might exist prior to this can be used as a chronometer in its own right, as discussed in Section 8.

Initial disequilibrium of the uranium decay series also affects the accuracy of the U–Pb method. For example, ignoring any initial excess ^{234}U would result in an overestimated $^{206}\text{Pb}/^{238}\text{U}$ age, and any initial ^{231}Pa deficit would result in an underestimated $^{207}\text{Pb}/^{235}\text{U}$ age. Thus initial disequilibrium is one mechanism to produce discordant results. The effect of initial disequilibrium is relatively small in most studies. It can be neglected in many geological applications, and is usually only a question of concern in high precision geochronology.

However in U–Pb geochronology of young carbonates, the effect of initial disequilibrium can be very significant, and may potentially result in order-of-magnitude levels of bias. *IsoplotR* offers three different strategies to deal with this bias:

1. If the intermediate daughter is sufficiently long lived, and the sample is sufficiently young to retain some of its disequilibrium, then the activity ratios can be back-calculated to the time of isotopic closure. This strategy applies to $^{234}\text{U}/^{238}\text{U}$ disequilibrium and, for very young samples, to $^{230}\text{Th}/^{234}\text{U}$ disequilibrium.
2. For older samples and shorter lived intermediate daughters such as ^{226}Ra ($t_{1/2} = 1599$ yr), secular equilibrium has usually been re-established and the initial activity ratio must be assumed.
3. However in the case of $^{230}\text{Th}/^{238}\text{U}$ disequilibrium in igneous rocks, the initial activity ratio can also be inferred from the $^{232}\text{Th}/^{238}\text{U}$ ratio of the bulk host rocks. In this case we make the assumption that the bulk rock is representative for the starting material from which the datable mineral formed. Due to the chemical similarity between Th and Pa, the same procedure can be applied to $^{231}\text{Pa}/^{238}\text{U}$ disequilibrium as well.

IsoplotR solves the complex evolution of the decay series using a matrix exponential approach developed by McLean, Bowring, and Gehrels (2016). To illustrate the principles behind this approach, describe the ^{238}U – ^{206}Pb decay chain in matrix form:

$$\frac{\partial}{\partial t} \begin{bmatrix} n_{38} \\ n_{34} \\ n_{30} \\ n_{26} \\ n_{06} \end{bmatrix} = \begin{bmatrix} -\lambda_{38} & 0 & 0 & 0 & 0 & 0 \\ \lambda_{38} & -\lambda_{34} & 0 & 0 & 0 & 0 \\ 0 & \lambda_{38} & -\lambda_{34} & 0 & 0 & 0 \\ 0 & 0 & \lambda_{34} & -\lambda_{30} & 0 & 0 \\ 0 & 0 & 0 & \lambda_{30} & -\lambda_{26} & 0 \\ 0 & 0 & 0 & 0 & \lambda_{26} & -\lambda_{26} \\ 0 & 0 & 0 & 0 & 0 & \lambda_{26} \end{bmatrix} \begin{bmatrix} n_{38} \\ n_{34} \\ n_{30} \\ n_{26} \\ n_{06} \end{bmatrix} \quad (15.16)$$

where n_{**} and λ_{**} stand for “the number of atoms and decay constant of nuclide 2**”. Equation 15.16 is the matrix equivalent of the system of equations that is represented in a simplified form by Equations 2.9–2.11. Just like the ordinary decay equation is solved by an exponential function (Equation 2.12), so the matrix decay equation is solved by a matrix exponential:

$$\begin{bmatrix} n_{38} \\ n_{34} \\ n_{30} \\ n_{26} \\ n_{06} \end{bmatrix} = \text{expm} \left(\begin{bmatrix} -\lambda_{38} & 0 & 0 & 0 & 0 & 0 \\ \lambda_{38} & -\lambda_{34} & 0 & 0 & 0 & 0 \\ 0 & \lambda_{38} & -\lambda_{34} & 0 & 0 & 0 \\ 0 & 0 & \lambda_{34} & -\lambda_{30} & 0 & 0 \\ 0 & 0 & 0 & \lambda_{30} & -\lambda_{26} & 0 \\ 0 & 0 & 0 & 0 & \lambda_{26} & -\lambda_{26} \\ 0 & 0 & 0 & 0 & 0 & \lambda_{26} \end{bmatrix} t \right) \begin{bmatrix} n_{38} \\ n_{34} \\ n_{30} \\ n_{26} \\ n_{06} \end{bmatrix}_0 \quad (15.17)$$

which expresses the present day amounts as a function of the initial amounts. Conversely, the equation can also be turned around to express the initial amounts as a function of the present day amounts:

$$\begin{bmatrix} n_{38} \\ n_{34} \\ n_{30} \\ n_{26} \\ n_{06} \end{bmatrix}_0 = \text{expm} \left(- \begin{bmatrix} -\lambda_{38} & 0 & 0 & 0 & 0 & 0 \\ \lambda_{38} & -\lambda_{34} & 0 & 0 & 0 & 0 \\ 0 & \lambda_{38} & -\lambda_{34} & 0 & 0 & 0 \\ 0 & 0 & \lambda_{34} & -\lambda_{30} & 0 & 0 \\ 0 & 0 & 0 & \lambda_{30} & -\lambda_{26} & 0 \\ 0 & 0 & 0 & 0 & \lambda_{26} & -\lambda_{26} \\ 0 & 0 & 0 & 0 & 0 & \lambda_{26} \end{bmatrix} t \right) \begin{bmatrix} n_{38} \\ n_{34} \\ n_{30} \\ n_{26} \\ n_{06} \end{bmatrix} \quad (15.18)$$

The matrix exponential approach provides an elegant solution for all three scenarios described above. Equation 15.17 can be used to construct a concordia diagram in the presence of disequilibrium:

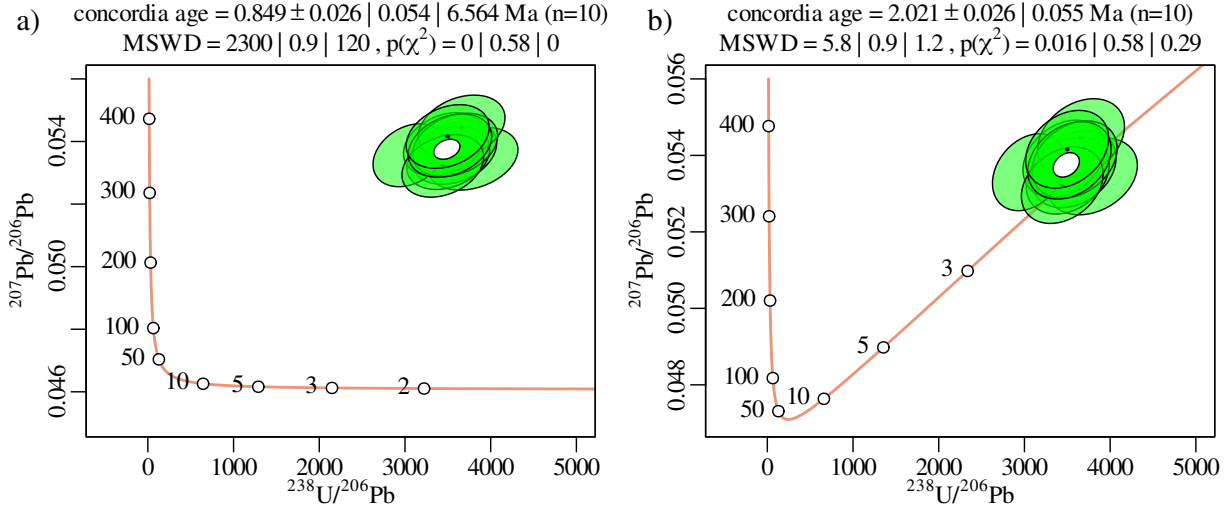


Figure 15.14: Tera-Wasserburg concordia diagram a) assuming secular equilibrium and b) accounting for secular disequilibrium with initial activity ratios of $^{234}\text{U}/^{238}\text{U} = 0$, $^{230}\text{Th}/^{238}\text{U} = 2$, $^{226}\text{Ra}/^{238}\text{U} = 2$ and $^{231}\text{Pa}/^{235}\text{U} = 2$. These initial conditions cause the concordia line to curve upwards for young ages. Without the disequilibrium correction, the concordia age would be wrong by over 100%.

15.6 Discordance filters

In detrital geochronology it is generally not possible to compute multi-grain concordia ages and isochrons. In fact, each grain in a detrital dataset has its own age and it is the entire distribution of their values that carries scientific value. The question then arises which method should be used to constrain the age distribution. *IsoplotR* offers a number of options:

1. use the $^{206}\text{Pb}/^{238}\text{U}$ date (t_{68}).
2. use the $^{207}\text{Pb}/^{235}\text{U}$ date (t_{75}). Given that the half-life of ^{235}U is more than six times shorter than that of ^{238}U , and that ^{235}U is more than 100 times less abundant than ^{238}U , little ^{207}Pb has been produced during the last billion years of Earth history compared to ^{206}Pb . Consequently, the $^{207}\text{Pb}/^{235}\text{U}$ method is less precise than the $^{206}\text{Pb}/^{238}\text{U}$ method during the Phanerozoic and Neoproterozoic, but more precise prior to that.
3. use the $^{207}\text{Pb}/^{206}\text{Pb}$ date (t_{76}). Like the $^{207}\text{Pb}/^{235}\text{U}$, also the $^{207}\text{Pb}/^{206}\text{Pb}$ method is more precise than the $^{206}\text{Pb}/^{238}\text{U}$ method for old grains, and less precise for young ones. The gradual shift in sensitivity between the $^{206}\text{Pb}/^{238}\text{U}$ and $^{207}\text{Pb}/^{206}\text{Pb}$ methods is visible in the slope of a Tera-Wasserburg concordia line, which is steep at old ages (high $^{207}\text{Pb}/^{206}\text{Pb}$ gradient w.r.t. time) and shallow at young ages (low $^{238}\text{U}/^{206}\text{Pb}$ gradient w.r.t. time).
4. switch from $^{206}\text{Pb}/^{238}\text{U}$ to $^{207}\text{Pb}/^{206}\text{Pb}$ at some point during the Proterozoic. This ensures good precision for all grains but introduces two practical issues. First, it requires the selection of a discrete discordance cutoff between the two methods. Second, the sudden switch between the $^{206}\text{Pb}/^{238}\text{U}$ and $^{207}\text{Pb}/^{206}\text{Pb}$ clocks may be marked by a discrete step in the age spectrum. This step is entirely artificial and obscures any geologically significant events that might occur around the same time.
5. use the single grain concordia date (t_c), which is calculated by applying Equation 15.5 or 15.6 separately to each grain. This approach avoids the need to switch between different methods, and offers superior precision to any of the other methods across the entire geologic time scale.

Once a chronometer has been chosen, it is advisable to ‘filter’ the data before plotting them as a KDE or CAD, so as to remove the most discordant analyses. It may be so that the common Pb correction of Section 15.4 removes much (or all, in the case of formats 1–3) discordance. But accuracy of single-grain common Pb corrections decreases quickly with increasing distance from the concordia line. For example, in Figure 15.12, aliquot 1 should probably not be used to constrain the age distribution. *IsoplotR* offers six different definitions of discordance that can be used to filter U–Pb data:

1. The relative age discordance:

$$d_r = 1 - t_{68}/t_{76} \quad (15.19)$$

This is the most widely used criterion today. It is more likely to remove young grains than old ones, and strongly skews the age distribution towards old age components as a result.

2. The absolute age discordance:

$$d_t = t_{76} - t_{68} \quad (15.20)$$

This definition is not very widely used. But it illustrates the dramatic effect that the discordance definition can have on the filtered age distributions. Compared with the relative age filter, it is more likely to reject old grains, and less likely to reject young ones. It even allows physically impossible negative $^{207}\text{Pb}/^{206}\text{Pb}$ ages to pass through it.

3. The p-value based discordance filter:

$$d_p = \text{Prob}(s > S_c | S_c \sim \chi^2_2) \quad (15.21)$$

where S_c is defined in Equation 15.5/15.6. d_p may have intuitive appeal as an ‘objective’ definition. But it has an undesirable negative effect on the precision and accuracy of the filtered results. This is because the p-value definition affects grains differently depending on their analytical precision.

For example, consider a 1.5 Ga zircon that is $d_r = 1\%$ discordant. If this grain were analysed by LA-ICP-MS with an analytical precision of 2%, say, then it would pass the chi-square test and be accepted as being concordant. However, if that same grain were analysed by TIMS with a precision of 0.2%, then the p-value criterion would reject it as being discordant. It seems fundamentally wrong that an imprecise analytical method would be favoured over a precise one. This is a pertinent problem because technical innovations are increasing the precision of all analytical approaches to U–Pb geochronology. As precision improves, so does the ability to detect ever small degrees of discordance. Using the p-value criterion, there may come a time when no zircon passes this filter. Hence it is best not to use this filter, but *IsoplotR* offers it nonetheless for the sake of completeness and to allow reproducing published results.

4. The Stacey-Kramers discordance filter

$$d_{sk} = 1 - r_{86}/r_{86}^* \quad (15.22)$$

where r_{86} and r_{86}^* are the $^{238}\text{U}/^{206}\text{Pb}$ ratios before and after common Pb correction, assumes that discordance is solely caused by common Pb contamination. If this assumption is correct, then the d_{sk} filter will produce the most accurate age distributions, provided that a Stacey and Kramers (1975) common Pb correction is applied to the filtered data afterwards.

5. The perpendicular Aitchison distance

$$d_a = dx(t_{68}) \sin \left(\arctan \left[\frac{dy(t_{76})}{dx(t_{68})} \right] \right) \quad (15.23)$$

represents the logarithmic distance from the measurement to the concordia line in log-log space (Vermeesch, 2021). $dx(*)$ and $dy(*)$ are the horizontal and vertical component of this distance. d_a produces a parallel acceptance zone around the (log-transformed) concordia line. This filter is most likely to reject ‘middle aged’ zircon grains, between 1000 and 2000 Ma, where the age resolving power of the U–Pb method is greatest. Above and below this interval, the d_a criterion is more forgiving. This behaviour is desirable because natural samples tend to exhibit more age discordance below 1000 Ma and above 2000 Ma than between these dates.

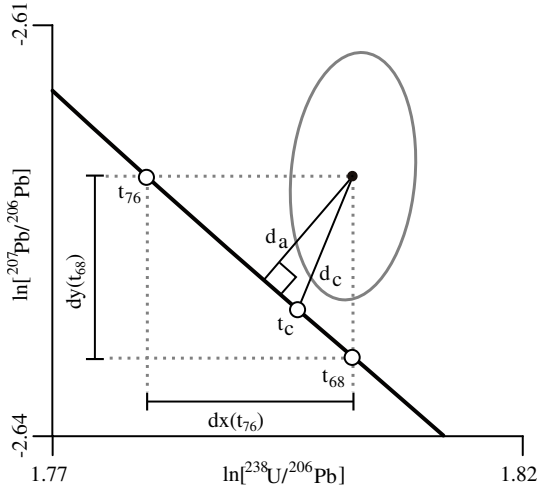


Figure 15.15: Illustration of the two logratio distance definitions of discordance. d_a is the perpendicular Aitchison distance from the measured logratio to the concordia line. d_c is the Aitchison distance measured along a line connecting the measured value and the concordia composition.

6. The concordia distance

$$d_c = \text{sgn}[t_{76} - t_{68}] \sqrt{dx(t_c)^2 + dy(t_c)^2} \quad (15.24)$$

is a modified version of the d_a criterion that takes into account the uncertainties of the U–Pb isotopic composition. It represents the distance (in log-log space) from the measurement to the U–Pb composition of the concordia age. Its effects on the U–Pb age distributions are more difficult to visualise but are similar to those of the d_a criterion. Empirical evidence suggests that this filter is optimal in the sense that it has a minimal effect on the shape of the age distribution: it results in a tightening of subpopulations without changing their position or relative size (Vermeesch, 2020).

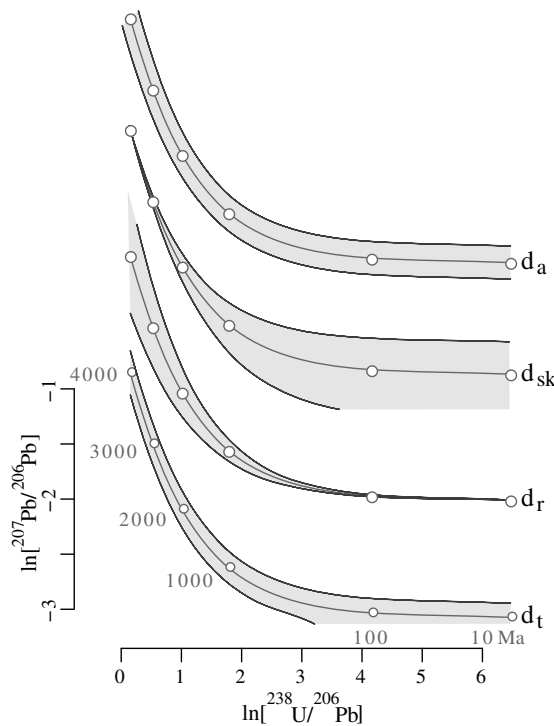


Figure 15.16: Discordance cutoffs for four of the six discordance definitions. The d_p and d_c criteria are not shown because they depend on the analytical uncertainty of the measurements, which may vary between studies. The grey envelopes mark cutoff values of $d_r = 20\%$ (relative age filter), $d_t = 300$ Ma (absolute age filter), $d_{sk} = 2\%$ (Stacey–Kramers filter) and $d_a = 15\%$ (perpendicular Aitchison distance) on a Tera–Wasserburg concordia diagram, which is plotted in logarithmic space to provide a more balanced view of the old and young ends of the time scale. The d_{sk} and d_t envelopes are truncated where they cross over into physically impossible negative isotope ratio space.

References

- Janots, E. and D. Rubatto (2014). “U–Th–Pb dating of collision in the external Alpine domains (Urseren zone, Switzerland) using low temperature allanite and monazite”. In: *Lithos* 184, pp. 155–166.
- Ludwig, K. R. (1998). “On the treatment of concordant uranium–lead ages”. In: *Geochimica et Cosmochimica Acta* 62, pp. 665–676. DOI: 10.1016/S0016-7037(98)00059-3.
- McLean, N. M., J. F. Bowring, and G. Gehrels (2016). “Algorithms and software for U–Pb geochronology by LA–ICPMS”. In: *Geochemistry, Geophysics, Geosystems* 17.7, pp. 2480–2496.
- Stacey, J. and J. Kramers (1975). “Approximation of terrestrial lead isotope evolution by a two-stage model”. In: *Earth and Planetary Science Letters* 26.2, pp. 207–221.
- Vermeesch, P. (2020). “Unifying the U–Pb and Th–Pb methods: joint isochron regression and common Pb correction”. In: *Geochronology* 2.1, pp. 119–131.
- (2021). “On the treatment of discordant detrital zircon U–Pb data”. In: *Geochronology* 3, pp. 1–11. DOI: 10.5194/gchron-3-1-2021.

Chapter 16

Pb–Pb and Th–Pb

The Pb–Pb and Th–Pb methods are extensions of the U–Pb method that do not require measuring uranium. Although Chapter 15 did discuss $^{207}\text{Pb}/^{206}\text{Pb}$ ages and the U–Th–Pb concordia diagram and isochron, the applications of $^{207}\text{Pb}/^{206}\text{Pb}$ and $^{208}\text{Pb}/^{232}\text{Th}$ discussed in this chapter are sufficiently different to warrant separate discussion. The Pb–Pb method applies the full ^{204}Pb – ^{206}Pb – ^{207}Pb composition of cogenetic minerals to construct isochrons. This method plays a fundamental role in unravelling the early history of the solar system, and has been used to date the formation of our planet. The Th–Pb method behaves very much like the Rb–Sr, Sm–Nd and other simple parent daughter chronometers, which will be discussed in more detail in Chapter 18.

16.1 Pb–Pb

Pb–Pb data can be supplied in three data formats:

1. ‘Normal’: $\frac{06}{04}$, $\text{err}[\frac{06}{04}]$, $\frac{07}{04}$, $\text{err}[\frac{07}{04}]$, $r[\frac{06}{04}, \frac{07}{04}]$
2. ‘Inverse’: $\frac{04}{06}$, $\text{err}[\frac{04}{06}]$, $\frac{07}{06}$, $\text{err}[\frac{07}{06}]$, $(r[\frac{04}{06}, \frac{07}{06}])$
3. ‘Three ratios’: $\frac{06}{04}$, $\text{err}[\frac{06}{04}]$, $\frac{07}{04}$, $\text{err}[\frac{07}{04}]$, $\frac{07}{06}$, $\text{err}[\frac{07}{06}]$

where format 3 can be converted to format 1 using Equation 15.2. Format 1 can be converted to format 2 using the following expression:

$$\begin{cases} x' = \frac{1}{x} \\ y' = \frac{x}{y} \\ \left(\frac{s[x']}{x'}\right)^2 = \left(\frac{s[x]}{x}\right)^2 \\ \left(\frac{s[y']}{y'}\right)^2 = \left(\frac{s[x]}{x}\right)^2 - 2\rho_{x,y} \left(\frac{s[x]}{x}\right) \left(\frac{s[y]}{y}\right) + \left(\frac{s[y]}{y}\right)^2 \\ \rho_{x'y'} = \left(\frac{x'}{s[x']}\right) \left[\left(\frac{y}{s[y]}\right) - \rho_{xy} \left(\frac{x}{s[x]}\right)\right] \end{cases} \quad (16.1)$$

where $x = [06/04]$ and $y = [07/04]$, $x' = [04/06]$ and $y' = [04/07]$. This transformation is perfectly symmetric in the sense that it can also be used to convert inverse isochron ratios to conventional ones, so that $x' = [06/04]$ and $y' = [07/04]$, $x = [04/06]$ and $y = [04/07]$.

16.2 (inverse) isochrons

The ‘normal’ and ‘inverse’ monikers for the first two Pb–Pb input formats refers to their use for isochron regression:

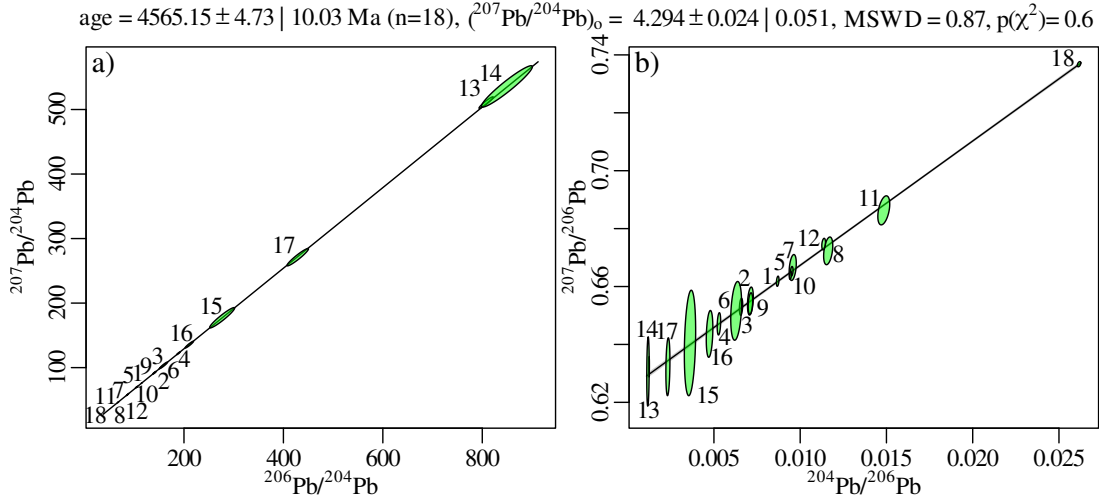


Figure 16.1: a) conventional and b) inverse isochron plot for a Pb–Pb dataset of carbonaceous chondrules, which date the oldest meteorites in the solar system. The aliquots are numbered to facilitate the comparison of the two plots. The most radiogenic aliquots plot in the upper right corner of the conventional isochron, and in the lower left corner of the inverse isochron diagram. The conventional isochron places the least abundant isotope in the denominator, ^{204}Pb , which caused strong error correlations for reasons that are explained in Section 13.5. These correlations are greatly reduced when the more abundant ^{206}Pb is used as a common denominator.

The Pb–Pb age is proportional to the slope of a conventional isochron, and to the y-intercept of the inverse isochron. Conversely, the $^{207}\text{Pb}/^{204}\text{Pb}$ -ratio of the common Pb is given by the y-intercept of the conventional isochron, and by the slope of the inverse isochron. Provided that the analytical uncertainties are reasonably small compared to the measured isotopic ratios ($< 5\%$, say), the age and common Pb composition are identical for both approaches.

16.3 The Stacey-Kramers growth curve

As previously discussed in Section 15.4 and quantified by Equations 15.13–15.15, the mantle evolution model of Stacey and Kramers (1975) describes the Pb composition of the mantle through geologic time. This model can be used for the common Pb correction of discordant samples, but can also be used to compute ‘model ages’ from Pb-rich mineral phases such as galena. It is also useful to compare whole rock Pb–Pb isochron ages with the mantle evolution model, in order to better understand the source of the source material from which the rock was derived. To facilitate this type of investigation, *IsoplotR* allows the Stacey and Kramers (1975) growth curve to be plotted alongside the isochron data, and estimates the intersection(s) between the isochron and the growth curve.

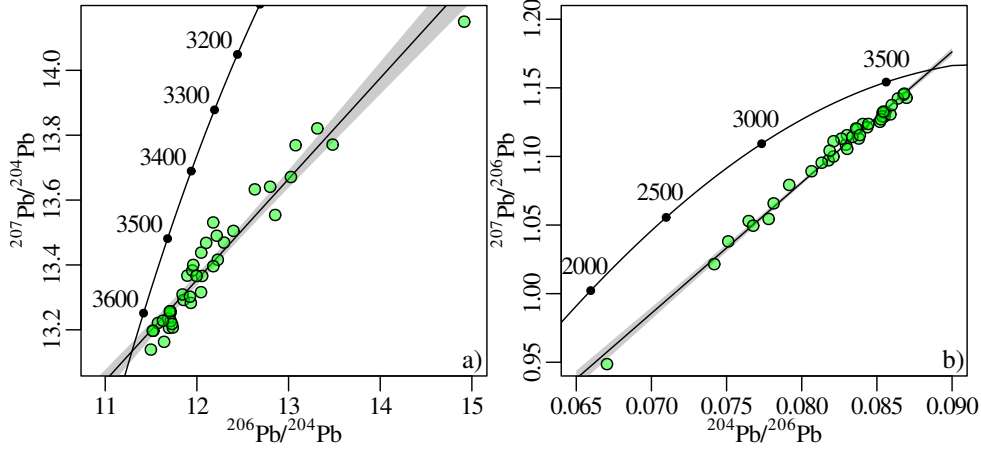


Figure 16.2: a) conventional and b) inverse model-2 whole rock Pb–Pb isochron of the Amitsoq gneiss (Greenland, Kamber and Moorbath, 1998), with the Stacey and Kramers (1975) growth curve shown on the left. The close agreement between the isochron age (3550 ± 130 Ma) and the model age (3650 Ma) suggest that the magmatic precursor of the Amitsoq orthogneiss was extracted from the mantle shortly before its formation.

16.4 Th–Pb

The Th–Pb method applies to minerals (such as allanite and monazite) that are rich in Th and relatively poor in U. `IsoplotR` accepts Th–Pb data in three formats that are similar to the Pb–Pb data formats:

1. ‘Normal’: $\frac{32}{04}$, $\text{err}[\frac{32}{04}]$, $\frac{08}{04}$, $\text{err}[\frac{08}{04}]$, $r[\frac{08}{04}, \frac{08}{04}]$
2. ‘Inverse’: $\frac{32}{08}$, $\text{err}[\frac{32}{08}]$, $\frac{04}{08}$, $\text{err}[\frac{04}{08}]$, $(r[\frac{32}{08}, \frac{04}{08}])$
3. ‘Three ratios’: $\frac{32}{08}$, $\text{err}[\frac{32}{08}]$, $\frac{04}{08}$, $\text{err}[\frac{04}{08}]$, $\frac{32}{08}$, $\text{err}[\frac{32}{08}]$, $\frac{32}{04}$, $\text{err}[\frac{32}{04}]$,

where format 3 can be converted to format 1 using Equation 15.2, and format 1 can be converted to format 2 (and vice versa) using Equation 16.1. As the names of the formats suggest, Th–Pb data can be used to form conventional and inverse isochrons, where the former place non-radiogenic ^{204}Pb in the denominator, and the latter radiogenic ^{208}Pb :

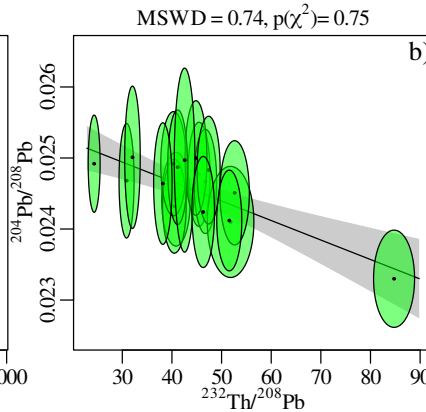
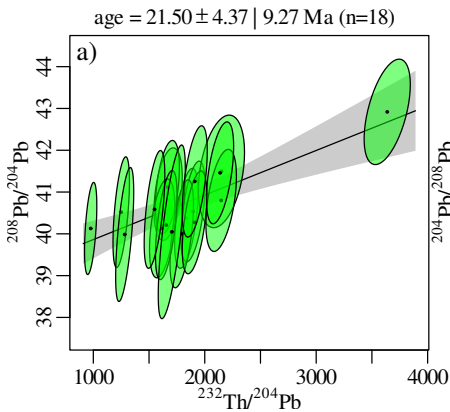


Figure 16.3: a) conventional and b) inverse model-1 isochron for the allanite Th–Pb data of Janots and Rubatto (2014). The age is proportional to the slope of the conventional isochron, and to the x-intercept of the inverse isochron. The common-Pb composition is given by the y-intercept.

16.5 Single grain ages

The Th–Pb method is usually applied to multiple aliquots from the same sample, for which the isochron method can retrieve both the age and the non-radiogenic Pb components. However it can also be useful to inspect the ages of each individual aliquot, using radial plots, KDEs and CADs. There are two ways to do this:

1. Treat the aliquots together by projecting the isotopic ratio data onto the x-axis of the inverse isochron plot.

$$\left[\frac{D}{P}\right]_i^* = \frac{b}{bx_i - y_i} \quad (16.2)$$

where $[D/P]_i^*$ is the radiogenic daughter-to-parent ratio of the i^{th} aliquot, x_i and y_i are the independent and dependent variable of the inverse isochron diagram, and b is its slope.

2. Apply a nominal correction to each aliquot independently, by two point isochron regression. For example, in conventional isochron space:

$$\left[\frac{D}{P}\right]_i^* = \frac{y_i - y_o}{x_i} \quad (16.3)$$

where y_o is the isotopic ratio of the inherited daughter component.

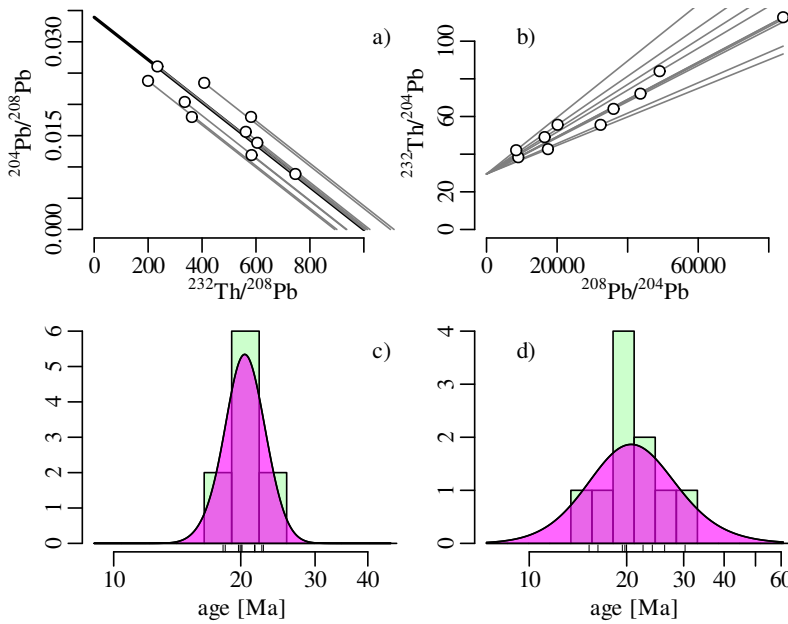


Figure 16.4: Single grain analysis of Th–Pb data by a) projecting each aliquot onto the x-axis of an inverse isochron, and b) individually correcting each aliquot by calculating the slope of a line that connects it to the common Pb composition on a conventional isochron diagram. The KDEs of the corresponding dates are shown in c) and d). The isochron-based approach yields less dispersed results.

References

- Janots, E. and D. Rubatto (2014). “U–Th–Pb dating of collision in the external Alpine domains (Urseren zone, Switzerland) using low temperature allanite and monazite”. In: *Lithos* 184, pp. 155–166.
- Kamber, B. S. and S. Moorbath (1998). “Initial Pb of the Amitsoq gneiss revisited: implication for the timing of early Archaean crustal evolution in West Greenland”. In: *Chemical Geology* 150.1-2, pp. 19–41.
- Stacey, J. and J. Kramers (1975). “Approximation of terrestrial lead isotope evolution by a two-stage model”. In: *Earth and Planetary Science Letters* 26.2, pp. 207–221.

Chapter 17

Ar–Ar and K–Ca

The Ar–Ar and K–Ca chronometers are based on the branched decay of ^{40}K to ^{40}Ar and ^{40}Ca . The Ar–Ar is a widely used method that has replaced the K–Ar method in all but a few applications (Section 6). The K–Ca method is a more recent development that has become feasible due to analytical advances in SIMS, which have resolved the isobaric interference between ^{40}K and ^{40}Ca . The original K–Ar method is not implemented in **IsoplotR** but may be added later.

17.1 Ar–Ar

IsoplotR offers three input formats for Ar–Ar data, which all require the user to provide the J factor and its standard error (Section 6.2), as well as the following columns of isotopic ratio data:

1. ‘Normal’: $\frac{40}{36}$, $\text{err}[\frac{40}{36}]$, $\frac{39}{36}$, $\text{err}[\frac{39}{36}]$, $r[\frac{40}{36}, \frac{39}{36}]$, (39)
2. ‘Inverse’: $\frac{39}{40}$, $\text{err}[\frac{39}{40}]$, $\frac{36}{40}$, $\text{err}[\frac{36}{40}]$, $(r[\frac{39}{40}, \frac{36}{40}])$, (39)
3. ‘Three ratios’: $\frac{39}{40}$, $\text{err}[\frac{39}{40}]$, $\frac{36}{40}$, $\text{err}[\frac{36}{40}]$, $\frac{39}{36}$, $\text{err}[\frac{39}{36}]$, (39)

where (39) stands for the amount of ^{39}Ar in each heating step, which is normalised to form the X-axis of an age spectrum (Section 17.2). Error correlations are much stronger for format 1 than for format 2 and are therefore compulsory for the former and optional for the latter. As for the Pb–Pb and Th–Pb methods, the names of the formats refer to the normal and inverse isochrons that they form. However, both normal and inverse isochrons are available for all three methods, because **IsoplotR** converts them in the background. It does so using Equation 15.2 for the conversion from format 3 to format 2; and using Equation 16.1 to convert format 2 to format 1 and vice versa.

Single grain ages can be calculated by projecting cogenetic aliquots along an isochron, or by applying a nominal ‘excess argon’ correction to each aliquot separately. The latter approach typically uses the atmospheric argon composition, which is characterised by a $^{40}\text{Ar}/^{39}\text{Ar}$ ratio of 298.56 ± 0.31 Lee et al. (2006). The resulting ages can then be visualised as radial plots, KDEs, or CADs:

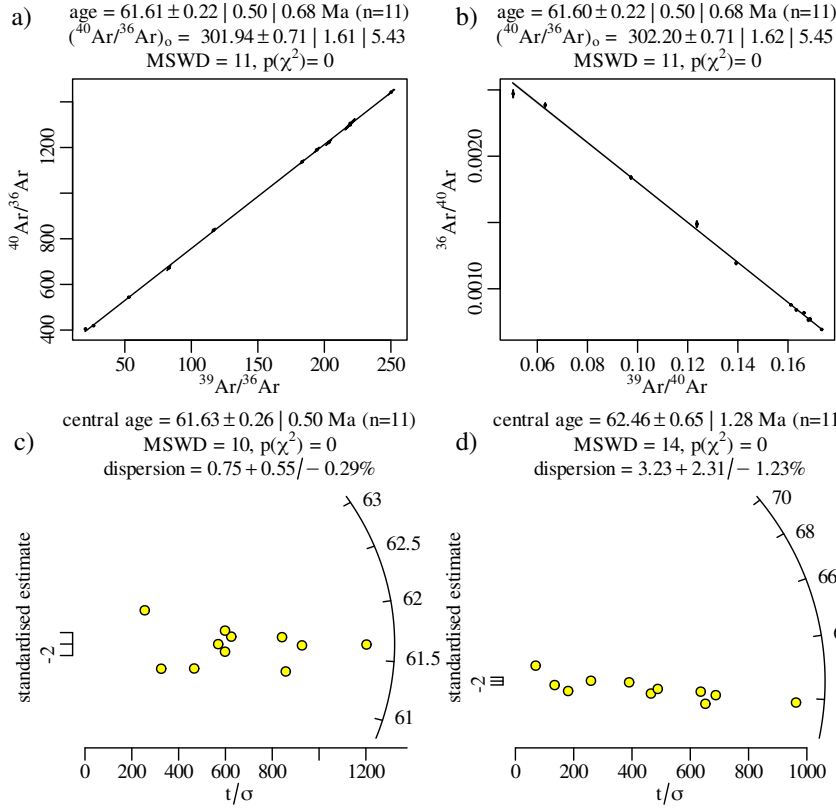


Figure 17.1: a) conventional and b) inverse model-1 isochron for Ar–Ar data. The non-radiogenic (‘excess’) argon is characterised by a $^{40}\text{Ar}/^{39}\text{Ar}$ ratio of 302, which is slightly higher than atmosphere. c) shows a radial plot of the excess-Ar-corrected ages obtained by projecting the aliquots along the inverse isochron (just like in Figure 16.4.a). d) using the atmospheric ratio of 298.56 ± 0.31 to correct each aliquot independently yields a slightly older and more dispersed distribution.

17.2 Age spectra

As explained in Section 6.2, the $^{40}\text{Ar}/^{39}\text{Ar}$ -age spectrum is a useful tool to visualise stepwise heating measurements. Its appearance is based on the weighted mean plot (e.g., Figure 13.5), with the different heating steps arranged in order of increasing degree of degassing along the horizontal axis, and the width of the different sample boxes proportional to the corresponding amounts of ^{39}Ar .

IsoplotR defines the ‘plateau age’ as the weighted mean age of the longest sequence (in terms of cumulative ^{39}Ar content) of consecutive heating steps that pass the modified Chauvenet criterion of Section 14. Note that this definition is different (and simpler) than the one used by Isoplot (Ludwig, 2003). However, it is important to mention that all definitions of an age plateau are heuristic by nature and should not be used for quantitative inference.

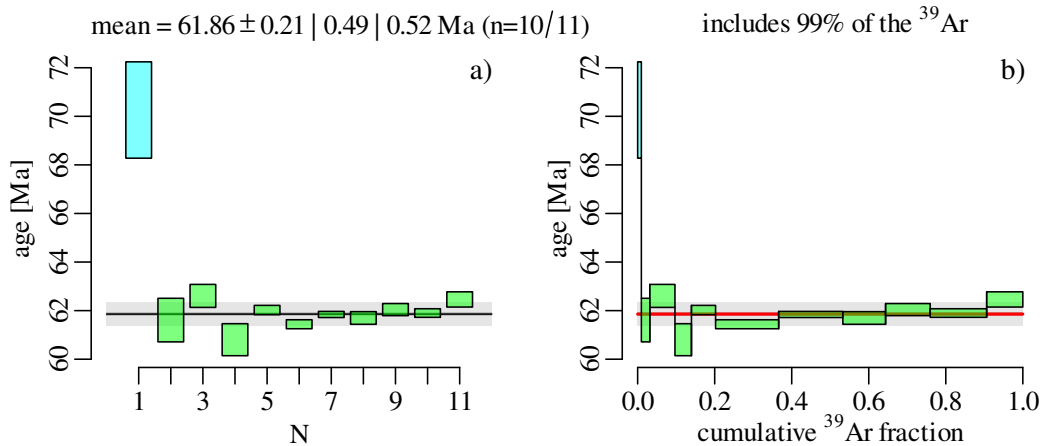


Figure 17.2: a) weighted mean and b) age spectrum for the Ar–Ar of Figure 17.1, using an atmospheric $^{40}\text{Ar}/^{39}\text{Ar}$ -ratio for the non-radiogenic component. The plateau is shown in green and the single outlier in blue. The weighted mean age was calculated using an ordinary weighted mean. In this case the weighted mean age and the plateau age are the same but this is not always the case.

17.3 K–Ca

IsoplotR offers three input formats for K–Ca data:

1. ‘Normal’: $\frac{^{40}\text{K}}{^{44}\text{Ca}}, \text{err}\left[\frac{^{40}\text{Ca}}{^{44}\text{Ca}}\right], \frac{^{40}\text{Ca}}{^{44}\text{Ca}}, \text{err}\left[\frac{^{40}\text{Ca}}{^{44}\text{Ca}}\right], r\left[\frac{^{40}\text{K}}{^{44}\text{Ca}}, \frac{^{40}\text{Ca}}{^{44}\text{Ca}}\right]$
2. ‘Inverse’: $\frac{^{40}\text{K}}{^{40}\text{Ca}}, \text{err}\left[\frac{^{40}\text{K}}{^{40}\text{Ca}}\right], \frac{^{44}\text{Ca}}{^{40}\text{Ca}}, \text{err}\left[\frac{^{40}\text{Ca}}{^{40}\text{Ca}}\right], r\left[\frac{^{40}\text{K}}{^{40}\text{Ca}}, \frac{^{44}\text{Ca}}{^{40}\text{Ca}}\right]$
3. ‘Three ratios’: $\frac{^{40}\text{K}}{^{40}\text{Ca}}, \text{err}\left[\frac{^{40}\text{K}}{^{40}\text{Ca}}\right], \frac{^{44}\text{Ca}}{^{40}\text{Ca}}, \text{err}\left[\frac{^{40}\text{Ca}}{^{40}\text{Ca}}\right], r\left[\frac{^{40}\text{K}}{^{40}\text{Ca}}, \frac{^{44}\text{Ca}}{^{40}\text{Ca}}\right], \frac{^{40}\text{K}}{^{40}\text{Ca}}, \text{err}\left[\frac{^{40}\text{K}}{^{40}\text{Ca}}\right]$

where, in contrast with previous formatting summaries, the full names of the nuclides are given because of the isobaric parent and daughter. It is precisely this isobary that prevented the K–Ca from being widely applied until recently. Formats 1, 2 and 3 can be converted to each other using Equations 15.2 and 16.1.

IsoplotR uses ^{44}Ca as a normalising isotope because it is the most abundant of calcium’s non-radiogenic isotopes, accounting for up to 2% of the isotopic budget. Using a less abundant isotope such as ^{42}Ca ($< 0.647\%$), ^{43}Ca ($< 0.135\%$), or ^{46}Ca ($< 0.004\%$), would only increase the error correlations in conventional isochron space (which are already very strong as shown in Figure 13.6). However, IsoplotR also offers inverse isochrons, which greatly reduce these correlations as explained in Section 13.5 and shown in Figure 13.7.

References

- Lee, J.-Y. et al. (2006). “A redetermination of the isotopic abundances of atmospheric Ar”. In: *Geochimica et Cosmochimica Acta* 70.17, pp. 4507–4512.
- Ludwig, K. R. (2003). “User’s manual for Isoplot 3.00: a geochronological toolkit for Microsoft Excel”. In: *Berkeley Geochronology Center Special Publication* 4 4.

Chapter 18

Rb–Sr, Sm–Nd, Lu–Hf and Re–Os

Rb–Sr, Sm–Nd, Lu–Hf and Re–Os all fall in the category of simple parent daughter chronometers, which are based on a single parent that decays to a single daughter without additional complications such as branched decay or secular equilibrium. These chronometers usually involve liquid chromatography and mass spectrometry by TIMS or solution ICP-MS. Data can be introduced into `IsoplotR` in three formats:

1. ‘Normal’: $\frac{P}{d}$, $\text{err}\left[\frac{P}{d}\right]$, $\frac{D}{d}$, $\text{err}\left[\frac{D}{d}\right]$, $r\left[\frac{P}{d}, \frac{D}{d}\right]$
2. ‘Inverse’: $\frac{P}{D}$, $\text{err}\left[\frac{P}{D}\right]$, $\frac{d}{D}$, $\text{err}\left[\frac{d}{D}\right]$, $r\left[\frac{P}{D}, \frac{d}{D}\right]$
3. ‘Concentrations’: **P**, $\text{err}[\mathbf{P}]$, **D**, $\text{err}[\mathbf{D}]$, **P/D**

where

P = ^{87}Rb , ^{147}Sm , ^{187}Re or ^{176}Lu .

D = ^{87}Sr , ^{143}Nd , ^{187}Os or ^{176}Hf .

d = ^{86}Sr , ^{144}Nd , ^{188}Os or ^{177}Hf .

P = the elemental concentration (in ppm) of Rb, Sm, Re, or Lu.

D = the elemental concentration (in ppm) of Sr, Nd, Os, or Hf.

Format 1 can be converted to format 2 (and vice versa) using Equation 16.1, whereas Format 3 can be converted to format 1 with the methods that were used in Chapter 10. For example, for Rb–Sr:

$$\left(^{87}\text{Rb}/^{86}\text{Sr}\right) = \frac{\mathbf{Rb}}{\mathbf{Sr}} \frac{M(\text{Rb})}{M(\text{Sr})} \frac{1 + \left[^{87}\text{Sr}/^{86}\text{Sr}\right] \left[1 + \left(^{84}\text{Sr}/^{87}\text{Sr}\right) + \left(^{88}\text{Sr}/^{87}\text{Sr}\right)\right]}{1 + \left[^{85}\text{Rb}/^{87}\text{Rb}\right]} \quad (18.1)$$

where $(^{84}\text{Sr}/^{87}\text{Sr})$, $(^{88}\text{Sr}/^{87}\text{Sr})$ and $(^{85}\text{Rb}/^{87}\text{Rb})$ are constant, non-radiogenic isotope ratios, and $M(\text{Rb})$ and $M(\text{Sr})$ are the molar masses of Rb and Sr, respectively. Because the measured $(^{87}\text{Sr}/^{86}\text{Sr})$ -ratio appears in Equation 18.1, the covariance between $(^{87}\text{Rb}/^{86}\text{Sr})$ and $(^{87}\text{Sr}/^{86}\text{Sr})$ is nonzero and can be estimated using Equation 9.9 or 9.10.

The parent daughter pairs method are generally used by multi-aliquot isochrons that can either be plotted in conventional or inverse isochron space. In contrast with the U–Pb, Ar–Ar, Pb–Pb and K–Ca method, in which the nonradiogenic daughter isotope is less abundant than the radiogenic isotope, this is not the case for the Rb–Sr, Sm–Nd, Re–Os and Lu–Hf methods. Their non-radiogenic isotopes (marked as ‘d’ above) tend to be more abundant than the radiogenic isotope and therefore they exhibit weaker error correlations in conventional isotope space. Nevertheless, `IsoplotR` does offer the inverse isochron as an option because it is may still be useful

to visualise the data as a simple mixing line between non-radiogenic and radiogenic components.

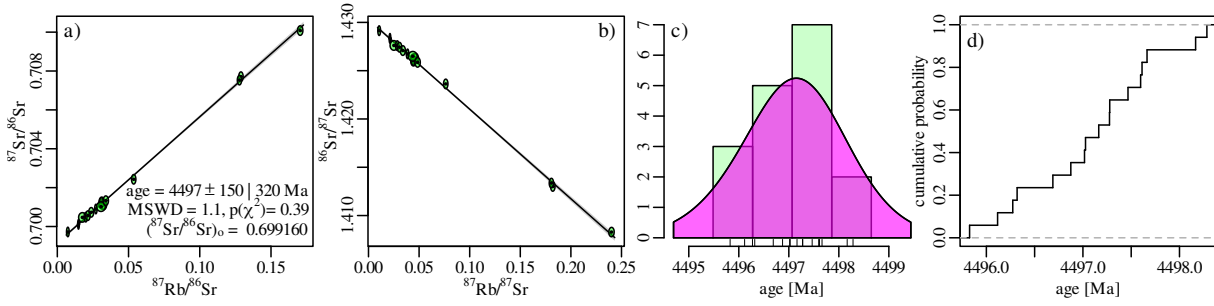


Figure 18.1: a) conventional and b) inverse Rb–Sr isochron, c) KDE and d) CAD of the single aliquot age estimates using the isochron intercept as a non-radiogenic $^{87}\text{Sr}/^{86}\text{Sr}$ ratio.

The distribution of the data around the best fit isochron can be visually assessed on radial plots, KDEs and CADs. This is achieved by projecting the data along parallel lines to the best fit in inverse isochron space. Alternatively, the assumption of cogenetic origin may be relaxed by fixing the non-radiogenic composition and computing two-point isochrons between this composition and the measured ratios for each aliquot.

Chapter 19

U–Th–(Sm)–He

IsoplotR offers a single input format for U–Th–(Sm)–He data, which constitutes a simple table with the following columns:

$$\text{He, err[He], U, err[U], Th, err[Th], Sm, err[Sm]}$$

which contains all the necessary information to calculate the age. Rewriting Equation 7.1:

$$\begin{aligned} [^4\text{He}] &= a(t)[\text{U}] + b(t)[\text{Th}] + c(t)[\text{Sm}] \\ \text{where } a(t) &= \left[8 \frac{137.818}{138.818} (e^{\lambda_{238}t} - 1) + 7 \frac{1}{138.818} (e^{\lambda_{235}t} - 1) \right] \\ b(t) &= 6(e^{\lambda_{232}t} - 1) \\ \text{and } c(t) &= 0.1499(e^{\lambda_{147}t} - 1) \end{aligned} \quad (19.1)$$

Because Sm (1) produces only one α -particle per decay event; (2) has a very long half-life; and (3) its radioactive isotope 147 only accounts for 14.99% of total samarium, Sm can be ignored as a parent in all but the most Sm-rich samples. For this reason, some laboratories do not measure Sm at all, and the ‘Sm’ and ‘err[Sm]’ columns are optional. If omitted, IsoplotR will simply assume that the Sm-concentration is zero.

The He, U, Th (and Sm) measurements must be expressed in internally consistent **atomic units** such as mol, fmol, pmol, mol/cc, fmol/ μg etc. They must not be expressed in mass units such as ppm, ppb or wt%! For U and Sm, which are poly-isotopic elements, it is the total amount that is required, and not just ^{238}U and ^{147}Sm . A second important requirement is that the data have been corrected for **α -ejection** prior to analysis, as explained in the next section.

19.1 The α -ejection correction

Like argon, helium is a noble gas that is lost to the environment (and eventually to space) at high temperatures by volume diffusion. Additional complication is added by the physical separation of the parent and daughter nuclides in the U-Th-(Sm)-He system. This separation results from the energy released during α -decay, which displaces the α -particles by up to 16 μm and may result in the ejection of helium produced by parent atoms that are sited near the edges of the host mineral. That lost helium must be taken into account when interpreting the thermal history of a sample. For rapidly cooled samples, this can be done by applying a geometric correction to the U, Th and Sm-measurements. For a sphere:

$$F_T = 1 - \frac{3}{4} \frac{S}{R} + \frac{1}{16} \left[\frac{S}{R} \right]^3 \quad (19.2)$$

where F_T is the fraction of helium that is retained in the grain, r is the radius of a sphere with equivalent surface-to-volume ratio as the mineral habit of interest, and S is the α -stopping distance:

mineral	^{238}U	^{235}U	^{232}Th	^{147}Sm
apatite	18.81	21.80	22.25	5.93
zircon	15.55	18.05	18.43	4.76
sphene	17.46	20.25	20.68	5.47

Table 19.1: α -stopping distances (S) in μm .

Most minerals are not spherical but elongated prismatic, and can be approximated to a first degree as cylinders with radius r and height h :

$$F_T = 1 - \frac{1}{2} \frac{(r+h)S}{rh} + 0.2122 \frac{S^2}{rh} + 0.0153 \frac{S^3}{r^3} \quad (19.3)$$

An extensive list of formulas for even more realistic geometric shapes is provided by Ketcham, Gautheron, and Tassan-Got (2011). The α -ejection correction can be applied in one of three ways:

1. For relatively young (< 100 Ma) samples, the ejected helium can be mathematically replaced to a good approximation by dividing the uncorrected U-Th-He age by F_T Farley (2002):

$$t^* \approx \frac{t}{\frac{a(t^*)[U]}{a(t^*)[U]+b(t^*)[Th]} \left(\frac{137.818}{138.818} F_T^{238} + \frac{1}{138.818} F_T^{235} \right) + \frac{b(t^*)[Th]}{a(t^*)[U]+b(t^*)[Th]} F_T^{232}} \quad (19.4)$$

where t^* is the corrected age; $a(t^*)$ and $b(t^*)$ are defined in Equation 19.1; and F_T^{238} , F_T^{235} and F_T^{232} are the α -retention factors of ^{238}U , ^{235}U and ^{232}Th , respectively.

2. More accurate results are obtained by dividing not the age but the helium concentrations by the α -retention factor (Min et al., 2003; Vermeesch, 2008):

$$[\text{He}^*] = \frac{[\text{He}]}{\frac{a(t^*)[U]}{a(t^*)[U]+b(t^*)[Th]} \left(\frac{137.818}{138.818} F_T^{238} + \frac{1}{138.818} F_T^{235} \right) + \frac{b(t^*)[Th]}{a(t^*)[U]+b(t^*)[Th]} F_T^{232}} \quad (19.5)$$

and then plugging $[\text{He}^*]$ into Equation 19.1 instead of $[\text{He}]$. The difference between Equations 19.4 and 19.5 can reach several percent for early Precambrian ages.

3. The most accurate approach to α -ejection correction is to adjust not the radiogenic daughter product but the radioactive parents:

$$[^{238}\text{U}^*] = \frac{[^{238}\text{U}]}{F_T^{238}}, \quad [^{235}\text{U}^*] = \frac{[^{235}\text{U}]}{F_T^{235}}, \quad \text{and} \quad [^{232}\text{Th}^*] = \frac{[^{232}\text{Th}]}{F_T^{232}} \quad (19.6)$$

and then substituting $[^{238}\text{U}^*]$, $[^{235}\text{U}^*]$ and $[^{232}\text{Th}^*]$ for $[^{238}\text{U}]$, $[^{235}\text{U}]$ and $[^{232}\text{Th}]$ in Equation 19.1.

IsoplotR assumes that the α -ejection correction has been applied to the data **prior** to age calculation. This must be done using either method 2 or 3 above.

19.2 isochrons

More often than not, and more often than for other geochronometers, U–Th–(Sm)–He data are overdispersed with respect to the analytical uncertainties. Several mechanisms have been invoked to explain this overdispersion, including compositional effects, radiation damage, and breakage during mineral separation.

IsoplotR implements four different ways to visualise, average and quantify the overdispersion. The first two of these are the weighted mean and radial plot, which were discussed in Sections 14.1 and 14.3. The third way is the isochron plot and age. This uses a first order approximation of the U–Th–He age equation:

$$t \approx \frac{[{}^4\text{He}]}{P}, \text{ where } P = \left[8 \frac{137.818}{138.818} \lambda_{38} + 7 \frac{1}{138.818} \lambda_{35} \right] [\text{U}] + 6 \lambda_{32} [\text{Th}] \quad (19.7)$$

which is accurate to better than 1% for ages less than 100 Ma (Vermeesch, 2008). A U–Th–He isochron is constructed by plotting the numerator of the right-hand side of Equation 19.7 against the denominator and fitting a straight line through several aliquots of the same sample:

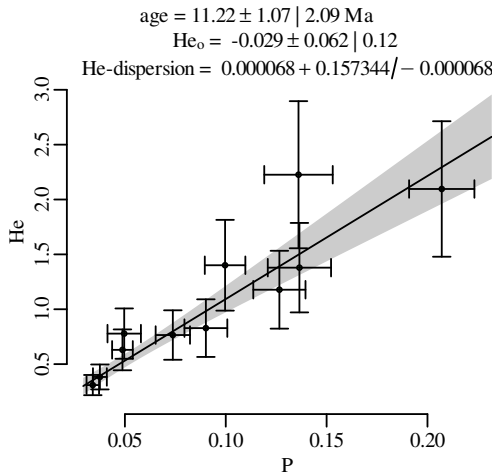


Figure 19.1: U–Th–He isochron with a model-3 fit. Because the parent and daughter nuclides are analysed separately on different mass spectrometers, their uncertainties are uncorrelated with each other. Hence the data are shown as error crosses instead of error ellipses.

19.3 Compositional data analysis and the ‘helioplot’

The fourth and final way to visualise and average U–Th–He data is based on the fact that U, Th and He are *compositional* data. This means that it is not so much the absolute concentrations of these elements that bear the chronological information, but rather their relative proportions. Equation 19.1 can be recast in terms of the elemental ratios U/He, Th/He, which take on strictly positive values:

$$a(t) \frac{[\text{U}]}{[\text{He}]} + b(t) \frac{[\text{Th}]}{[\text{He}]} = 1 \quad (19.8)$$

The space of all possible U–Th–He compositions fits within the constraints of a ternary diagram. If Sm is included as well, then this expands to a three-dimensional tetrahedral space (Vermeesch, 2008). The **central age** is obtained by first computing the average U–Th–He composition of a multi-sample dataset, and then calculating the U–Th–He corresponding to that composition. This is a similar procedure in a sense to the two-step process that was used to compute concordia ages in Section 15.2. Unfortunately, averaging compositional data is not as

straightforward as one may think. Consider, for example, the following ternary dataset:

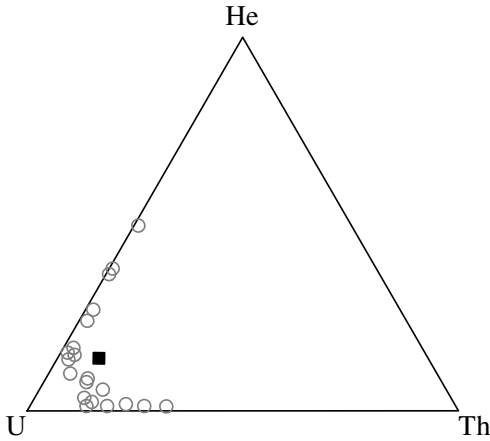


Figure 19.2: The U–Th–He age equation is scale invariant in the sense that the three elements can be renormalised to unity without loss of chronological information. This figure shows a synthetic dataset of 20 scattered U–Th–He measurements (grey circles). The arithmetic mean composition of the dataset is shown as a black square. It plots outside the data cloud, and is therefore not representative of the data.

Aitchison (1986) showed that the natural way to process compositional data is by subjecting them to a **logratio transformation**. In the case of the U–Th–He system, the logratio analysis is achieved by first defining two new variables:

$$u \equiv \ln\left(\frac{[U]}{[He]}\right), v \equiv \ln\left(\frac{[Th]}{[He]}\right) \quad (19.9)$$

and then performing the desired statistical analysis (averaging, uncertainty propagation, ...) on the transformed data. Upon completion of the mathematical operations, the results can then be mapped back to U–Th–(Sm)–He space using an inverse logratio transformation:

$$[He] = \frac{1}{[e^u + e^v + 1]}, [U] = \frac{e^u}{[e^u + e^v + 1]}, [Th] = \frac{e^v}{[e^u + e^v + 1]} \quad (19.10)$$

where $[He] + [U] + [Th] = 1$.

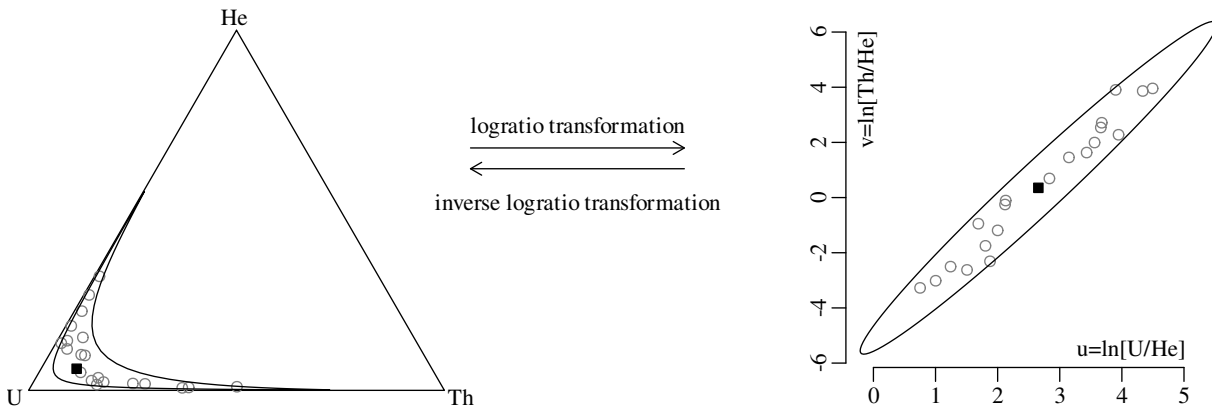


Figure 19.3: The logratio transformation maps data from an n -dimensional compositional space to an $(n - 1)$ -dimensional Euclidean space. For the U–Th–He data, it maps the data from a ternary diagram ($n = 3$) to a bivariate ($n - 1 = 2$) dataspace using Equation 19.9. In this transformed space, it is safe to calculate the arithmetic mean (black square) and confidence regions (black ellipse). After completion of these calculations, the result can be mapped back to the ternary diagram using the inverse logratio transformation (Equation 19.10).

In the context of U–Th–He dating, the central age is defined as the age that corresponds to the arithmetic mean composition in logratio space. `IsoplotR`'s `helioplot` function performs

this calculation using the same algorithm that is used to obtain the weighted mean U-Pb composition for the concordia age calculation (Section 15.2).

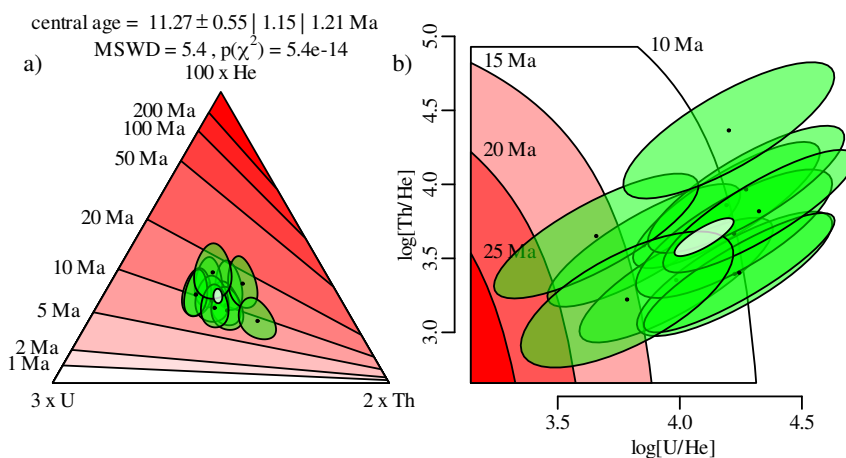


Figure 19.4: a) ternary diagram and b) logratio diagram or ‘helioplot’ of the U–Th–He data from Figure 19.1. The white ellipse marks the (geometric) mean U–Th–He composition.

Overdispersion is treated similarly as in a regression context (Section 13.6). Thus, there are options to augment the uncertainties with a factor $\sqrt{\text{MSWD}}$ (model-1); to ignore the analytical uncertainties altogether (model-2); or to add a constant overdispersion term to the analytical uncertainties (model-3). The helioplot diagram provides a convenient way to simultaneously display the isotopic composition of samples and their chronological meaning. In this respect, they fulfil the same purpose as the U–Pb concordia diagram (Section 15.2) and the U-series evolution plot (Section ??).

References

- Aitchison, J. (1986). *The statistical analysis of compositional data*. London, Chapman and Hall, p. 416.
- Farley, K. A. (2002). “(U–Th)/He dating: techniques, calibrations, and applications”. In: *Reviews in Mineralogy and Geochemistry* 47.1, pp. 819–844.
- Galbraith, R. F. (1990). “The radial plot: graphical assessment of spread in ages”. In: *Nuclear Tracks and Radiation Measurements* 17, pp. 207–214.
- Galbraith, R. F. and P. F. Green (1990). “Estimating the component ages in a finite mixture”. In: *Nuclear Tracks and Radiation Measurements* 17, pp. 197–206.
- Galbraith, R. F. and G. M. Laslett (1993). “Statistical models for mixed fission track ages”. In: *Nuclear tracks and radiation measurements* 21.4, pp. 459–470.
- Ketcham, R. A., C. Gautheron, and L. Tassan-Got (2011). “Accounting for long alpha-particle stopping distances in (U–Th–Sm)/He geochronology: refinement of the baseline case”. In: *Geochimica et Cosmochimica Acta* 75.24, pp. 7779–7791.
- Ludwig, K. R. (2003). “User’s manual for Isoplot 3.00: a geochronological toolkit for Microsoft Excel”. In: *Berkeley Geochronology Center Special Publication* 4 4.
- Min, K. et al. (2003). “Single grain (U–Th)/He ages from phosphates in Acapulco meteorite and implications for thermal history”. In: *Earth and Planetary Science Letters* 209.3–4, pp. 323–336.
- Vermeesch, P. (2008). “Three new ways to calculate average (U–Th)/He ages”. In: *Chemical Geology* 249, pp. 339–347.
- (2010). “HelioPlot, and the treatment of overdispersed (U–Th–Sm)/He data”. In: *Chemical Geology* 271.3–4, pp. 108–111. DOI: DOI:10.1016/j.chemgeo.2010.01.002.

Vermeesch, P. (2017). “Statistics for LA-ICP-MS based fission track dating”. In: *Chemical Geology* 456, pp. 19–27. DOI: <https://doi.org/10.1016/j.chemgeo.2017.03.002>.

Chapter 20

Fission tracks

IsoplotR accepts three types of fission track data:

1. ‘EDM’: ζ , $\text{err}[\zeta]$, ρ_D , $\text{err}[\rho_D]$, N_s , N_i
2. ‘ICP (ζ)’: ζ , $\text{err}[\zeta]$, spot size (μm), U_1 , $\text{err}[U_1]$, U_2 , $\text{err}[U_2]$, \dots , U_n , $\text{err}[U_n]$
3. ‘ICP (absolute)’: spot size (μm), U_1 , $\text{err}[U_1]$, U_2 , $\text{err}[U_2]$, \dots , U_n , $\text{err}[U_n]$

ζ , $\text{err}[\zeta]$, ρ_D , $\text{err}[\rho_D]$, and spot size are scalars, and N_s , N_i and U_i and $\text{err}[U_i]$ are vectors. The three formats represent two different approaches to fission track dating:

1. The External Detector Method (EDM) implements the neutron irradiation method that was previously introduced in Section 7.2.
2. The ‘ICP’ method uses LA-ICP-MS (see Section 3.1) to determine the ^{238}U -content of fission track samples. The main reasons for this change are the increased throughput achieved by not having to irradiate samples and the ease of double-dating apatite and zircon with the U-Pb method.

20.1 The external detector method

Recall the fission track age equation from Section 7.2:

$$t = \frac{1}{\lambda_{38}} \ln \left(1 + \frac{g_i}{g_s} \lambda_{38} \zeta \rho_d \frac{N_s}{N_i} \right) \quad (20.1)$$

The fission track method has been a test bed of statistical approaches that have subsequently been adopted by other chronometers. A case in point is the radial plot, which is uniquely suited to deal with the large and highly variable (‘heteroscedastic’) counting uncertainties of fission track data. Spontaneous fission is accurately described by a Poisson distribution. For young and/or uranium-poor samples, there is a finite probability that the spontaneous track count is zero for some grains. To accommodate such zero values, it is customary to use an arcsine transformation for radial plots instead of the usual logarithmic transformation (Galbraith, 1990):

$$z_j = \arcsin \sqrt{\frac{N_{sj} + 3/8}{N_{sj} + N_{ij} + 3/4}} \quad (20.2)$$

and

$$\sigma_j = \frac{1}{2\sqrt{N_{sj} + N_{ij} + 1/2}} \quad (20.3)$$

The arithmetic mean is not a reliable estimator of the true age, for a similar reason why the arithmetic mean is not the best estimator of the average U–Th–He composition and age. The Poisson distribution is negatively skewed, and this biases the arithmetic mean. The solution is similar as for the U–Th–He method, namely:

1. Take the average logarithm of the spontaneous and induced track densities.
2. Compute the fission track age the corresponds to this average ratio.

This procedure again gives rise to a ‘central age’. Fission track data are often overdispersed with respect to the Poisson counting uncertainties, and this dispersion carries important thermal history information. It is therefore customary to compute the average track density ratio using a model-3 style random effects model, in which the true ρ_s/ρ_i -ratio is assumed to follow a log-normal distribution with location parameter μ and scale parameter σ (Galbraith and Laslett, 1993):

$$\ln \left[\frac{\rho_s}{\rho_i} \right] \sim \mathcal{N}(\mu, \sigma^2) \quad (20.4)$$

This model gives rise to a two-parameter log-likelihood function:

$$\mathcal{L}(\mu, \sigma^2) = \sum_{j=1}^n \ln f_j(\mu, \sigma^2) \quad (20.5)$$

where the probability mass function $f_j(\mu, \sigma^2)$ is defined as:

$$f_j(\mu, \sigma^2) = \binom{N_{sj} + N_{ij}}{N_{sj}} \int_{-\infty}^{\infty} \frac{e^{\beta N_{sj}} (1 + e^{\beta})^{-N_{sj} - N_{ij}}}{\sigma \sqrt{2\pi} e^{(\beta - \mu)^2 / (2\sigma^2)}} d\beta \quad (20.6)$$

in which the fission track count ratios are subject to two sources of variation: the Poisson counting uncertainty and an ‘(over)dispersion’ factor σ . Maximising Eq. 20.5 results in two estimates $\hat{\mu}$ and $\hat{\sigma}$ and their respective standard errors. Substituting $\exp[\hat{\mu}]$ for N_s/N_i in Equation 20.1 produces the desired central age. $\hat{\sigma}$ estimates the overdispersion, and quantifies the excess scatter of the single grain ages which cannot be explained by the Poisson counting statistics alone. This dispersion can be just as informative as the central age itself, as it encodes geologically meaningful information about the compositional heterogeneity and cooling history of the sample.

20.2 LA-ICP-MS based fission track dating

The EDM continues to be the most widely used analytical protocol in fission track dating. However, over the past decade, an increasing number of laboratories have abandoned it and switched to LA-ICP-MS as a means of determining the uranium concentration of datable minerals, thus reducing sample turnover time and removing the need to handle radioactive materials (Hasebe et al., 2004; Chew and Donelick, 2012; Vermeesch, 2017). The statistical analysis of ICP-MS based FT data is less straightforward and less well developed than that of the EDM. The latter is based on simple ratios of Poisson variables, and forms the basis of a large edifice of statistical methods which cannot be directly applied to ICP-MS based data. The following paragraphs summarise Vermeesch (2017)’s solution to these issues, as implemented in *IsoplotR*.

Two analytical approaches are being used in ICP-based fission track geochronology, which each correspond to a different data format:

1. The ‘absolute dating’ method is based on Equation 7.8:

$$t = \frac{1}{\lambda_D} \ln \left(1 + \frac{\lambda_D}{\lambda_f} \frac{N_s}{[U] A_s R_e q} \right) \quad (20.7)$$

where N_s is the number of spontaneous tracks counted over an area A_s , q is an ‘efficiency factor’ (~ 0.93 for apatite and ~ 1 for zircon, Iwano and Danhara, 1998; Enkelmann and Jonckheere, 2003; Jonckheere, 2003; Soares et al., 2013) and $[U]$ is the ^{238}U -concentration (in atoms per unit volume) measured by LA-ICP-MS. Equation 20.7 requires an explicit value for λ_f and assumes that the etchable range (R_e) is accurately known (Soares et al., 2014).

2. The ζ -calibration method folds the etch efficiency, decay constant and etchable range into a ζ -calibration factor akin to that used in the EDM:

$$t = \frac{1}{\lambda_D} \ln \left(1 + \frac{1}{2} \lambda_D \zeta_{ICP} \frac{N_s}{A_s [U]} \right) \quad (20.8)$$

in which ζ_{ICP} is determined by analysing a standard of known FT age (Hasebe et al., 2004). Note that, in contrast with the ‘absolute’ dating method, the ζ -calibration method allows $[U]$ to be expressed in any concentration units (e.g., ppm or wt% of total U) or could even be replaced with the measured U/Ca-, U/Si- or U/Zr-ratios produced by the ICP-MS instrument.

20.3 Compositional zoning

Uranium-bearing minerals such as apatite and zircon often exhibit compositional zoning, which must either be removed or quantified in order to ensure unbiased ages. Two approaches are being used to deal with this issue:

1. The effect of compositional zoning can be *removed* by covering the entire counting area with one large laser spot (Soares et al., 2014) or a raster (Hasebe et al., 2004). The uncertainty of $[U]$ is then simply given by the analytical uncertainty of the LA-ICP-MS instrument, which typically is an order of magnitude lower than the standard errors of induced track counts in the EDM.
2. Alternatively, the uranium-heterogeneity can be *quantified* by analysing multiple spots per analysed grain (Hasebe et al., 2009). This is why **IsoplotR** accommodates multiple uranium measurements per aliquot ($U_1, \text{err}[U_1], \dots, U_n, \text{err}[U_n]$)

It is commonly found that the variance of the different uranium-measurements within each grain far exceeds the formal analytical uncertainty of each spot measurement. **IsoplotR** assumes that this dispersion is constant across all aliquots and follows a log-normal distribution:

$$\ln[U_{jk}] \sim \mathcal{N}(\mu_j, \sigma^2 + s[U]_{jk}^2) \quad (20.9)$$

where U_{jk} is the k^{th} (out of n_j) uranium concentration measurement, $s[U]_{jk}$ is its standard error, and μ_j and σ^2 are the (unknown) mean and variance of a Normal distribution. Note that μ_j is allowed to vary from grain to grain but σ is not. μ_j and σ can be estimated using the method of maximum likelihood, and the corresponding geometric mean uranium concentrations ($\exp[\mu_j]$) directly plugged into Equation 20.7.

To plot ICP-MS based fission track data on a radial plot, we can replace Eqs. 20.2 and 20.3 with

$$z_j = \ln(t_j), \quad (20.10)$$

$$\text{and } s_j = \sqrt{\left(\frac{s[\zeta]}{\zeta}\right)^2 + \left(\frac{s[U]}{U}\right)^2 + \frac{1}{N_s}} \quad (20.11)$$

respectively (Galbraith, 2010). Alternatively, a square root transformation may be more appropriate for young and/or U-poor samples:

$$z_j = \sqrt{t_j}, \quad (20.12)$$

$$\text{and } s_j = s[t_j] / (2\sqrt{t_j}) \quad (20.13)$$

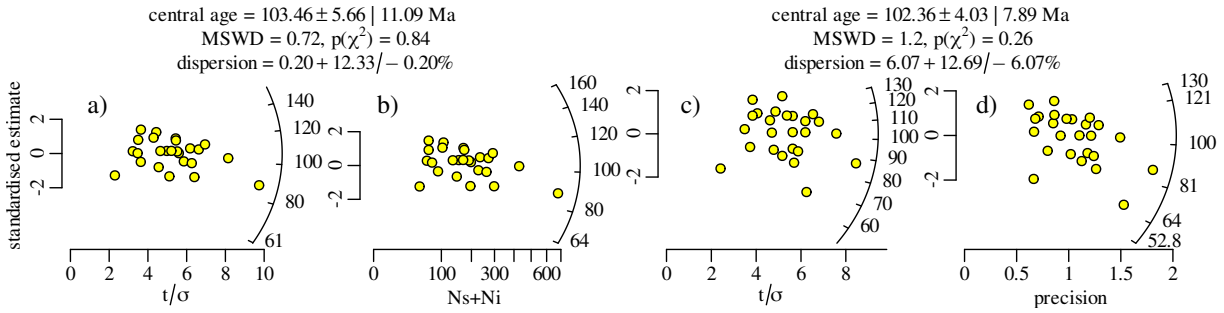


Figure 20.1: Radial plots of EDM-based fission track data using the a) logarithmic and b) arcsine transformation; and of ICP-based fission track data using the c) logarithmic and d) square root transformation.

20.4 Zero track counts

The standard error of a single grain fission track age estimate can be derived by standard error propagation. For the EDM, this yields:

$$s[t] \approx t \sqrt{\left(\frac{s[\zeta]}{\zeta}\right)^2 + \left(\frac{s[\rho_D]}{\rho_D}\right)^2 + \frac{1}{N_s} + \frac{1}{N_i}} \quad (20.14)$$

which returns an infinite uncertainty if either N_s or N_i is zero. For the EDM, this problem is adequately addressed by adding half a count to both the spontaneous and induced track count:

$$s[t] \approx t \sqrt{\left(\frac{s[\zeta]}{\zeta}\right)^2 + \left(\frac{s[\rho_D]}{\rho_D}\right)^2 + \frac{1}{N_s + \frac{1}{2}} + \frac{1}{N_i + \frac{1}{2}}} \quad (20.15)$$

This correction avoids the problem with zero or small counts whilst only having a minor effect on the accuracy of the estimate. Unfortunately this simple trick does not work for ICP-based fission track data, whose uncertainty estimates are given by (for the absolute dating approach):

$$s[t] \approx t \sqrt{\left(\frac{s[U]}{U}\right)^2 + \frac{1}{N_s}} \quad (20.16)$$

Adding half a count to the spontaneous fission track count would introduce more or less bias depending on whether the grain is poor or rich in uranium. One pragmatic solution to

this problem is to approximate the ICP-MS based uranium concentration measurement with an ‘equivalent induced track density’, using the following linear transformation:

$$\hat{N}_{ij} = \rho_j A_{sj} [U_j] \quad (20.17)$$

where A_{sj} is the area over which the spontaneous tracks of the j^{th} grain have been counted and ρ_j plays a similar role as ρ_d in Eq. 7.9. From the requirement that the variance of a Poisson-distributed variable equals its mean, it follows that:

$$\hat{N}_{ij} = \rho_j^2 A_{sj}^2 [U_j]^2 \quad (20.18)$$

from which it is easy to determine ρ_j . Thus the ICP-MS data have effectively been converted in to EDM data, and can be subjected to the same treatment as EDM data.

References

- Chew, D. M. and R. A. Donelick (2012). “Combined apatite fission track and U-Pb dating by LA-ICP-MS and its application in apatite provenance analysis”. In: *Quantitative Mineralogy and Microanalysis of Sediments and Sedimentary Rocks: Mineralogical Association of Canada, Short Course 42*, pp. 219–247.
- Enkelmann, E and R Jonckheere (2003). “Correction factors for systematic errors related to the track counts in fission-track dating with the external detector method”. In: *Radiation Measurements* 36.1, pp. 351–356.
- Galbraith, R. F. (1990). “The radial plot: graphical assessment of spread in ages”. In: *Nuclear Tracks and Radiation Measurements* 17, pp. 207–214.
- (2010). “Statistics for LA-ICPMS fission track dating”. In: *Thermo2010 - 12th International Conference on Thermochronology, Glasgow*, p. 175.
- Galbraith, R. F. and G. M. Laslett (1993). “Statistical models for mixed fission track ages”. In: *Nuclear tracks and radiation measurements* 21.4, pp. 459–470.
- Hasebe, N. et al. (2004). “Apatite fission-track chronometry using laser ablation ICP-MS”. In: *Chemical Geology* 207.3, pp. 135–145.
- Hasebe, N. et al. (2009). “The effect of chemical etching on LA-ICP-MS analysis in determining uranium concentration for fission-track chronometry”. In: *Geological Society, London, Special Publications* 324.1, pp. 37–46.
- Iwano, H and T Danhara (1998). “A re-investigation of the geometry factors for fission-track dating of apatite, sphene and zircon”. In: *Advances in Fission-Track Geochronology*. Springer, pp. 47–66.
- Jonckheere, R. (2003). “On the densities of etchable fission tracks in a mineral and co-irradiated external detector with reference to fission-track dating of minerals”. In: *Chemical Geology* 200.1, pp. 41–58.
- Soares, C. et al. (2014). “Novel calibration for LA-ICP-MS-based fission-track thermochronology”. In: *Physics and chemistry of minerals* 41.1, pp. 65–73.
- Soares, C. J. et al. (2013). “Further investigation of the initial fission-track length and geometry factor in apatite fission-track thermochronology”. In: *Am Mineral* 98, pp. 1381–1392.
- Vermeesch, P. (2017). “Statistics for LA-ICP-MS based fission track dating”. In: *Chemical Geology* 456, pp. 19–27. DOI: <https://doi.org/10.1016/j.chemgeo.2017.03.002>.

Chapter 21

²³⁰Th–U dating

The general principles of U-series disequilibrium dating were laid out in Chapter 8. Recall that the radioactive decay of ²³⁸U to ²⁰⁶Pb produces short-lived ²³⁰Th ($t_{1/2}=76$ kyr) and ²³⁴U ($t_{1/2}=246$ kyr), which may fractionate by one of several mechanisms:

1. U and Th have contrasting chemical properties and are easily fractionated during chemical processes such as crystallisation. This fractionation disrupts any pre-existing state of secular equilibrium between ²³⁰Th and its parent nuclide ²³⁴U.
2. Preferential leaching of weakly sited ²³⁴U due to energetic recoil of the U-nucleus during ²³⁸U-decay enriches ²³⁴U relative to ²³⁸U in river and sea water.
3. Redox processes and repeated precipitation–dissolution cycles may fractionate ²³⁴U from ²³⁸U, especially in the presence of organic acids in soils. This can produce ground waters that are highly enriched in ²³⁴U relative to ²³⁸U.

Section 8.1 showed that the fractionation between ²³⁴U and ²³⁸U can be used to date marine carbonates; Section 8.2 showed that the fractionation between ²³⁰Th and ²³⁴U can be used to date young volcanic rocks; and Section 8.3 combined the two equations together in a single equation. Recall Equation 8.10:

$$\frac{A(^{230}\text{Th})}{A(^{238}\text{U})} = 1 - e^{-\lambda_{230}t} + \frac{\lambda_{230}}{\lambda_{230} - \lambda_{234}}(\gamma_o - 1) \left(e^{-\lambda_{234}t} - e^{-\lambda_{230}t} \right) \quad (21.1)$$

where γ_o is the oceanic ²³⁴U/²³⁸U activity ratio. Equation 8.10 requires that γ_o is known and produces non-unique age solutions when $A(^{230}\text{Th})/A(^{238}\text{U}) > 1$. Both of these limitations can be avoided by recasting the equation in the following form:

$$\frac{A[^{230}\text{Th}] - A[^{230}\text{Th}]_o e^{-\lambda_{230}t}}{A[^{238}\text{U}]} = 1 - e^{-\lambda_{230}t} - \left(\frac{A[^{234}\text{U}]}{A[^{238}\text{U}]} - 1 \right) \left(\frac{\lambda_{230}}{\lambda_{234} - \lambda_{230}} \right) \left(1 - e^{[\lambda_{234} - \lambda_{230}]t} \right) \quad (21.2)$$

where $A[*]$ is the activity of $*$ and $A[^{230}\text{Th}]_o$ is the ‘detrital’ ²³⁰Th component, i.e. the ²³⁰Th that was already present in the sample at the time of its formation (Kaufman and Broecker, 1965; Ludwig, 2003). This component is unknown but can be estimated by isochron regression using long-lived ²³²Th as a normalising factor.

IsoplotR uses Equation 21.2 as the basis of all its U-series dating applications.

21.1 Data formats

IsoplotR accepts U-series data in four different formats:

1. $\frac{38}{32}, s[\frac{38}{32}], \frac{34}{32}, s[\frac{34}{32}], \frac{30}{32}, s[\frac{30}{32}], r[\frac{38}{32}, \frac{34}{32}], r[\frac{38}{32}, \frac{30}{32}], r[\frac{34}{32}, \frac{30}{32}]$
2. $\frac{32}{38}, s[\frac{32}{38}], \frac{34}{38}, s[\frac{34}{38}], \frac{30}{38}, s[\frac{30}{38}], r[\frac{32}{38}, \frac{34}{38}], r[\frac{32}{38}, \frac{30}{38}], r[\frac{34}{38}, \frac{30}{38}]$
3. $\frac{38}{32}, s[\frac{38}{32}], \frac{30}{32}, s[\frac{30}{32}], r[\frac{38}{32}, \frac{30}{32}]$
4. $\frac{32}{38}, s[\frac{32}{38}], \frac{30}{38}, s[\frac{30}{38}], r[\frac{32}{38}, \frac{30}{38}]$

where ‘30’, ‘32’, ‘34’ and ‘38’ stand for ^{230}Th , ^{232}Th , ^{234}U and ^{238}U , respectively. It is important to emphasise that, unlike all of **IsoplotR**’s other data formats, the numbers in these data tables are no atomic ratios but activity ratios. The relationship between activity ratios and atomic ratios is given by:

$$\frac{\text{activity}(x)}{\text{activity}(y)} = \frac{\text{atoms}(x) \lambda_x}{\text{atoms}(y) \lambda_y} \quad (21.3)$$

Formats 1 and 2 are applicable to carbonate lithologies in which both the $^{230}\text{Th}/^{234}\text{U}$ and $^{234}\text{U}/^{238}\text{U}$ equilibrium has been disturbed. Formats 3 and 4 are applicable to igneous rocks, in which only the $^{230}\text{Th}/^{234}\text{U}$ activity ratio has been disturbed, but ^{234}U and ^{238}U are in secular equilibrium (i.e. the ^{230}Th dating method of Section 8.2).

The error correlations of formats 1 and 3 tend to be stronger than those of formats 2 and 4. This is because formats 1 and 3 normalise the elements of the ^{238}U decay series to the highly variable amount of detrital ^{232}Th . In contrast, formats 2 and 4 feature only one ratio containing ^{232}Th , thus reducing a source of shared variability.

21.2 Isochrons

For igneous samples, in which $A[^{234}\text{U}]/A[^{238}\text{U}] = 1$, the second term on the right-hand side of Equation 21.2 vanishes and we can write:

$$\left(\frac{A[^{230}\text{Th}]}{A[^{232}\text{Th}]} \right)_i = \left(\frac{A[^{230}\text{Th}]}{A[^{232}\text{Th}]} \right)_o e^{-\lambda_{230}t} + \left(\frac{A[^{238}\text{U}]}{A[^{232}\text{Th}]} \right)_i (1 - e^{-\lambda_{230}t}) \quad (21.4)$$

for $1 \leq i \leq n$, which can be solved for t and $(A[^{230}\text{Th}]/A[^{232}\text{Th}])_o$ using the least squares method of York et al. (2004). Equation 21.4 (which was previously derived as Equation 8.5) forms a ‘Rosholt’-type isochron, which is akin to a ‘normal’ isochron in Rb-Sr or Ar-Ar geochronology (Rosholt, 1976). Using $A[^{238}\text{U}]$ as the normalising factor instead yields an ‘Osmond’-type isochron, which is akin to an ‘inverse’ isochron in Ar-Ar or Pb-Pb geochronology (Osmond, May, and Tanner, 1970; Ludwig, 2003):

$$\left(\frac{A[^{230}\text{Th}]}{A[^{238}\text{U}]} \right)_i = (1 - e^{-\lambda_{230}t}) + \left(\frac{A[^{232}\text{Th}]}{A[^{238}\text{U}]} \right)_i \left(\frac{A[^{230}\text{Th}]}{A[^{232}\text{Th}]} \right)_o e^{-\lambda_{230}t} \quad (21.5)$$

Note that for the Rosholt isochron, the age is a function of the slope, whereas for the Osmond isochron, it is a function of the y-intercept.

For carbonate samples, in which ^{234}U and ^{238}U generally are not in secular equilibrium, three activity ratios are needed to determine the detrital ^{230}Th (and initial ^{234}U) component.

This in turn requires three dimensional isochron regression of the $^{230}\text{Th}/^{238}\text{U}$ -, $^{232}\text{Th}/^{238}\text{U}$ - and $^{234}\text{U}/^{238}\text{U}$ -activity ratios. **IsoplotR** performs this calculation with the maximum likelihood algorithm of Ludwig and Titterton (1994). This solves the following system of equations:

$$\begin{cases} \left[\frac{^{234}\text{U}}{^{238}\text{U}} \right]_i = a + b \left[\frac{^{232}\text{Th}}{^{238}\text{U}} \right]_i + \delta_i \\ \left[\frac{^{230}\text{Th}}{^{238}\text{U}} \right]_i = A + B \left[\frac{^{232}\text{Th}}{^{238}\text{U}} \right]_i + \epsilon_i \end{cases} \quad (21.6)$$

where δ_i and ϵ_i are the bivariate normal residuals. Equation 21.6 can be solved by maximising the following log-likelihood function for x_i , a , b , A and B :

$$\mathcal{LL} = \text{const.} - \frac{1}{2} \sum_{i=1}^n \begin{bmatrix} \left[\frac{^{32}\text{Th}}{^{38}\text{U}} \right]_i - x_i \\ \left[\frac{^{34}\text{U}}{^{38}\text{U}} \right]_i - a - bx_i \\ \left[\frac{^{30}\text{Th}}{^{38}\text{U}} \right]_i - A - Bx_i \end{bmatrix}^T \begin{bmatrix} s \left[\frac{^{32}\text{Th}}{^{38}\text{U}} \right]_i^2 & s \left[\frac{^{32}\text{Th}}{^{38}\text{U}}, \frac{^{34}\text{U}}{^{38}\text{U}} \right]_i & s \left[\frac{^{32}\text{Th}}{^{38}\text{U}}, \frac{^{30}\text{Th}}{^{38}\text{U}} \right]_i \\ s \left[\frac{^{34}\text{U}}{^{38}\text{U}}, \frac{^{32}\text{Th}}{^{38}\text{U}} \right]_i & s \left[\frac{^{34}\text{U}}{^{38}\text{U}} \right]_i^2 & s \left[\frac{^{34}\text{U}}{^{38}\text{U}}, \frac{^{30}\text{Th}}{^{38}\text{U}} \right]_i \\ s \left[\frac{^{30}\text{Th}}{^{38}\text{U}}, \frac{^{32}\text{Th}}{^{38}\text{U}} \right]_i & s \left[\frac{^{30}\text{Th}}{^{38}\text{U}}, \frac{^{34}\text{U}}{^{38}\text{U}} \right]_i & s \left[\frac{^{30}\text{Th}}{^{38}\text{U}} \right]_i^2 \end{bmatrix}^{-1} \begin{bmatrix} \left[\frac{^{32}\text{Th}}{^{38}\text{U}} \right]_i - x_i \\ \left[\frac{^{34}\text{U}}{^{38}\text{U}} \right]_i - a - bx_i \\ \left[\frac{^{30}\text{Th}}{^{38}\text{U}} \right]_i - A - Bx_i \end{bmatrix} \quad (21.7)$$

which uses the shorthand notation introduced at the beginning of Section 21.1. The isochron age can be obtained by substituting the estimate of a for $\left[\frac{^{234}\text{U}}{^{238}\text{U}} \right]_i$ and A for $\left[\frac{^{230}\text{Th}}{^{238}\text{U}} \right]_i$ in Equation 21.2, and setting $A[^{230}\text{Th}]_0 = 0$. The results of the three-dimensional isochron regression can be visualised in four possible ways:

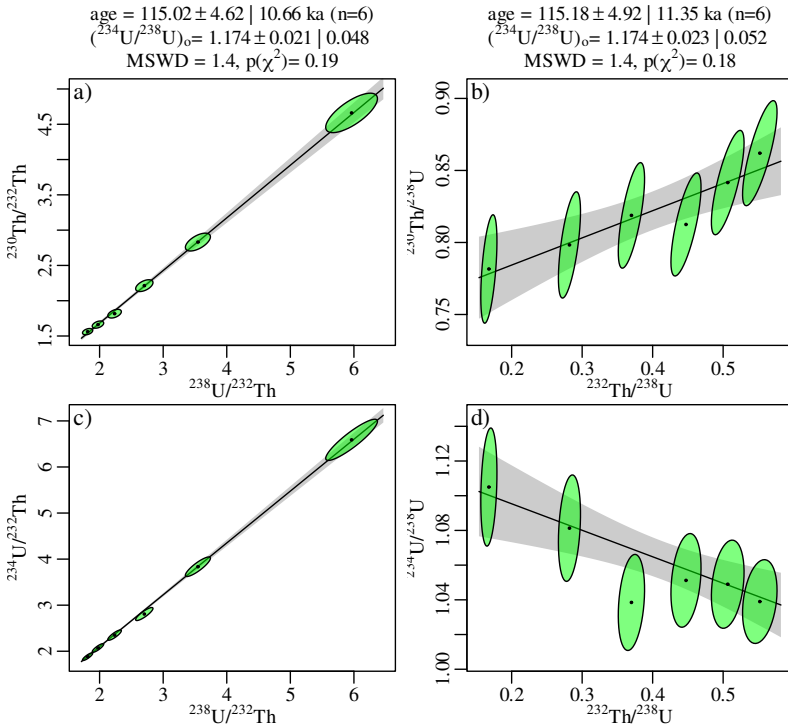


Figure 21.1: The same ^{230}Th - U data shown on a) Rosholt type-I, b) Osmond type-I, c) Rosholt type-II and d) Osmond type-II isochron diagrams. Note the slight difference in the isochron age. This is due to the skewness of the log-likelihood function, which does not allow negative values. This effect applies to all isochrons and is most prominent when the analytical uncertainties are relatively large compared to the activity ratios themselves. Solving this issue requires a reformulation of the isochron equation in terms of log-ratios, which has not yet been attempted.

21.3 Th-U evolution diagrams

In addition to (Rosholt and Osmond) isochrons and the usual weighted mean, radial, CAD and KDE plots, U-series data can also be visualised on Th-U evolution diagrams. For carbonate data, these consist of a scatter plot that sets out the $^{234}\text{U}/^{238}\text{U}$ -activity ratios against the $^{230}\text{Th}/^{238}\text{U}$ -activity ratios as error ellipses, and displays the authigenic $^{234}\text{U}/^{238}\text{U}$ -activity ratios and ages as a set of intersecting lines.

The Th-U evolution diagram has a similar purpose and appearance as the U-Pb concordia diagram, which also displays compositions and dates simultaneously. An alternative way of doing so for carbonate samples is by plotting the initial $^{234}\text{U}/^{238}\text{U}$ -ratios against the ^{230}Th - ^{234}U - ^{238}U -ages. In both types of evolution diagrams, *IsoplotR* provides the option to project the raw measurements along the best fitting isochron line and thereby remove the detrital ^{230}Th -component. This procedure allows a visual assessment of the degree of homogeneity within a dataset, as is quantified by the MSWD.

Neither the U-series evolution diagram nor the $^{234}\text{U}/^{238}\text{U}$ vs. age plot is applicable to igneous datasets, in which ^{234}U and ^{238}U are in secular equilibrium. For such datasets, *IsoplotR* produces an Osmond-style regression plot that is decorated with a fanning set of isochron lines.

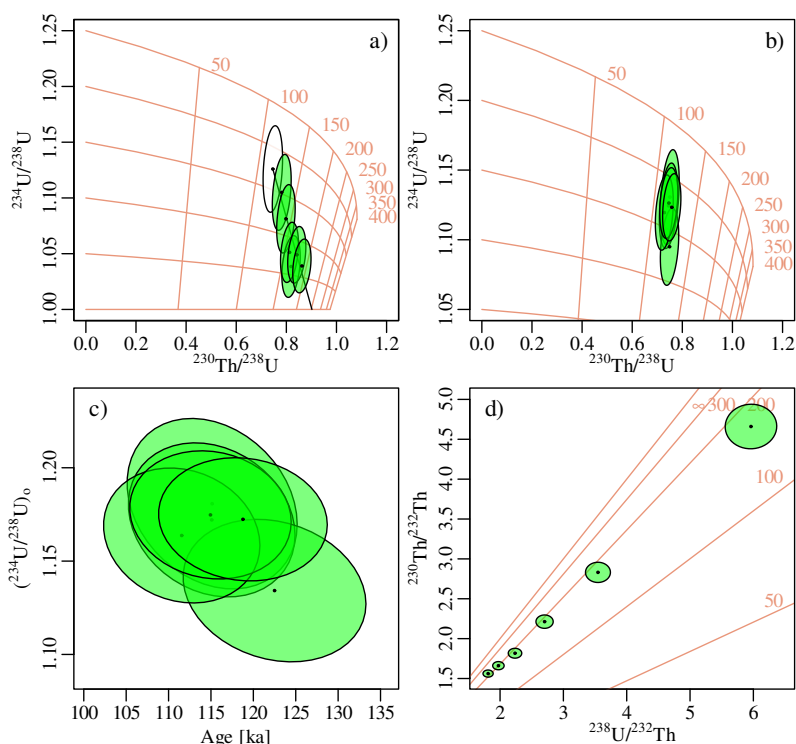


Figure 21.2: The data of Figure 21.1 shown on a ^{230}Th -U evolution diagram a) showing the raw data with an isochron fit and the inferred authigenic end member composition shown as a white ellipse; and b) showing the data projected along the isochron. c) shows the projected data in initial $^{234}\text{U}/^{238}\text{U}$ -activity vs. ^{230}Th -U age space. d) shows *IsoplotR*'s output for an evolution diagram of data formats 3 and 4. In this case the data are shown in Rosholt type-I space with isochrons shown in salmon red.

References

- Kaufman, A. and W. Broecker (1965). "Comparison of Th^{230} and C^{14} ages for carbonate materials from Lakes Lahontan and Bonneville". In: *Journal of geophysical Research* 70.16, pp. 4039–4054.
- Ludwig, K. R. (2003). "Mathematical-statistical treatment of data and errors for $^{230}\text{Th}/\text{U}$ geochronology". In: *Reviews in Mineralogy and Geochemistry* 52.1, pp. 631–656.
- Ludwig, K. R. and D. Titterton (1994). "Calculation of ^{230}Th -U isochrons, ages, and errors". In: *Geochimica et Cosmochimica Acta* 58.22, pp. 5031–5042.
- Osmond, J., J. P. May, and W. Tanner (1970). "Age of the Cape Kennedy Barrier-and-Lagoon Complex". In: *Journal of Geophysical Research* 75.2, pp. 469–479.
- Rosholt, J. (1976). " $^{230}\text{Th}/^{234}\text{U}$ dating of travertine and caliche rinds". In: *Geological Society of America Abstracts with Programs*. Vol. 8, p. 1076.
- York, D. et al. (2004). "Unified equations for the slope, intercept, and standard errors of the best straight line". In: *American Journal of Physics* 72.3, pp. 367–375.

Chapter 22

Detrital geochronology

22.1 Maximum depositional age estimation

Detrital geochronology is often the only way to estimate the depositional age of siliclastic rocks in the absence of fossils or volcanic ash layers. Detrital zircon U–Pb geochronology in particular has become a popular technique to obtain maximum depositional ages (MDAs). However other chronometers such as $^{40}\text{Ar}/^{39}\text{Ar}$ can be used for this purpose as well, and can in fact be more useful than U–Pb. Numerous MDA estimation algorithms have been proposed over the years, such as:

1. the youngest single grain (YSG);
2. the youngest grain cluster at 1σ (YGC1 σ) or 2σ (YGC2 σ);
3. the youngest detrital zircon estimated by Ludwig (2003)’s Monte Carlo resampling algorithm (YDZ);
4. the outcome of Ludwig and Mundil (2002)’s TuffZirc algorithm;
5. the weighted mean of the youngest three (Y3Z) or four (Y4Z) zircons;
6. the minimum age of grains selected by Gehrels (2003)’s AgePick algorithm.
7. the mode of the youngest graphical peak on a probability density plot (YPP);
8. the weighted mean of the grains in the youngest peak of a probability density plot (τ); and

The first six groups of methods gradually drift to younger ages with increasing sample size, for reasons that are essentially captured by Figure 14.6: increasing sample size increases the ‘power’ of statistical tests to subdivide a population of values in to smaller subpopulations. The youngest of these subpopulations inevitably gets younger as the number of subpopulations increases. In contrast, the last two methods converged to ages that are systematically too old. The failure of YPP and τ to retrieve the correct depositional age reflects the underlying flaws of the probability density plots (PDPs) on which they are based. The shortcomings of PDPs were explained in Section 14.2 and won’t be discussed further here.

The minimum age model of Equation 14.7 does not suffer from this undesirable sample size dependency. With increasing sample size, this model converges to a sensible value, provided that the following assumptions are met:

1. the true age distribution approximately follows the functional form shown in Figure 14.7; and

2. the analytical uncertainties are well characterised.

The first assumption is generally easy to verify. If the young end of the age spectrum is marked by a cluster of nearly concordant ages, then the minimum age model will appropriately average these. And it will do so even if the old end of the spectrum does not look like a (log)normal distribution. It is not uncommon for detrital zircon U–Pb age distributions to be fat tailed at both ends of the spectrum. However, similar results are obtained by the full model (Equation 14.7) and a 3-parameter simplification in which $\gamma = \mu$. This suggests that even quite strong violations of the parametric assumptions do not have a major effect on the outcomes.

If the age difference between the youngest and the second youngest grains in a sample is significantly greater than their respective analytical uncertainties, then the minimum age model will simply return the youngest age as a result. In other words, for fat tailed age spectra, the minimum age model reduces to the YSG model. This is the most sensible solution from a statistical point of view. In the absence of a discrete youngest age peak, the objections to the YSG model raised before do not apply. However whether age of the youngest grain is also the most sensible solution from a geological point of view is a different matter.

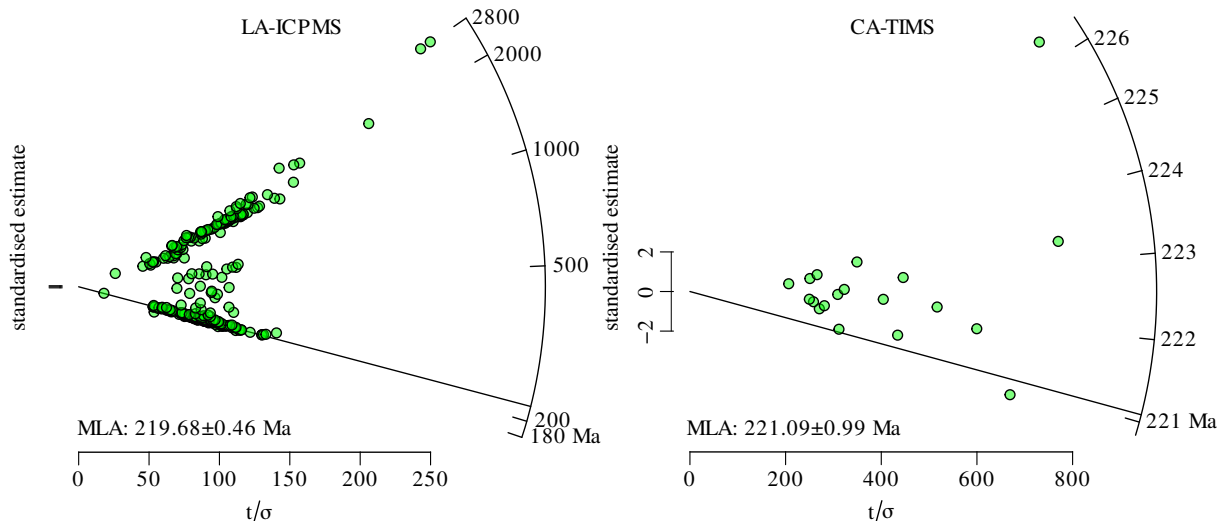


Figure 22.1: Radial plots and MDA estimates for sample 297 of Gehrels et al. (2020, LA-ICPMS data, left) and Rasmussen et al. (2020, CA-TIMS data, right), calculated with *IsoplotR* (Vermeesch, 2018). The MDA estimates agree to within 0.6% despite the great differences in sample size and analytical precision between the two datasets. The ad hoc MDA estimation algorithms listed at the start of this Section do not fare so well, resulting in differences of 2 – 17% between the LA-ICPMS and CA-TIMS data.

22.2 Multi-sample plots

The principal aim of the methods and graphical devices discussed thus far has been to extract geologically meaningful information from multiple aliquots of a single sample. However, most geochronological applications nowadays involve multiple samples, and the differences between these samples often has greater scientific significance than any individual date. *IsoplotR* implements a number of graphical devices to facilitate the interpretation of such multi-sample datasets. The CAD is the easiest way to simultaneously visualise multiple age distributions on a single plot.

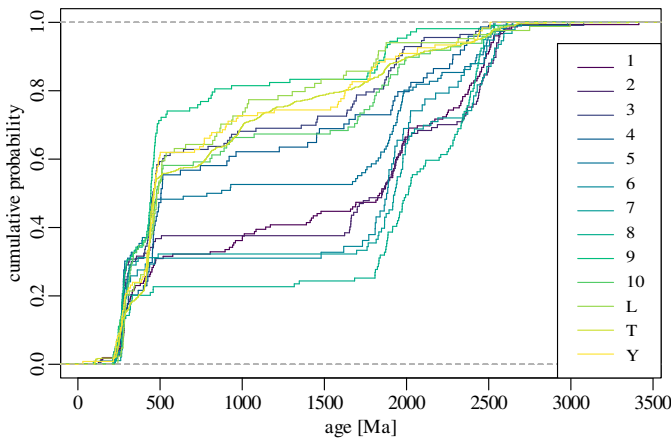


Figure 22.2: CAD plot of 13 detrital zircon U-Pb datasets from China (Vermeesch, 2013). Samples with similar age distributions have CADs that plot close together. Dissimilar samples are characterised by greater vertical separation of their respective CADs. The CAD is the only way to plot several complete datasets together on a single panel figure. However this plot becomes cluttered when used to display more than 10 or so samples.

In contrast, KDEs are better presented in a multi-panel format. To facilitate the intercomparison of multiple age distributions, `IsoplotR` offers the option to force all panels to use the same kernel bandwidth, to normalise the area under each KDE to a common value, and to plot them all on the same timescale.

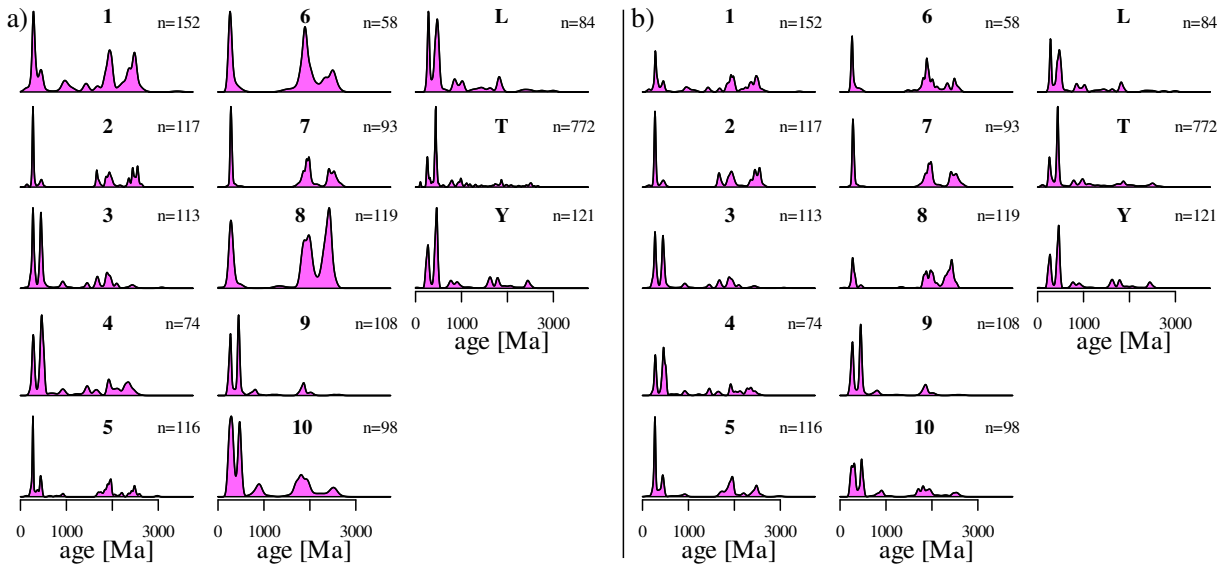


Figure 22.3: a) KDEs of the Chinese zircon data using different kernel bandwidths and scaled independently so as to display each sample to its maximum possible extent; b) KDEs of the same data using the same bandwidth (the median of all the plots in panel a) and normalised to the same area.

Visual comparison of CADs or KDEs can be an effective way to spot general trends and groupings in simple datasets. But this approach becomes impractical when the inter-sample differences are subtle or the datasets are large (> 10 samples, say). Such cases call for an additional layer of statistical simplification to emphasise the geologically significant differences whilst removing the less informative similarities. Multi-dimensional scaling (MDS) is one way to achieve this goal.

22.3 Multidimensional scaling

Multidimensional Scaling (MDS) is a multivariate **ordination** technique that is similar in many ways to PCA. MDS aims to extract two (or higher) dimensional ‘maps’ from tables of pairwise distances between objects. Let us illustrate the method with a simple geographical example. Consider the following table of pairwise distances between European cities:

	Athens	Barcelona	Brussels	...	Rome	Stockholm	Vienna
Athens	0	3313	2963	...	817	3927	1991
Barcelona	3313	0	1326	...	1460	2868	1802
Brussels	2963	1318	0	...	1511	1616	1175
⋮	⋮	⋮	⋮	⋮	⋮	⋮	⋮
Rome	817	1460	1511	...	0	2707	1209
Stockholm	3927	2868	1616	...	2707	0	2105
Vienna	1991	1802	1175	...	1209	2105	0

Figure 22.4: Table of road distances (in km) between European cities. The full dataset comprises 21 cities.

Given a table of this form, MDS reconstructs the map of Europe:

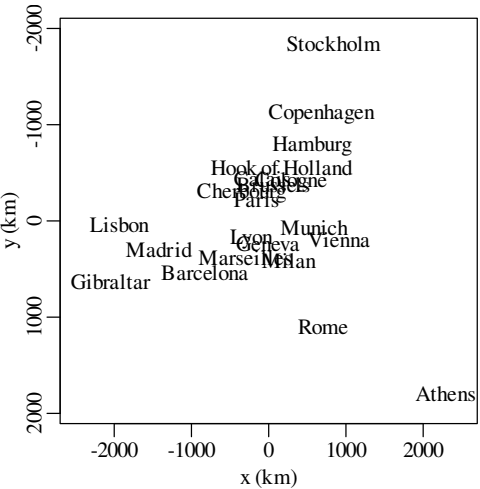


Table 22.1: MDS configuration of the European city distance data (Table 22.4). Cities (such as Lyon and Geneva) that are close together in the real world plot close together on the MDS configuration. And cities (such as Stockholm and Athens) that are far apart in the real world plot on opposite ends of the MDS configuration. But whilst the MDS configuration preserves the distances, it does not preserve the orientation of the cities. In this figure, the y-axis has been flipped, and the city locations are rotated $\sim 15^\circ$ in a clockwise sense compared to the real map of Europe.

We can measure the distances between the cities on the MDS map (in cm, inches or any other unit) and plot them against the input distances (in km) from Table 22.4. This produces a so-called **Shepard plot**:

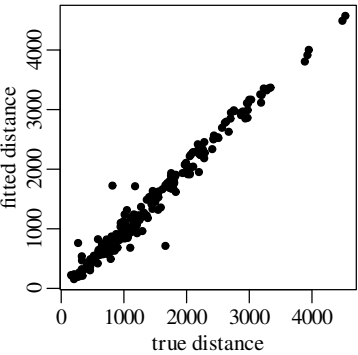


Figure 22.5: The Shepard plot of the European city distances shows a good agreement between the true input distances from Table 22.4 (x-axis) and the fitted distances measured on the MDS configuration of Figure 22.1 (y-axis). There are 21 cities in the dataset, resulting in $21 \times 20/2 = 210$ pairwise distances. Hence there are 210 data points on this scatter plot. Most of the scatter of the data around the best fit line is caused by the fact that the input data are *road distances*, which do not perfectly agree with the straight line map distances.

The scatter of the fitted data relative to the true distances can be quantified as the **Stress**:

$$S = \sqrt{\frac{\sum_{i=1}^n \sum_{j=i+1}^n (f(d[i, j]) - \delta[i, j])^2}{\sum_{i=1}^n \sum_{j=i+1}^n \delta[i, j]^2}} \quad (22.1)$$

where $d[i, j]$ is the input distance between objects i and j (for example the Euclidean distance of Table 22.1), $\delta[i, j]$ is the fitted distance measured on the MDS configuration, and f is a monotonic transformation that essentially maps $d[i, j]$ to the same scale as $\delta[i, j]$. The European city distance dataset is characterised by a Stress values of 7.5%, which corresponds to a ‘good’ fit:

fit	poor	fair	good	excellent	perfect
S	0.2	0.1	0.05	0.025	0

Table 22.2: Rule of thumb for interpreting the goodness of fit of an MDS configuration.

The preceding paragraphs have discussed the graphical output of MDS, but did not explain how this output is produced. It turns out that there are several ways to do so. In its simplest form (**classical MDS**), MDS consists of a simple sequence of matrix operations that are similar in many ways to the widely used principal component analysis algorithm. An alternative and more widely used approach (**nonmetric MDS**) uses an iterative gradient search algorithm to minimise Equation 22.1.

Nonmetric MDS is more flexible than classical MDS because it accommodates unconventional ‘dissimilarity’ measures that do not necessarily have to behave like conventional distances. So instead of physical distances expressed in kilometres or miles, we can also use MDS to interpret differences in chemical concentration, density, degree of correlation, and many other numerical quantities. In the context of detrital geochronology, the dissimilarity between samples is given by the statistical distance between age distributions. There are many ways to define this statistical distance. **IsoplotR** uses the Kolmogorov-Smirnov (KS) statistic due to its simplicity and the fact that it behaves like a true distance in the mathematical sense of the word (Vermeesch, 2013; Vermeesch, 2018).

The Kolmogorov-Smirnov statistic is defined as the maximum vertical distance between the CADs of the two samples:

$$D = \max_z |F_x(z) - F_y(z)| \quad (22.2)$$

where F_x and F_y are the CADs of x and y , respectively. D takes on values from 0 (two identical distributions) and 1 (no overlap between the two distributions). To illustrate the Kolmogorov-Smirnov method, consider two sand samples from China: one sample from the Yellow River, and one sample from a sand dune in the Mu Us desert:

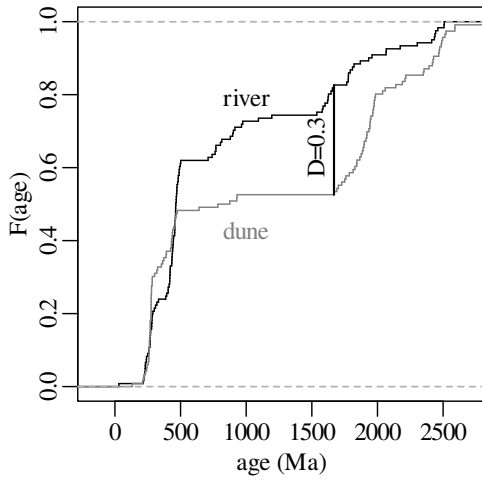


Figure 22.6: The two-sample Kolmogorov-Smirnov statistic is the maximum vertical distance between two CADs. This example compares the cumulative distributions of 121 detrital zircon U–Pb ages from the Yellow River with 116 detrital zircon U–Pb ages from a sand dune in the adjacent Mu Us desert. The KS-distance is 0.3006.

Calculating the KS-distance between samples two at a time populates a symmetric dissimilarity matrix with positive values and a zero diagonal. For the Chinese dataset, this produces the following 13×13 matrix:

$$d = \begin{matrix} & \begin{matrix} 1 & 2 & 3 & 4 & \boxed{5} & 6 & 7 & 8 & 9 & 10 & L & T & \boxed{Y} \end{matrix} \\ \begin{matrix} 1 \\ 2 \\ 3 \\ 4 \\ \boxed{5} \\ 6 \\ 7 \\ 8 \\ 9 \\ 10 \\ L \\ T \\ \boxed{Y} \end{matrix} & \begin{bmatrix} 0 & 14 & 33 & 27 & 18 & 14 & 15 & 22 & 48 & 32 & 42 & 37 & 40 \\ 14 & 0 & 36 & 33 & 16 & 14 & 15 & 24 & 46 & 32 & 47 & 42 & 43 \\ 33 & 36 & 0 & 19 & 24 & 44 & 47 & 55 & 17 & 10 & 13 & 12 & 8 \\ 27 & 33 & 19 & 0 & 20 & 38 & 41 & 48 & 28 & 14 & 21 & 17 & 16 \\ 18 & 16 & 24 & 20 & 0 & 22 & 24 & 33 & 31 & 20 & 33 & 28 & \boxed{30} \\ 14 & 14 & 44 & 38 & 22 & 0 & 14 & 24 & 52 & 41 & 52 & 48 & 49 \\ 15 & 15 & 47 & 41 & 24 & 14 & 0 & 16 & 51 & 43 & 54 & 49 & 52 \\ 22 & 24 & 55 & 48 & 33 & 24 & 16 & 0 & 61 & 53 & 63 & 59 & 62 \\ 48 & 46 & 17 & 28 & 31 & 52 & 51 & 61 & 0 & 20 & 22 & 18 & 16 \\ 32 & 32 & 10 & 14 & 20 & 41 & 43 & 53 & 20 & 0 & 17 & 15 & 13 \\ 42 & 47 & 13 & 21 & 33 & 52 & 54 & 63 & 22 & 17 & 0 & 10 & 11 \\ 37 & 42 & 12 & 17 & 28 & 48 & 49 & 59 & 18 & 15 & 10 & 0 & 7 \\ 40 & 43 & 8 & 16 & \boxed{30} & 49 & 52 & 62 & 16 & 13 & 11 & 7 & 0 \end{bmatrix} \end{matrix} \quad (22.3)$$

where the K-S values have been multiplied with 100 to remove the decimal points. Square boxes mark the two samples shown in Figure 22.6. Equation 22.3 is a symmetric matrix containing positive values and a zero diagonal. Thus it fulfils all the requirements for MDS analysis:

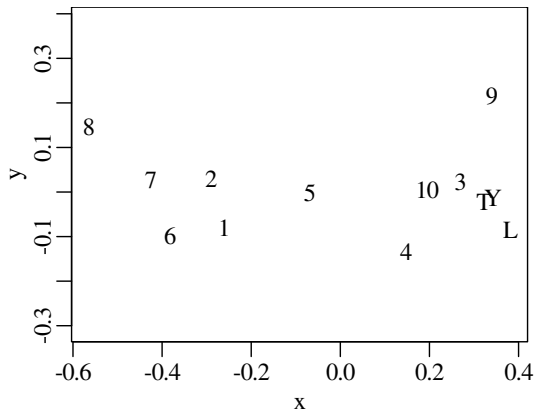


Figure 22.7: MDS configuration of the detrital zircon U–Pb data. Samples that have similar age distributions (such as ‘Y’ and ‘T’) are characterised by low K-S statistics (e.g., $d[Y, T] = 0.07$) and plot close together. Samples that have greatly differing age distributions (such as ‘Y’ and ‘8’) are characterised by high K-S statistics (e.g., $d[Y, 5] = 0.62$) and plot far apart on the MDS map.

References

- Gehrels, G. (2003). *AgePick*. <https://sites.google.com/a/laserchron.org/laserchron/home/> Last accessed: 2020-06-05.
- Gehrels, G. et al. (2020). “LA-ICPMS U–Pb geochronology of detrital zircon grains from the Coconino, Moenkopi, and Chinle Formations in the Petrified Forest National Park (Arizona)”. In: *Geochronology*.
- Kruskal, J. B. and M. Wish (1978). *Multidimensional scaling*. Vol. 07-011. Sage University Paper series on Quantitative Application in the Social Sciences. Sage Publications, Beverly Hills and London, p. 93.
- Ludwig, K. R. (2003). “User’s manual for Isoplot 3.00: a geochronological toolkit for Microsoft Excel”. In: *Berkeley Geochronology Center Special Publication 4* 4.
- Ludwig, K. and R. Mundil (2002). “Extracting reliable U–Pb ages and errors from complex populations of zircons from Phanerozoic tuffs”. In: *Geochimica et Cosmochimica Acta*. Vol. 66, A463–A463.
- Rasmussen, C. et al. (2020). “U–Pb zircon geochronology and depositional age models for the Upper Triassic Chinle Formation (Petrified Forest National Park, Arizona, USA): Implications for Late Triassic paleoecological and paleoenvironmental change”. In: *GSA Bulletin*.
- Torgerson, W. S. (1952). “Multidimensional scaling: I. Theory and method”. In: *Psychometrika* 17.4, pp. 401–419.
- Vermeesch, P. (2013). “Multi-sample comparison of detrital age distributions”. In: *Chemical Geology* 341, pp. 140–146.
- (2018). “Dissimilarity measures in detrital geochronology”. In: *Earth-Science Reviews* 178, pp. 310–321. DOI: 10.1016/j.earscirev.2017.11.027.
- Vermeesch, P. and E. Garzanti (2015). “Making geological sense of ‘Big Data’ in sedimentary provenance analysis”. In: *Chemical Geology* 409, pp. 20–27.
- Vermeesch, P., A. Resentini, and E. Garzanti (2016). “An R package for statistical provenance analysis”. In: *Sedimentary Geology*.
- Young, G. and A. S. Householder (1938). “Discussion of a set of points in terms of their mutual distances”. In: *Psychometrika* 3.1, pp. 19–22.

Part III

IsoplotR manual

Chapter 23

Introduction to IsoplotR

For many years, a Microsoft Excel add-in called *Isoplot* has been the main data processing software of choice in geochronology. Developed by Kenneth R. Ludwig over a period of two decades, *Isoplot* is a user-friendly toolbox that allows geologists to calculate and visualise geochronological data within a familiar spreadsheet environment (Ludwig, 1988; Ludwig, 1999; Ludwig, 2003; Ludwig, 2012). Few computer programs have been as widely used in the Earth Sciences as *Isoplot*. Written in Visual Basic for Applications (VBA), *Isoplot* takes isotopic data as input and produces publication-ready figures as output.

Unfortunately, recent versions of Excel are incompatible with *Isoplot*, whose creator has retired and no longer maintains the code. These software issues are a major problem for the field of radiometric geochronology, to the point where some laboratories kept an old Windows XP computer with Excel 2003 around for the sole purpose of running *Isoplot*.

IsoplotR is a free, open and more future proof alternative for *Isoplot* (Vermeesch, 2018). *IsoplotR*'s software architecture uses a modular design with future proofness and extendability in mind.

23.1 Software architecture

There are three ways to use *IsoplotR*: online, offline and from the command line.

The online version¹ is convenient in several ways. First, it requires no software installation. Second, the *IsoplotR* website is perfectly platform-independent. It renders on any modern HTML-5 compatible web browser, including those installed on smartphones and tablet computers. Third, by using the online version, the user is guaranteed to have accessed the most up-to-date version of the software.

An offline version of the GUI is provided for use on computers that are not (permanently) connected to the internet. This is often the case for machines that are connected to mass spectrometers, as a safety precaution. The offline version of the GUI works by emulating a web server within the default browser on the user's system. Installation instructions are provided on the *IsoplotR* website and on GitHub².

¹<http://isoplotr.london-geochron.com/>

²<https://github.com/pvermees/IsoplotRgui/>

The third way to access the full functionality of **IsoplotR** is through the command line within the R programming environment. The command line offers the greatest flexibility to automate, modify and extend **IsoplotR**'s functionality.

23.2 The Graphical User Interface (GUI)

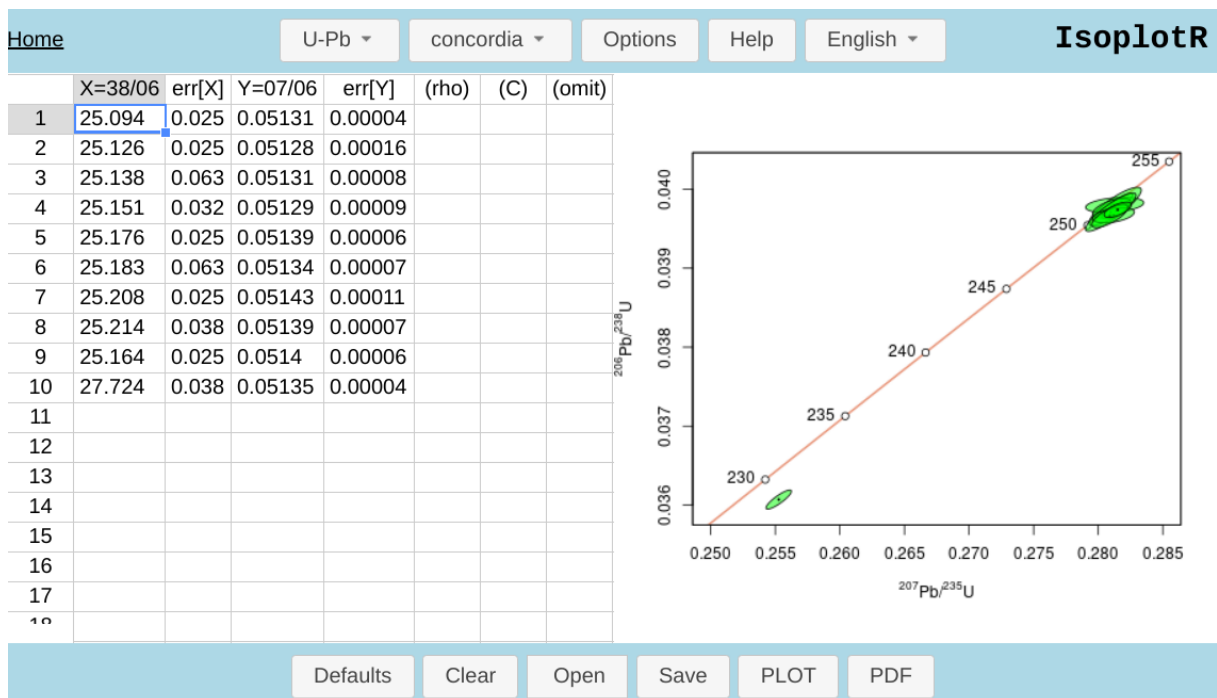
The code base for the GUI and the core data processing algorithms are surgically separated. The command-line functionality is grouped in a lightweight package called **IsoplotR** that may be installed from CRAN as instructed in Section 11.1.11. The **IsoplotR** package has minimal dependencies and should work on a basic R installation. In contrast, the GUI is written in **HTML** and **Javascript** and interacts with **IsoplotR** via an interface package. It is provided in a second R package called **IsoplotRgui** that is available from CRAN as well:

```
> install.packages('IsoplotRgui')
```

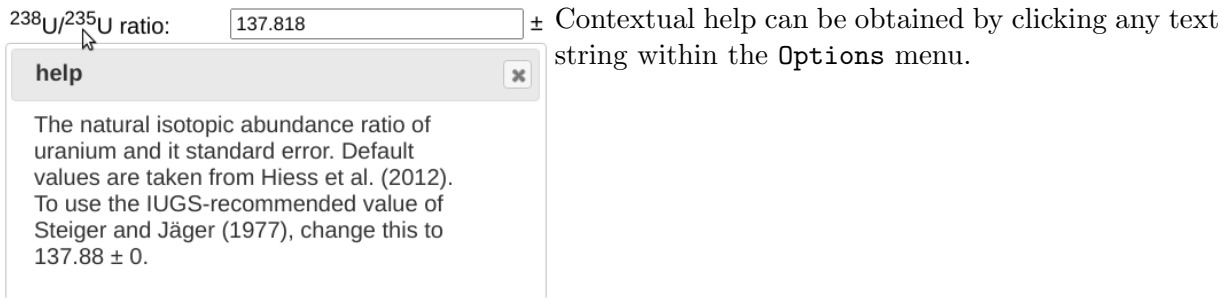
Once installed, **IsoplotRgui** can be started from the R console as follows:

```
> library(IsoplotRgui)
> IsoplotR()
```

This opens the GUI in a new tab of the user's default internet browser. The GUI has four components: a top bar with selection menus for the various chronometers and plot devices, optional settings and documentation; an input table into which data can be pasted from spreadsheet applications; an output window displaying the graphical or numerical results; and a lower bar to import and export data and results:



U-Pb ▾	IsoplotR currently implements 12 different geochronometers: U-Pb, Pb-Pb, Th-Pb, Ar-Ar, K-Ca, Rb-Sr, Sm-Nd, Re-Os, Lu-Hf, U-Th-He, fission tracks, and Th-U. Additionally, it also includes functionality for detrital geochronology and general purpose data processing.
concordia ▾	For each chronometer there are several possible plot devices. These may vary from method to method. For example, concordia plots are only available for U-Pb data, and release spectra for Ar-Ar data.
Options	The Options menu allows the user to choose between different input formats and change parameters (e.g. decay constants, plot colours) that affect the numerical or graphical output.
Help	The Help button provides further information about the input table, about the graphical and numerical numerical results, and some references. The Help function dynamically responds to the settings that are listed under the Options menu.
Open	The data and settings can be stored in a <code>.json</code> format for further processing in the future.
Save	
PLOT	The PLOT button (or RUN button if <code>ages</code> or <code>'get ζ'</code> is chosen as output) saves all the current settings and produces the graphical and/or numerical output.
RUN	
PDF	Clicking the PDF button repeats the calculations but saves the output as a <code>.pdf</code> file, which can be further processed by vector editing software such as Adobe Illustrator , CorelDraw or Inkscape . If <code>ages</code> is chosen as output saves the results to a comma separated value (<code>.csv</code>) file.
CSV	
(C)	The (C) column of the input table can be used to store numerical values that can be used as a fill colour for the plot symbols.
(omit)	Specific samples can be omitted from the numerical calculations (e.g. isochron, weighted mean, or concordia age) by marking them with a lowercase 'x' in the optional (omit) column. To hide samples from the graphical (as well as the numerical) output, mark them with an uppercase 'X'.
x	
X	
Input format: 1. Normal ▾	The Options menu provides access to a range of different input formats. Selecting any item from this menu replaces the input table with a different set of default data.
1. Normal	
2. Inverse	
3. Three ratios	
Input errors: 1se (abs) ▾	The Options menu also allows the user to specify the ratio uncertainties as being absolute or relative errors at 1 or 2 standard errors. Selecting any item from this menu automatically changes the input data accordingly.
1se (abs)	
2se (abs)	
1se (%)	
2se (%)	
Input errors: 1se (abs) ▾	Contextual help can be obtained by clicking any text string within the Options menu.
1se (abs)	
2se (abs)	
1se (%)	
2se (%)	



23.3 The Command Line Interface (CLI)

CLI offers all the functionality of the GUI, and more. A complete list of public functions can be viewed by typing

```
> help(package='IsoplotR')
```

at the command prompt. Data are read from comma-separated variable (.csv) files using the `read.data()` function. For example:

```
1 UPb_dat <- read.data('file.csv',method='U-Pb',format=1,ierr=3)
```

where

<code>'file.csv'</code>	is the name of the data file
<code>method='U-Pb'</code>	specifies the chronometer
<code>format=1</code>	tells <code>IsoplotR</code> that <code>file.csv</code> contains the following columns: $^{207}\text{Pb}/^{235}\text{U}$, $\text{err}[^{207}\text{Pb}/^{235}\text{U}]$, $^{206}\text{Pb}/^{238}\text{U}$, $\text{err}[^{206}\text{Pb}/^{238}\text{U}]$, and r , where <code>'err[*]'</code> marks the uncertainties of <code>'*'</code> , and r is the correlation coefficient between $\text{err}[^{207}\text{Pb}/^{235}\text{U}]$ and $\text{err}[^{206}\text{Pb}/^{238}\text{U}]$ (see Chapter 13).
<code>ierr=3</code>	indicates that these uncertainties (<code>'err[*]'</code>) are specified as relative values at two standard errors.

Further details about these arguments can be viewed by typing `?read.data` at the console. The various plot devices are implemented in a collection of designated functions such as `concordia()`, `isochron()`, `weightedmean()`, `isochron()`, `agespectrum()`, `KDE()`, `CAD()` and `radialplot()` that will be discussed in further details in later chapters. A table of age estimates can be obtained using the `ages()` function. Many of `IsoplotR`'s functions are *overloaded*, which means that the same function can be applied to multiple data types with potentially different results. For example, using the output of `read.data('data.csv',method='Rb-Sr')` as input to the `isochron()` function automatically produces a Rb–Sr isochron, with the correct decay constants and axis labels.

A colour scale can be added to most plots using the options `levels` argument. For example:

```
2 ns <- length(UPb_dat)
3 concordia(UPb_dat,levels=runif(ns),ellipse.fill=c("yellow","red"))
```

assigns a vector of random numbers to some U–Pb data and uses these numbers to colour the error ellipses on a concordia diagram from yellow to red. Omitting or hiding samples from

calculations and/or plots is achieved by specifying the indices of the relevant aliquots to the functions of interest. For example:

```
2 weightedmean(UPb_dat,omit=10)
```

omits the 10th from the weighted mean calculation, whereas

```
2 weightedmean(UPb_dat,hide=10)
```

removes the aliquot from the weighted mean diagram altogether.

The GUI may be the easiest way to interact with `IsoplotR` and explore various data processing strategies with individual samples. But the CLI is more useful than the GUI when processing large datasets comprising multiple samples, and provides a powerful mechanism to produce *reproducible* science. The `.csv` data files and `.R` data processing scripts can easily be archived and shared with others. They provide a parsimonious way to produce FAIR science (Wilkinson et al., 2016).

References

- Ludwig, K. R. (1988). “ISOPLOT for MS-DOS, a plotting and regression program for radiogenic isotope data for IBM-PC compatible computers, version 1.00”. In: *USGS Open-File Report OF-88-0557*.
- (1999). “Using Isoplot/EX, version 2, a geochronological toolkit for Microsoft Excel”. In: *Berkeley Geochronological Center Special Publication 1a*.
- (2003). “User’s manual for Isoplot 3.00: a geochronological toolkit for Microsoft Excel”. In: *Berkeley Geochronology Center Special Publication 4* 4.
- (2012). “User’s manual for Isoplot version 3.75–4.15: a geochronological toolkit for Microsoft Excel”. In: *Berkeley Geochronological Center Special Publication 5*.
- Vermeesch, P. (2018). “`IsoplotR`: a free and open toolbox for geochronology”. In: *Geoscience Frontiers* 9, pp. 1479–1493.
- Wilkinson, M. D. et al. (2016). “The FAIR Guiding Principles for scientific data management and stewardship”. In: *Scientific data* 3.1, pp. 1–9.